

**Investigation of a Polymer-Dispersed Liquid Crystal System**  
**by NMR Diffusometry and Relaxometry**

Von der Fakultät für Naturwissenschaften  
Department Chemie  
der Universität Paderborn

zur Erlangung des Grades eines  
Doktors der Naturwissenschaften  
Dr. rer. nat.  
genehmigte Dissertation

von  
**Mingxue Tang**  
aus der Provinz Yunnan (China)

Paderborn 2013

Die vorliegende Arbeit wurde in der Zeit von Juli 2009 bis Januar 2013 im Fachgebiet Physikalische Chemie am Department Chemie der Fakultät für Naturwissenschaften der Universität Paderborn unter Anleitung von Prof. Dr. Claudia Schmidt angefertigt.

Referentin: Prof. Dr. Claudia Schmidt  
Korreferent: PD Dr. Hans Egold

Eingereicht am: 18.01.2013  
Mündliche Prüfung am: 26.02.2013

## **Acknowledgements**

First of all, I would like to thank my supervisor Prof. Dr. Claudia Schmidt for offering me this invaluable opportunity to undertake my thesis on this interesting topic and providing excellent facilities, research environment and continuous supports. And thanks for your support and patience in completing my thesis!

I would like to thank Prof. Dr. Heinz-Siegfried Kitzerow for his supervision, illuminating discussions and facilitation of knowledge transfer for my PhD project.

Many thanks would be extended to:

PD Dr. Hans Egold for being a valuable source of ideas and suggestions in the topic of NMR spectroscopy and moreover for agreeing to write the Korreferat.

Prof. Dr. Klaus Huber for the nice collaborations and illuminating suggestions.

Prof. Dr. Daniel Topgaard for his help with the diffusion NMR measurements at Lund University.

Prof. Dr. Jürgen Senker for discussion of pulse sequences.

Dr. Andreas Redler, Dr. Frank Markus Bayer and Martin Schneider for happy collaborations.

My colleagues, Dr. Richard Szopko, Dr. Alexander Lorenz, Dr. Andreas Hoischen, Dr. Gönül Ar, Felix Grewe, Martin Urbanski, Dmitry Kushnikovskiy, Zhiyuan Zhang, Melanie Kube and Svenja Marl for kind help and a positive working atmosphere.

Rita Egert-Tiesbohlenkamp, Gisela Jünnemann and Susanne Keuker-Baumann for the technical support.

Isabella Koralewicz for the perfect all-around help.

Finally, I would like to thank my family for their continuous support!

## Abstract

Polymer-dispersed liquid crystals (PDLCs) are polymer composites containing a dispersion of liquid crystal droplets in polymer networks. PDLCs have attracted much attention due to their unique properties and potential usage. The properties of PDLCs depend on the degree of phase separation and the size of liquid crystal droplets. To investigate the structure will help us to better understand and optimize PDLCs.

The main aim of this PhD thesis was to investigate PDLCs by NMR techniques. Diffusion constants and spin-lattice relaxation times in the laboratory ( $T_1$ ) and rotating frame ( $T_{1\rho}$ ) were measured for PDLCs as well as precursor mixtures based on the trifunctional monomer trimethylolpropane triacrylate (TMPTA) and the commercial nematic mixture E7.

The variation of the main dipolar splitting of  $^1\text{H}$  spectra with increasing temperature was analyzed to obtain the nematic-to-isotropic phase transition temperature and the nematic order parameter of E7 and, for comparison, the nematic liquid crystal 5CB.

Diffusion constants in TMPTA/E7 mixtures, measured by pulsed-field gradient NMR, increase for both E7 and TMPTA as the mass fraction of E7 increases, due to the lower viscosity of E7. E7 in the PDLC diffuses more slowly than in the bulk because of the hindrance by the polymer matrix.

$T_1$  and  $T_{1\rho}$  relaxation times in the liquid or liquid-crystalline phases of TMPTA and bulk E7 are higher than in the PDLC and the pure polymer, due to the lower mobility in the polymer samples.  $T_{1\rho}$  in the PDLC is even shorter than in the pure polymer, indicating an anti-softening effect caused by E7 molecules. In bulk E7, the well-ordered rod-like molecules exhibit a unique H-C dipolar coupling, which leads to oscillations in the cross-polarization curve. However, in the PDLC, the anchoring effect at the boundary between the polymer and LC droplets disturbs the molecular order resulting in a smooth cross polarization curve.

# Table of Contents

<b>Chapter 1 Introduction</b> .....	<b>1</b>
<b>Chapter 2 Introduction to Solid State NMR</b> .....	<b>5</b>
<b>2.1 NMR in solution and in the solid state</b> .....	<b>5</b>
<b>2.2 Chemical shift anisotropy (CSA)</b> .....	<b>6</b>
<b>2.3 Magic angle spinning (MAS)</b> .....	<b>8</b>
<b>2.4 Cross polarization (CP)</b> .....	<b>9</b>
<b>2.5 Spin relaxation</b> .....	<b>11</b>
2.5.1 Spin-lattice relaxation .....	11
2.5.2 Inversion recovery .....	12
2.5.3 Spin echo.....	14
<b>2.6 Setting up CPMAS experiments</b> .....	<b>16</b>
2.6.1 Magic angle adjustment .....	16
2.6.2 Cross polarization .....	18
<b>Chapter 3 Sample Applications of Solid State NMR</b> .....	<b>20</b>
<b>3.1 <sup>13</sup>C spectroscopy of diosgenin derivatives</b> .....	<b>20</b>
3.1.1 Diosgenin monosuccinate (MSD).....	20
3.1.2 Diosgenin monomaleate (MMD).....	21
<b>3.2 Chemical modification of polymer colloids</b> .....	<b>22</b>
<b>3.3 Composition determination</b> .....	<b>24</b>
<b>3.4 Determination of phase transitions of liquid crystals</b> .....	<b>25</b>
<b>3.5 Conclusions</b> .....	<b>27</b>
<b>Chapter 4 The PDLC System (P)TMPTA/E7: NMR Spectra and Polarizing Microscopy</b> .....	<b>28</b>
<b>4.1 Materials</b> .....	<b>28</b>
<b>4.2 Preparation of PDLCs</b> .....	<b>29</b>
<b>4.3 Spectra of TMPTA, E7 and mixtures</b> .....	<b>30</b>
4.3.1 <sup>1</sup> H spectra.....	30
4.3.2 Determination of the nematic-to-isotropic phase transition from <sup>1</sup> H spectra.....	35
4.3.3 <sup>13</sup> C Spectra .....	37
<b>4.4 Spectra of the polymer PTMPTA and of PDLCs</b> .....	<b>39</b>
4.4.1 <sup>1</sup> H spectra.....	39
4.4.2 <sup>13</sup> C spectra.....	41
<b>4.5 Textures of TMPTA/E7 by polarizing optical microscopy</b> .....	<b>44</b>
4.5.1 Microscopy measurements .....	44
4.5.2 Textures and phase behavior of TMPTA/E7 .....	45

4.6 Conclusions.....	47
<b>Chapter 5 Self-Diffusion in the PDLC Systems PTMPTA/E7 and Their Precursor Mixture</b> .....	<b>49</b>
5.1 Diffusion .....	49
5.2 NMR diffusometry.....	51
5.2.1 The pulsed gradient spin echo (PGSE) .....	51
5.2.2 Stimulated echo.....	53
5.3 Experimental aspects.....	54
5.3.1 Sample preparation .....	54
5.3.2 NMR measurements .....	54
5.4 Results and discussion .....	56
5.4.1 Proton spectra .....	56
5.4.2 Diffusion in isotropic mixtures .....	58
5.4.3 Diffusion in PDLCs .....	61
5.5 Conclusions.....	64
<b>Chapter 6 Relaxation Study of PDLC Systems PTMPTA/E7 and Their Precursor Mixture</b> .....	<b>65</b>
6.1 Correlation function, spectral density and relaxation rates .....	65
6.2 Determination of spin-lattice relaxation in the rotating frame, $T_{1\rho}$ .....	68
6.3 Results and discussions .....	70
6.3.1 Proton spin-lattice relaxation, $T_{1,H}$ .....	70
6.3.2 Carbon spin-lattice relaxation in the rotating frame, $T_{1\rho,C}$ .....	75
6.3.3 Proton spin-lattice relaxation in the rotating frame, $T_{1\rho,H}$ .....	82
6.4 Conclusions.....	86
<b>Chapter 7 Summary</b> .....	<b>88</b>
<b>Appendix</b> .....	<b>91</b>
A1 Additional NMR spectra .....	91
A2 Photographs of PDLCs.....	93
A3 Haller plot.....	94
A4 Diffusion measurement: example of spectra .....	95
A5 Determination of diffusion coefficients for E7 and PDLC .....	96
A6 Experimental parameters of diffusion experiments .....	98
A6.1 Static diffusion .....	98
A6.2 MAS diffusion .....	100
A7 Diffusion pulse programs .....	102
A7.1 Ramped BPP-LED sequence used for static diffusion measurements .....	102
A7.2 Sine-shaped BPP-LED pulse sequence used for MAS diffusion measurements ..	105

<b>A8 Relaxation in the rotating frame .....</b>	<b>110</b>
<b><i>List of Symbols</i> .....</b>	<b>111</b>
<b><i>References</i> .....</b>	<b>113</b>
<b><i>Publications</i>.....</b>	<b>118</b>

## Chapter 1 Introduction

Besides the conventional three states of matter (solid, liquid and gas), liquid crystals (LCs) are considered as a fourth state of matter that has properties between those of a conventional liquid and those of a solid crystal. LCs can flow like a liquid consisting of oriented molecules. Therefore LCs present special properties and play an important role in daily life, and both in the academic and industrial field. Liquid crystals were first observed in 1888 by Reinitzer as a strange phase between the liquid melt and the crystalline phase when heating and cooling cholesteryl benzoate.<sup>[1]</sup> One year later, Lehmann (Karlsruhe, Germany) investigated this mesophase for the same sample by polarizing optical microscopy and he chose “liquid crystals” as the title of the first book about the fourth state of matter.<sup>[2]</sup> A detailed history of liquid crystals can be found in reference.<sup>[3]</sup> More physical and chemical properties of liquid crystals can be found in books<sup>[4-7]</sup> and their applications are described, for example, in references.<sup>[8, 9]</sup>

Polymer-dispersed liquid crystals (PDLCs), as shown on the right of figure 1.1, are polymer composites containing a dispersion of micrometer- or submicrometer-sized liquid crystal droplets in a concentration of less than 70 %.<sup>[10, 11]</sup> PDLCs have been attracting more and more attention due to their unique properties and potential usages in many fields since the first PDLC devices were demonstrated by James Fergason, who was granted a U.S patent in 1984.<sup>[12]</sup> But the first study on the liquid crystal virus droplets in plants by X-ray can be traced back to 1941.<sup>[13]</sup> Later, the defects in nematic droplets were investigated by Volovik and Williams.<sup>[14, 15]</sup> From then, more than 1000 papers and 1000 patents on PDLCs were published till 2006.<sup>[16]</sup> Higgins investigated the liquid crystal droplet dynamics by optical microscopy.<sup>[17]</sup> They pointed out that the LC reorientation dynamics is strongly dependent on droplet size and shape, as well as on polymer/LC interfacial interactions. The dynamics also varies spatially within individual droplets. In PDLCs, each LC droplet has its own orientation (cf. Fig. 1.1). Therefore the sample appears opaque in optical observations. When an electrical field is applied, the LC droplets align and the PDLC becomes transparent. With this



property, PDLCs have many applications, for example, as switchable windows,<sup>[18]</sup> flexible displays,<sup>[19]</sup> or storage material.<sup>[20]</sup> For more properties and applications the reader is referred to several books or book chapters.<sup>[9, 21-25]</sup> The preparation of PDLCs was described by Bouteiller.<sup>[26]</sup> Generally, the fabrication of PDLC materials depends on the phase separation between liquid crystal and polymer network. These phase separation methods mainly include thermally-induced phase separation (TIPS), solvent-induced phase separation (SIPS), or polymerization-induced phase separation (PIPS).<sup>[11, 27]</sup> Figure 1.1 shows the principle of PIPS, which is used in this PhD work.

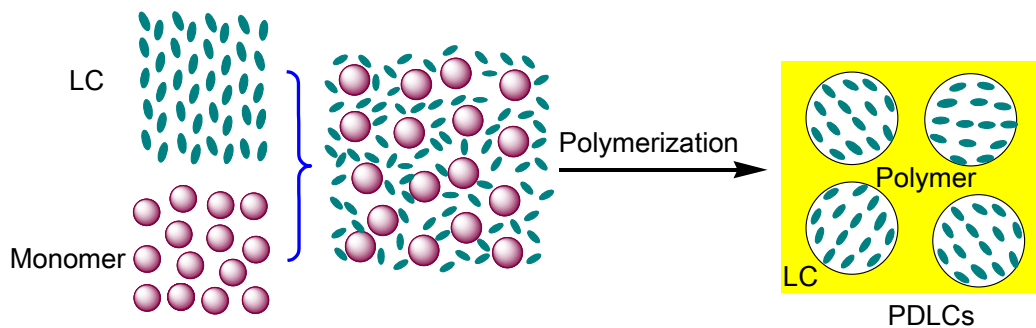


**Figure 1.1:** Schematic of PDLCs generated by PIPS.

Nuclear magnetic resonance (NMR) can be powerfully used to obtain a lot of useful information, such as compound assignments, internuclear distances, molecular orientations, molecular dynamics, and exchange processes. NMR spectra of deuterium ( $^2\text{H}$ ),<sup>[28-33]</sup> proton ( $^1\text{H}$ ),<sup>[34, 35]</sup> carbon ( $^{13}\text{C}$ ),<sup>[36-38]</sup> nitrogen ( $^{15}\text{N}$ ),<sup>[39]</sup> fluorine ( $^{19}\text{F}$ ),<sup>[34]</sup> phosphorus ( $^{31}\text{P}$ )<sup>[39]</sup> and xenon ( $^{129}\text{Xe}$ )<sup>[40]</sup> have been investigated to check the liquid crystal orientation, surface interaction and phase transitions.

A powerful tool in NMR investigations on LCs and PDLCs are relaxation measurements which provide information on molecular dynamics and orientational order<sup>[41, 42]</sup> or even anchoring effects on LC droplets in PDLCs. The main formalism of nuclear spin relaxation was developed in the classical works by Purcell and Pound,<sup>[43]</sup> Solomon,<sup>[44]</sup> Bloch,<sup>[45, 46]</sup> and Tomita.<sup>[47]</sup> NMR relaxation techniques range from measurements of the spin-lattice relaxation time  $T_1$  and spin-spin relaxation time  $T_2$  to the spin-lattice relaxation time in the rotating frame  $T_{1\rho}$ , and even further to cross

relaxation times. Cross and Fung applied magic-angle spinning (MAS) and polarization transfer to directly measure the cross relaxation rate between liquid crystal droplets and polymer.<sup>[48]</sup> To obtain a broad frequency range of  $T_1$  (~kHz to ~MHz), fast field-cycling NMR was developed and used.<sup>[49-53]</sup> Proton spin-lattice relaxation studies played a crucial role<sup>[54-57]</sup> in the late 1960s in identifying the unique collective dynamics known as order director fluctuations (ODF) in thermotropic LCs. Later, ODF involving two-dimensional or three-dimensional thermal excitations were found to be important in lipid bilayer dynamics.<sup>[58]</sup>

In particular, periodic PDLCs, namely holographic polymer-dispersed liquid crystals (HPDLCs),<sup>[59]</sup> whose properties depend on the spatial variation of the index of refraction, are of interest for optoelectronic or photonic applications. The index of refraction is determined by the degree of phase separation and the formation rate of HPDLCs. In cooperation with Dr. Redler on the diffusion-reaction model simulation which needs the initial diffusion coefficient of monomer in the precursor mixture of HPDLCs, pulsed field gradient NMR<sup>[60, 61]</sup> was chosen to measure the diffusion coefficients of each component in the mixture.

In the following chapters of this PhD thesis, Chapter 2 will focus on the basic theory and techniques used in solid state NMR (SSNMR), followed by a description of the set-up of SSNMR on our NMR spectrometer. Chapter 3 will give examples of SSNMR applications, such as the measurements of spectra of insoluble polymer colloids, which serve as a powerful and reliable tool to track the chemical modification. Moreover, it will be shown that NMR can be used to determine the phase transition and order parameter of liquid crystals, using 5CB as an example. Chapter 4 will describe the preparation of PDLC by polymerization-induced phase separation; secondly,  $^1\text{H}$  and  $^{13}\text{C}$  spectra of the PDLC system PTMPTA/E7 and its precursor will be given for component assignments. Furthermore, polarizing optical microscopy was chosen to study the phase behavior of the pure E7 and its mixtures with monomer TMPTA. The diffusometry study of the precursor and PDLC system will be described in detail in Chapter 5. Chapter 6 will concentrate on the relaxation investigation of the PDLC

system in comparison with the monomer and LC components used for its preparation.  
Chapter 7 will briefly summarize the PhD work.

## Chapter 2 Introduction to Solid State NMR

This chapter will focus on the principle of solid state NMR (SSNMR) and the techniques applied in SSNMR, including magic angle spinning, cross polarization and high power decoupling. In addition, the basic concepts of relaxation are described; and the techniques for determining relaxation times are given, such as inversion recovery and spin echo. Furthermore, the details of setting up SSNMR experiments are presented.

### 2.1 NMR in solution and in the solid state

From a practical point of view, many systems cannot be studied by solution NMR. Solid state NMR can be powerfully used to determine the structure of solid materials and also of gel-like or viscous samples, which cannot be dissolved in a solvent. Furthermore, in many systems, adding a solvent will destroy the special conditions under which the sample is to be investigated, preventing one from performing solution state NMR. However, SSNMR can offer reliable and approachable methods to investigate such systems.

In the following sections, only basic concepts of solid state NMR,<sup>[62]</sup> such as magic-angle spinning (MAS) and cross polarization (CP), and of NMR relaxation are described. The theoretical background of relaxation,<sup>[63]</sup> can be found in Chapter 6, and the principle of NMR diffusometry<sup>[61, 64]</sup> in Chapter 5. A more detailed discussion and further concepts of NMR can be found in many books, for example in references.<sup>[65-73]</sup>

There are two main factors which affect the NMR of solid samples: chemical shift anisotropy (CSA) and dipole-dipole (DD) interactions. Therefore solid samples usually give very broad lines with low resolution by using solution NMR techniques.<sup>[67, 71, 72, 74]</sup> Generally, dipole-dipole interactions produce a “Pake line shape”<sup>[75]</sup> with a line width of several kHz or more.

Both CSA and DD interactions occur in solution NMR but they generally average to zero as a result of the fast reorientation of the molecules. The difference between the

solid and solution state spectra of polystyrene as shown in figure 2.1 is obvious.

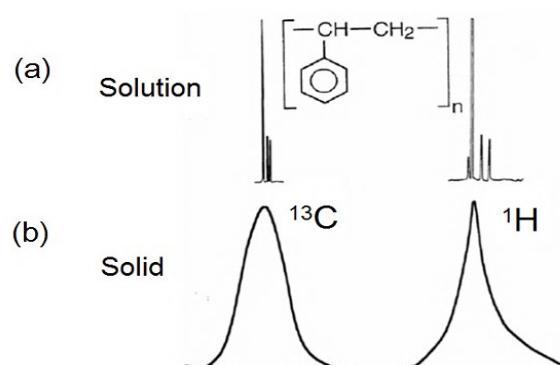


**Figure 2.1:**  $^{13}\text{C}$  and  $^1\text{H}$  NMR spectra of polystyrene: (a) solution spectra and (b) solid sample.<sup>[69]</sup>

Molecules in solid samples cannot reorient fast enough at the time scale of the NMR measurement and therefore yield poorly resolved spectra, from which little information on the molecular structure can be obtained. Generally, magic angle spinning, cross polarization, multiple-pulse sequence and high power decoupling are essential techniques to enhance the resolution of a solid spectrum. In this thesis, MAS and CP will be described in detail.

The most important approach to average the chemical shift and to weaken the dipole interaction in order to yield resolved spectra<sup>[76]</sup> is magic angle spinning. Another method is the dipolar decoupling of heteronuclei from protons. High power decoupling averages the proton spin distribution in different states to reduce the heteronuclear dipolar coupling. This removes the interaction between  $^1\text{H}$  and the X ( $^{13}\text{C}$ ,  $^{15}\text{N}$ ,  $^{31}\text{P}$ ) nuclei. Cross polarization is a trick to enhance the signal-to-noise ratio of the dilute nuclei such as  $^{13}\text{C}$  and  $^{15}\text{N}$ . Transfer of magnetization from the highly abundant nuclei ( $^1\text{H}$ ) to the lowly abundant nuclei ( $^{13}\text{C}$ ) is the principle of the technique. Further details can be found in the book by Duer.<sup>[62]</sup>

## 2.2 Chemical shift anisotropy (CSA)

The anisotropic chemical shift is the main reason for solid samples showing broad NMR spectra. In addition to the applied magnetic field, the electrons of the molecule produce secondary magnetic fields which make a contribution to the chemical shift of

the nuclei in the molecule.

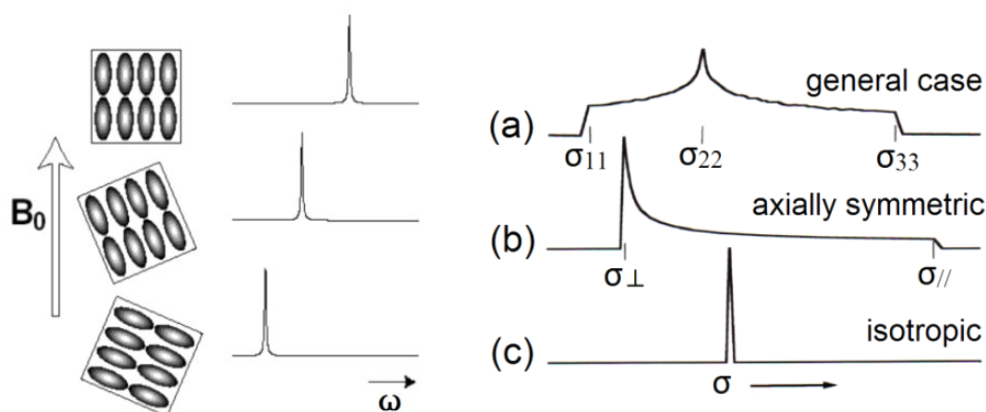


**Figure 2.2:** Left: The CSA results in an influence of molecular orientations on the resonance frequency.<sup>[63]</sup> Right: (a) Schematic of a powder pattern for anisotropic chemical shielding with  $\sigma_{11} \neq \sigma_{22} \neq \sigma_{33}$  (general case), (b) Pattern for axial symmetry where  $\sigma_{11} = \sigma_{22} = \sigma_{\perp}$  and  $\sigma_{33} = \sigma_{\parallel}$ . (c) Average of three principal values,  $\sigma_{\text{iso}} = (\sigma_{11} + \sigma_{22} + \sigma_{33})/3$ .  $\sigma$  is the chemical shielding tensor with principal values  $\sigma_{11}$ ,  $\sigma_{22}$  and  $\sigma_{33}$ .

In liquids, isotropic and rapid tumbling averages out the anisotropy of the chemical shifts. In solid or solid-like, even gel-like samples, these interactions are usually not completely averaged out due to the “fixed” confinement of the molecules on the time scale of the NMR experiments. The position of the NMR signal is related to the extent of shielding by the electrons, which is determined by the structure and orientation of a molecule. In a spherically symmetric molecule, the chemical shift is independent of molecular orientation. For an asymmetric molecule, the chemical shift is dependent on the orientation. The magnetic field experienced by the nucleus varies as a function of the orientation of the molecule in the magnetic field as shown in the left part of figure 2.2. This orientation dependence of the chemical shift is referred to as chemical shift anisotropy.<sup>[65]</sup> A powder with different orientations with respect to the magnetic field will cover a large range of frequencies and result in a broad line shape. Asymmetric molecules present an appearance as in figure 2.2a. An axially symmetric powder pattern is shown in figure 2.2b. For nuclei in an environment of cubic symmetry, the shielding will be independent of the orientation and the spectrum will be a single peak as in figure 2.2c.

### 2.3 Magic angle spinning (MAS)

The chemical shift anisotropy collapses to the isotropic chemical shift by using the magic angle spinning technique with the magic angle  $\beta = 54.7^\circ$  (Fig. 2.3a).<sup>[68]</sup> The mechanical design of the MAS system (Bruker) used in our lab is shown in Fig. 2.3b. Magic angle spinning was first described by Andrew<sup>[77]</sup> in 1958 and by Lowe<sup>[76]</sup> in 1959. The name of "magic-angle spinning" was coined in 1960 by Gorter at the AMPERE congress in Pisa.<sup>[78]</sup>

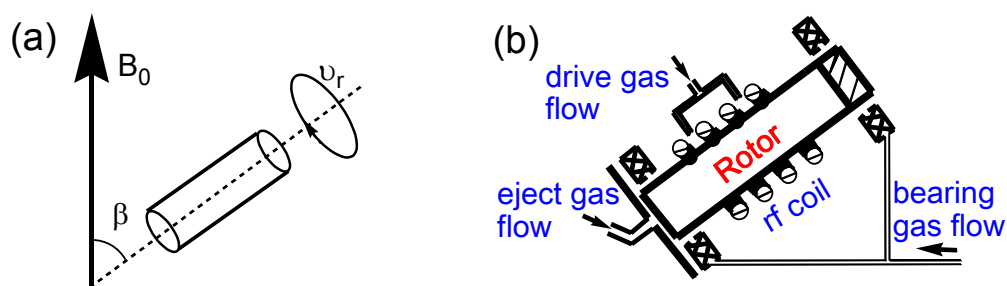


**Figure 2.3:** (a) Schematic presentation of MAS. (b) The design of a magic angle spinning probe. Schematic of a sample holder, rotating on air bearings within a stator, aligned at an angle of  $54.7^\circ$  to the vertical magnetic field  $B_0$ .

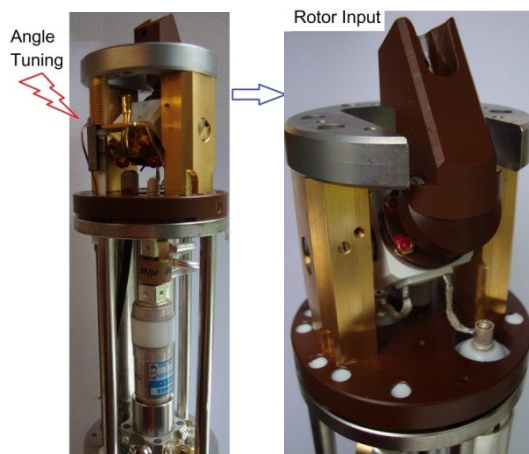


**Figure 2.4:** The MAS probe for rotors of 4 mm diameter used in our lab.

Figure 2.4 shows the 4mm MAS probe used in our NMR lab. To achieve an optimal spectrum, it is very important to set the angle exactly to the magic angle of  $54.7^\circ$ . The magic angle is adjusted through monitoring the number of  $K^{79}\text{Br}$  spinning side bands, as described in section 2.6.

## 2.4 Cross polarization (CP)

Due to the slow relaxation and low abundance of  $^{13}\text{C}$  in nature, it is difficult to get sufficient signal. To measure  $^{13}\text{C}$  spectra by direct excitation of the  $^{13}\text{C}$  spins is very time consuming. The cross polarization (CP) technique transfers the magnetization from the abundant nuclei (labeled I; examples:  $^1\text{H}$ ,  $^{19}\text{F}$ ) to the rare nuclei (labeled S; examples:  $^{13}\text{C}$ ,  $^{15}\text{N}$ ).<sup>[79]</sup> Thus CP increases the sensitivity in the NMR of the lowly abundant nuclei. The magnetization transfer is achieved by heteronuclear dipolar interaction. There are two advantages of CP. The first one is an increase in the signal intensity of the dilute nuclei since their gyromagnetic ratio  $\gamma$  is usually lower. The possible gain in intensity is given by  $\gamma_I/\gamma_S$ . Besides, CP allows us to shorten the time between subsequent scans because the relaxation time  $T_1$  of the abundant nuclei is shorter than  $T_1$  of the rare nuclei.<sup>[68]</sup> Therefore, a shorter measuring time is needed compared to the experiment without CP.

The mechanism of CP can be explained by the concept of spin temperature. The population of the energy levels of the spin system is given by a Boltzmann distribution with a parameter  $T$  defining the spin temperature.<sup>[80-82]</sup> The spin temperature ( $T$ ) can be defined as  $T=\infty$  when the high and low energy levels are occupied by the same number of spins;  $T>0$  when the low level contains more spins than the high level. An inverse population distribution corresponds to  $T<0$ . The abundant polarized I spins can be artificially treated as low-temperature system and the rare unpolarized S spins can be considered as high-temperature system. By thermally contacting the two systems, heat will start to flow from the S spins to the I spins. Therefore, the spin temperature of the S spins will drop meaning that the population difference between the lower and upper state is increased leading to an increased sensitivity in NMR. In the laboratory frame, I and S spins have different gaps between energy levels and magnetization cannot be transferred from one spin system to the other. However, in the rotating frame, adjusting the pulse power to match the energy gaps of I and S spins allows magnetization to be exchanged between I and S. This condition is called Hartman-Hahn (H-H) matching. CP is basically accomplished by using a  $90^\circ$  pulse at the



resonance frequency of the abundant nuclei, followed by a spin-lock. To accomplish a good thermal contact between the rare S and the abundant I spin systems the Hartmann-Hahn match condition must be fulfilled.<sup>[79]</sup> In the most common case of  $^{13}\text{C}$  (index C) and  $^1\text{H}$  (index H) the Hartmann-Hahn condition is

$$\gamma_{\text{H}}B_{1\text{H}} = \gamma_{\text{C}}B_{1\text{C}} \quad (2.1)$$

Here  $\gamma$  is the gyromagnetic ratio and  $B_1$  is the rf induced field.

A typical CP pulse sequence for  $^1\text{H} \rightarrow ^{13}\text{C}$  CP is shown in figure 2.5. A  $90^\circ$  pulse converts the z-magnetization of  $^1\text{H}$  into transverse magnetization, which will partly transfer to  $^{13}\text{C}$  under the Hartmann-Hahn match condition with spin lock. Finally, the signal of carbon will be detected with proton decoupling.

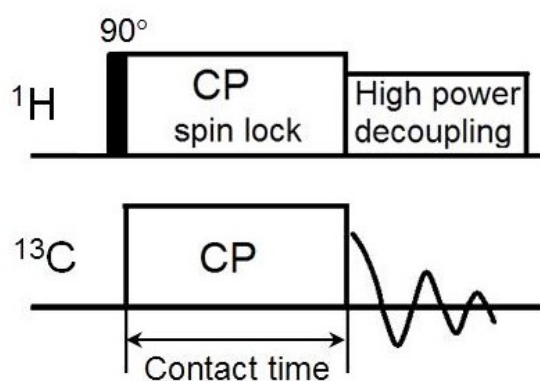


**Figure 2.5:** The standard cross polarization pulse sequence, taking the case of  $^1\text{H}$ - $^{13}\text{C}$  as an example.

Figure 2.6 explains the spin lock procedure using the vector model. In (a), in the absence of a spin lock pulse, the transverse magnetization will decay with the spin-spin relaxation time  $T_2$ . When rf irradiation (phase shifted by  $\pm 90^\circ$ ) is maintained (b), the magnetization  $M$  remains along the  $B_1$  magnetic field, namely spin-locked.<sup>[68]</sup> The magnetization will decay exponentially with a different time constant, the spin-lattice relaxation time  $T_{1\rho}$  in the rotating frame.

Cross polarization can be achieved when simultaneously to the spin-lock pulse on the protons a pulse (of arbitrary phase) irradiates the carbon spins. Then the protons are precessing about the  $B_{1\text{H}}$  field with a frequency of  $\gamma_{\text{H}}B_{1\text{H}}$  and the carbons about the  $B_{1\text{C}}$

field with a frequency of  $\gamma_C B_{1C}$ . When the Hartmann-Hahn match condition is established, these frequencies are equal. Hence the z-components of the proton and carbon nuclei have the same time dependence. Because of that, spin flip flops, a process of magnetization exchange between two spins can take place between the protons and carbons. In theory, an enhancement by the ratio of the  $\gamma$  values for the abundant and rare spins can be found in NMR spectra. This ratio is  $\sim 4$  in the case of  $^1\text{H}$  and  $^{13}\text{C}$ .

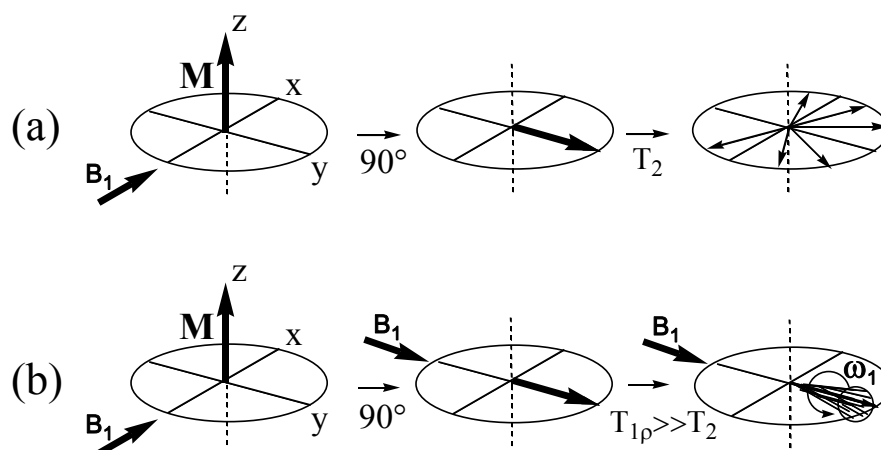


**Figure 2.6:** Spin locking process. (a) without spin locking field  $B_1$ ; (b) with spin locking field  $B_1$ .

## 2.5 Spin relaxation

There are two essential kinds of relaxation processes in NMR, namely spin-lattice ( $T_1$ ) and spin-spin ( $T_2$ ) relaxation. In this section, we will focus on the principle of spin-lattice relaxation. Additionally, the inversion recovery method for obtaining  $T_1$  is described. Furthermore, the spin echo is discussed, which is employed in many applications, such as diffusion measurements (cf. Chapter 5). The relationship between the correlation function of molecular motion and spin relaxation as well as pulse sequences for the measurement of spin-lattice relaxation in the rotating frame ( $T_{1\rho}$ ) will be discussed in Chapter 6.

### 2.5.1 Spin-lattice relaxation

The spin-lattice relaxation time  $T_1$  represents the "lifetime" of non-equilibrium  $z$ -

magnetization. It is the characteristic time constant of the first order rate process that returns the magnetization to the Boltzmann equilibrium along the z-axis.  $T_1$  is the characteristic time required by the spins, after rf excitation, to go back to thermal equilibrium magnetization. Spin-lattice relaxation, also called longitudinal relaxation, is a process through which the equilibrium population in spin states is reached after a perturbation of the population. This process requires an energy transfer between the spin system and the lattice, which is in equilibrium.<sup>[83]</sup> Therefore,  $T_1$  can also be thought of as the time it takes the energy of a spin to flow to its surroundings, or "lattice".

The rate of approach to equilibrium for the magnetization is proportional to the separation value from equilibrium, and is governed by the equation:

$$\frac{dM_Z}{dt} = \frac{M_\infty - M_Z}{T_1} \quad (2.2)$$

Here  $M_\infty$  is the final magnetization value corresponding to equilibrium,  $M_Z$  is the magnetization at time t and  $T_1$  is the spin-lattice relaxation time.

The solution of the above equation is:

$$M_Z(t) = M_\infty + (M_0 - M_\infty)\exp(-\tau/T_1) \quad (2.3)$$

$M_0$  is the initial value of magnetization.

### 2.5.2 Inversion recovery

The inversion recovery method, shown in figure 2.7, can be used to measure the spin-lattice relaxation time,  $T_1$ . First, a 180° pulse is applied to the sample to rotate the net magnetization from the +z to -z. After some time  $\tau$ , an additional 90° pulse is applied to produce transverse magnetization for detection. Figure 2.7 shows how the net magnetization changes with the delay  $\tau$ . The simplest way to get  $T_1$  is to divide the delay  $\tau$  when the signal is equal to zero by  $\ln 2$ . However, this calculation contains a large uncertainty. A better method is measuring the spectra as a function of the delay  $\tau$  and fitting the curve to get the precise value. When  $t=0$ ,  $M_Z = -M_\infty$ , therefore equation (2.3) gives:

$$M_Z = M_\infty(1 - 2\exp(\frac{-\tau}{T_1})) \quad (2.4)$$

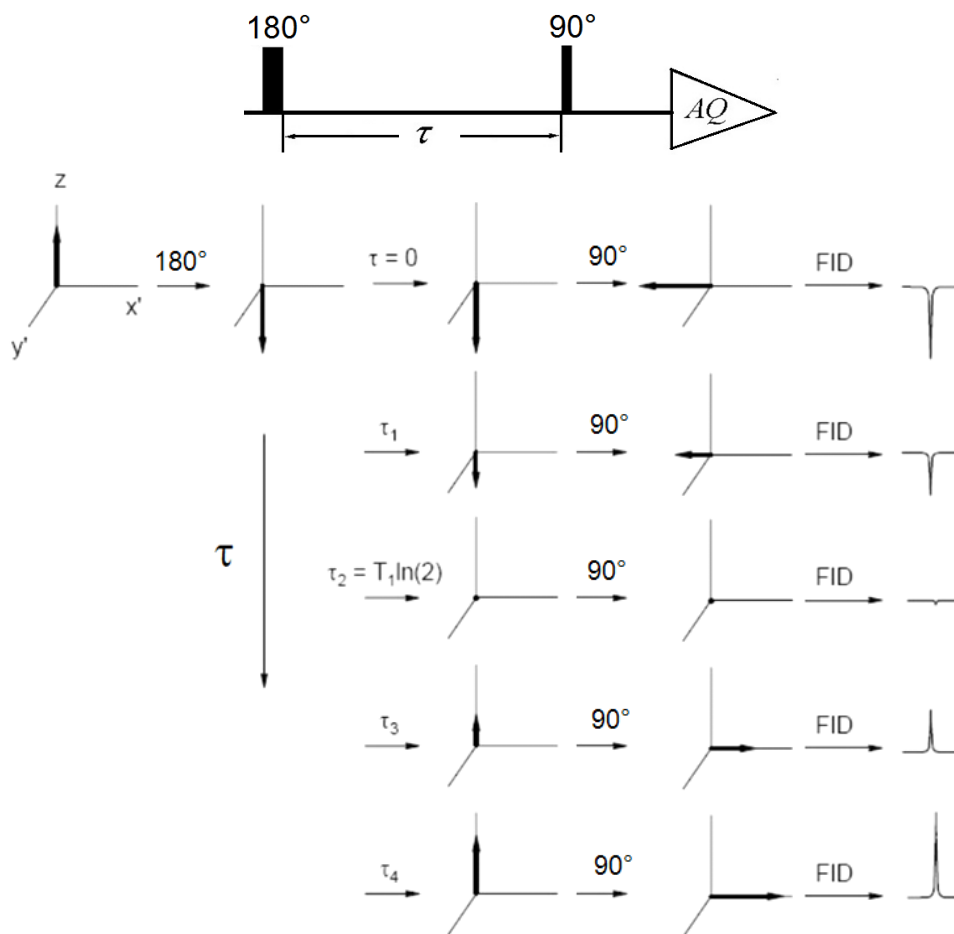


**Figure 2.7:** Pulse sequence and magnetization trajectories for the inversion recovery method to measure  $T_1$ .<sup>[84]</sup>

The relaxation of E7 is taken as an example. The dependence of the proton spectra on  $\tau$  obtained in a series of measurements is shown in figure 2.8. The  $T_1$  value of each peak can be obtained by fitting the peak intensities to equation (2.4). The aromatic proton at 7.3 ppm of E7, for example, shows a longitudinal relaxation time of 637 ms as indicated in the fitting window of the Tecmag software.

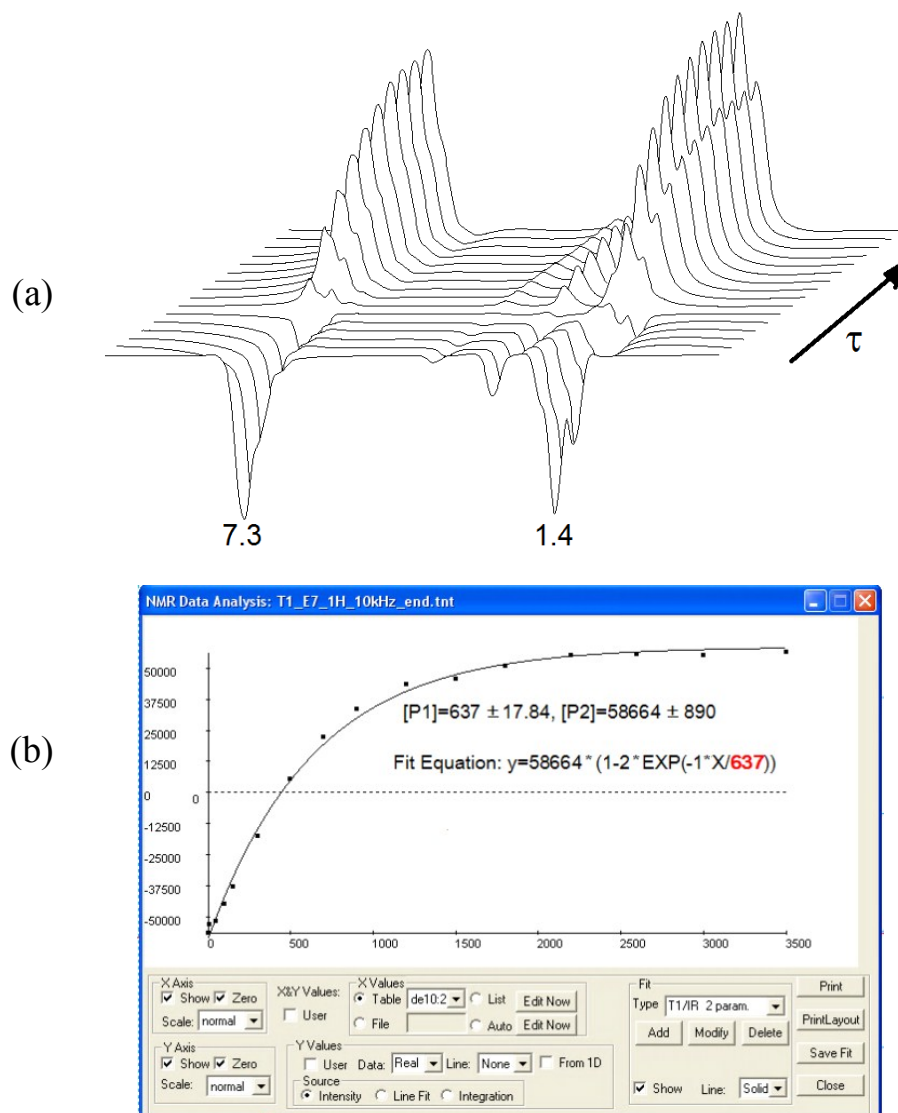


**Figure 2.8:** Inversion recovery experiment. (a) <sup>1</sup>H NMR spectra of E7 as a function of the recovery delay  $\tau$ ; (b) Plot of  $M_z$  for the aromatic protons of E7 vs.  $\tau$  (ms) in a series of measurements with varying  $\tau$ .

### 2.5.3 Spin echo

Because of interactions between spins, the magnetization suffers from dephasing and decays to zero after it has been rotated into the xy plane by a pulse. This decay can be partly reverted and a spin echo can be obtained. Figure 2.9 demonstrates the spin echo experiment. A 90° pulse is applied to tilt the spins into the xy plane. At time  $t=0$ , all the magnetization is aligned along a common axis (y in Fig. 2.9) in the xy plane. The spins precess about the z-axis with different frequencies. Referring to the rotating reference frame, some spins travel in one direction and others travel in the opposite

direction. The dephased spins produce a signal with attenuated intensity. However, if a  $180^\circ$  pulse is applied at the appropriate time,  $t=\tau$ , the spins are flipped (rotated by  $180^\circ$  about the pulse axis) and instead of traveling away from each other, they travel towards each other, and rephase along the  $-y$ -axis at the time  $t=2\tau$ . This rephasing after the  $180^\circ$  pulse is called a spin echo.<sup>[83]</sup>

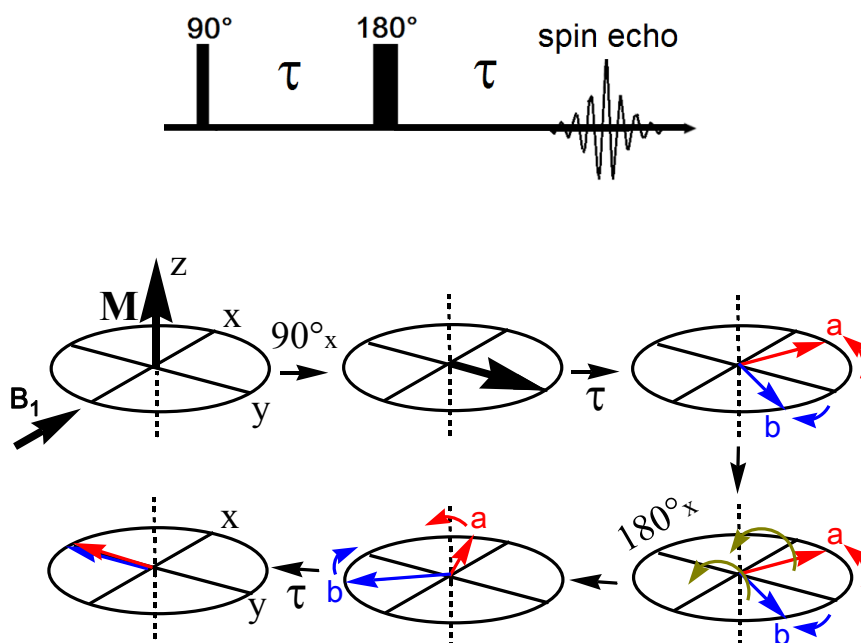


**Figure 2.9:** The pulse sequence and the magnetization trajectories for the spin echo experiment: the individual spins (a and b) precess at different Larmor frequencies during the  $\tau$  period, the  $180^\circ_x$  pulse causes a phase shift of the spins. The individual spins continue their precession during the next  $\tau$  period and refocus on the  $-y$ -axis.

The spin echo has many applications. One application is the detection of the broad spectra of solids. In the NMR measurement, detection cannot be performed immediately after the rf pulse due to the strong power of the pulse and the structure of the coil. During the time gap between pulse and detection (dead time), the spins dephase and the intensity is reduced. Spin echo detection can enhance the intensity. Due to the dephasing caused by spin-spin interactions, the spin echo also can be used to determine the transverse relaxation time  $T_2$ . Moreover, the spin echo is very important in NMR diffusometry, which is discussed in Chapter 5.

## 2.6 Setting up CPMAS experiments

### 2.6.1 Magic angle adjustment

The following description is basically according to the instruction of Taylor.<sup>[85]</sup> To set the angle precisely at  $54.7^\circ$ , a standard reference sample of KBr is chosen to find the magic angle.  $^{79}\text{Br}$  has a large natural abundance and a gyromagnetic ratio similar to  $^{13}\text{C}$ , giving a resonance within the bandwidth of most  $^{13}\text{C}$  probes. The central resonance of the quadrupolar spectrum of the  $I=3/2$  nucleus is used. Sample spinning results in spinning side bands (SSBs) over the range of the quadrupolar spectrum.

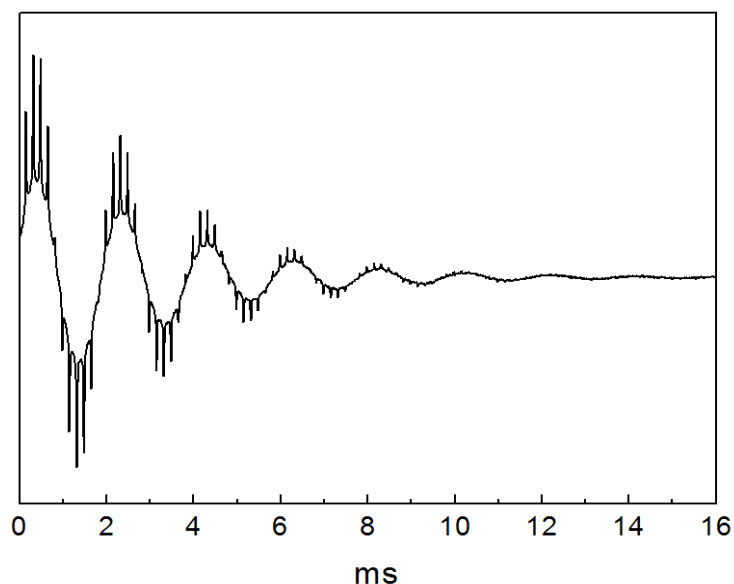


**Figure 2.10:** The FID of  $\text{K}^{79}\text{Br}$  at the magic angle, showing many rotor echo spikes.

Generally, there are two ways to check the angle: free induction decay (FID) and spectrum. The FID is more sensitive to misadjustments of the angle than the spectrum. When the spikes (rotor echoes), which can be seen in figure 2.10, become more and more, we are closer to the magic angle. Otherwise, we are far away from the magic angle. Anyway, it is easy to find the correct angle when you play with it. During the angle set up, the spin rate should be kept constant. Alternatively, the spectrum obtained by FT can offer another view for us to find the magic angle. The procedure works in a similar way: the more and higher spinning side bands occur, the closer the angle is to the magic value.

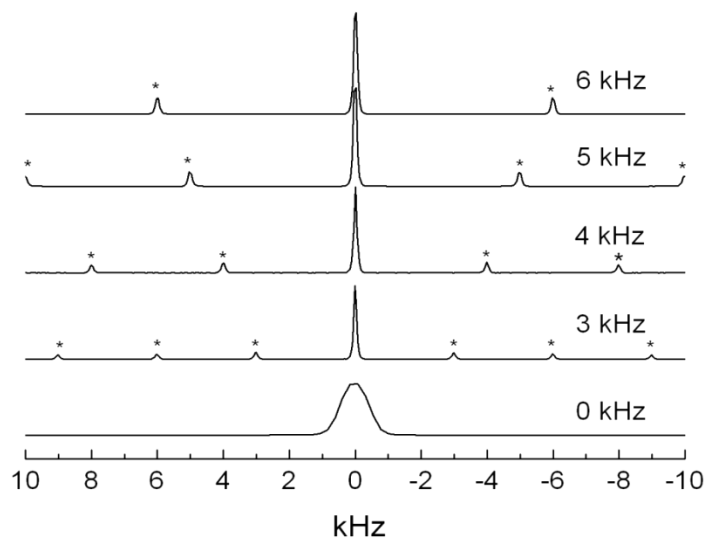


**Figure 2.11:** Spectra of  $K^{79}\text{Br}$  as a function of spin rate under MAS.

Figure 2.11 illustrates the effect of MAS on the  $^{79}\text{Br}$  NMR spectrum of KBr. As expected, solid  $K^{79}\text{Br}$  shows a broad signal under static conditions (0 kHz). As the spinning frequency increases, the number and intensity of SSBs decrease. The SSBs will disappear completely when the spin rate is large enough compared to the anisotropy of the interaction (here: quadrupolar coupling). Meanwhile, the central peak increases in intensity and stays at the same position. Last but not least, it should be pointed out that the distance between SSBs and the central peak is an integral number times the spinning rate.

Similar to the results of  $K^{79}\text{Br}$ ,  $^1\text{H}$  spectra show the same trends when the spinning rate is varied (cf. Fig. 2.12). The larger the spinning rate, the higher the resolution of the spectrum. However, due to the strong homonuclear interaction of protons, adamantane shows broad lines even under MAS.



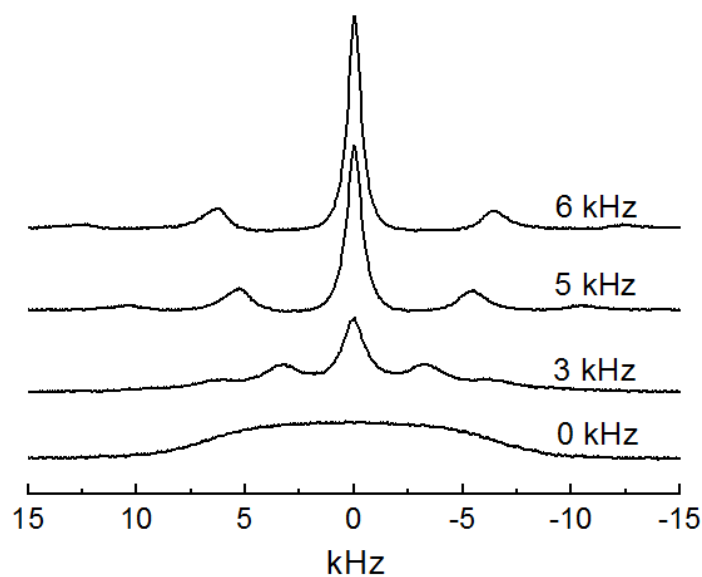


**Figure 2.12:**  $^1\text{H}$  spectra of adamantane as function of spinning rate under MAS.

### 2.6.2 Cross polarization

In practice, a  $90^\circ$  pulse is applied to rotate  $^1\text{H}$  spins into the xy plane, and the power of the spin lock pulse is kept constant. Adjust the power of the  $^{13}\text{C}$  CP pulse by tuning amplifier and attenuation to get Hartmann-Hahn matching. Under the Hartmann-Hahn condition, both  $^1\text{H}$  and  $^{13}\text{C}$  have the same precession frequency, and cross polarization from  $^1\text{H}$  to  $^{13}\text{C}$  happens. The signal in the  $^{13}\text{C}$  channel has maximum intensity.

To demonstrate the advantage of MAS and CP in SSNMR measurements, experiments on  $^{13}\text{C}$  of adamantane with different methods are compared in figure 2.13. The static ( $\omega=0$  kHz) measurement with CP shows quite broad peaks with a linewidth of about 280 Hz, which is fairly narrow for a solid due to the fast reorientation and the symmetric lattice of solid adamantane. Spinning the sample at  $\omega=5$  kHz without proton decoupling during signal recording gives a narrower linewidth of 88 Hz. Further removing the coupling to protons by high-power decoupling improves the resolution and reduces the line-width to 18 Hz. Finally, combining MAS and CP as well as decoupling provides the best spectrum with stronger signal and the same narrow linewidth.

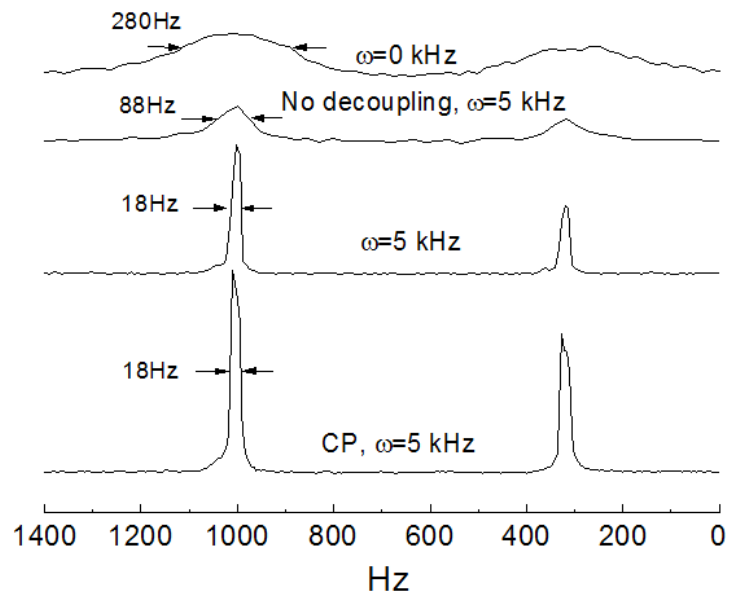


**Figure 2.13:** The effect of MAS, CP and decoupling on the  $^{13}\text{C}$  spectrum of adamantane

For solids, such as glycine, in which the molecules do not move, a  $^{13}\text{C}$  spectrum cannot be easily obtained without CP. Glycine is used as standard sample to check the Hartmann-Hahn condition. While CP is very efficient for crystalline samples, it does not work for fast reorienting samples, such as TMPTA and other liquids.

## Chapter 3 Sample Applications of Solid State NMR

In the previous chapter, the basic theory and set up of  $^{13}\text{C}$  CPMAS NMR were described. This chapter will present several examples of applications of NMR to solid samples. The spectra shown were measured for different projects carried out in collaboration. In addition, taking 4-cyano-4'-pentylbiphenyl (5CB) as an example,  $^1\text{H}$  spectra and their temperature dependence were used to determine the phase transition and order parameter of a liquid crystal.

### 3.1 $^{13}\text{C}$ spectroscopy of diosgenin derivatives

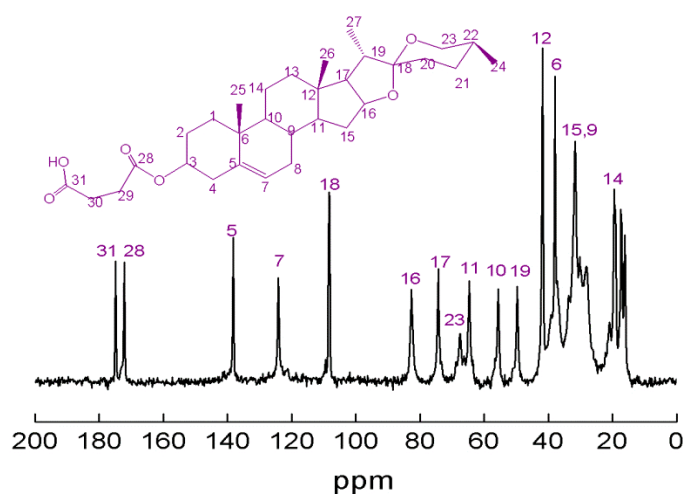
The basic application of NMR is to determine a molecular structure by analyzing NMR spectra. This requires good spectral resolution, which can be achieved for solids in  $^{13}\text{C}$  NMR spectra. This is illustrated here, using organic molecules with a fairly large number of carbon sites as example.

In collaboration with Javier Perez Quinones, as part of his project on drug delivery systems consisting of diosgenin-functionalized chitosan,<sup>[86]</sup>  $^{13}\text{C}$  spectra of solid diosgenin derivatives were measured. CPMAS was applied to record  $^{13}\text{C}$  spectra of the samples, which appear as white powder samples. In general, varying the spinning rate is the easiest way to check if spinning side bands (SSB) occur. Here,  $^{13}\text{C}$  spectra measured at spinning rates of  $\omega=5$  and  $\omega=8$  kHz were chosen to check the SSB in spectra. No difference can be found between two spectra measured at those spinning rates, indicating that no SSB are present, not even in the spectrum recorded at 5 kHz. Therefore,  $\omega=5$  kHz was chosen for the  $^{13}\text{C}$  spectra measurements of both diosgenin monosuccinate (MSD) and monomaleate (MMD). The peak at 38 ppm of the secondary carbon atom in adamantane was used as reference for all spectra listed below.

#### 3.1.1 Diosgenin monosuccinate (MSD)

Figure 3.1 shows the well resolved  $^{13}\text{C}$  spectrum and the structure of MSD. According to the prediction of a ChemDraw calculation and the spectra analyzed by Wawer,<sup>[87]</sup> it

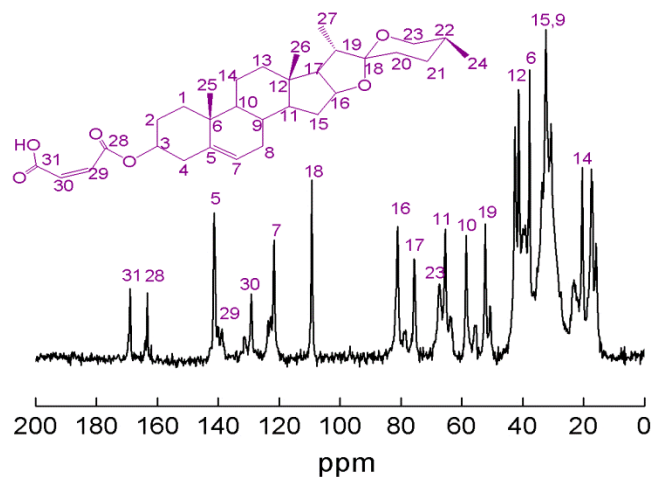
is easy to assign the peaks that appear in the chemical shift range of 100-170 ppm. Carbons of carbonyl C=O have the largest chemical shifts (C<sub>28</sub> and C<sub>31</sub>). The signals of C<sub>5</sub> and C<sub>7</sub> appear at 138 and 123 ppm, respectively, due to the double C=C bond. The peak of C<sub>18</sub> is at 108 ppm because of the strong electronegativity of two connected oxygen atoms. In the range of low chemical shifts, some carbons, such as C<sub>15</sub> and C<sub>9</sub>, have very similar chemical shifts and their peaks overlap with each other due to the very similar chemical environments.



**Figure 3.1:** <sup>13</sup>C spectrum and the assignments of MSD. Measured under CPMAS at  $\omega=5$  kHz at 298 K, 2048 scans.

### 3.1.2 Diosgenin monomaleate (MMD)

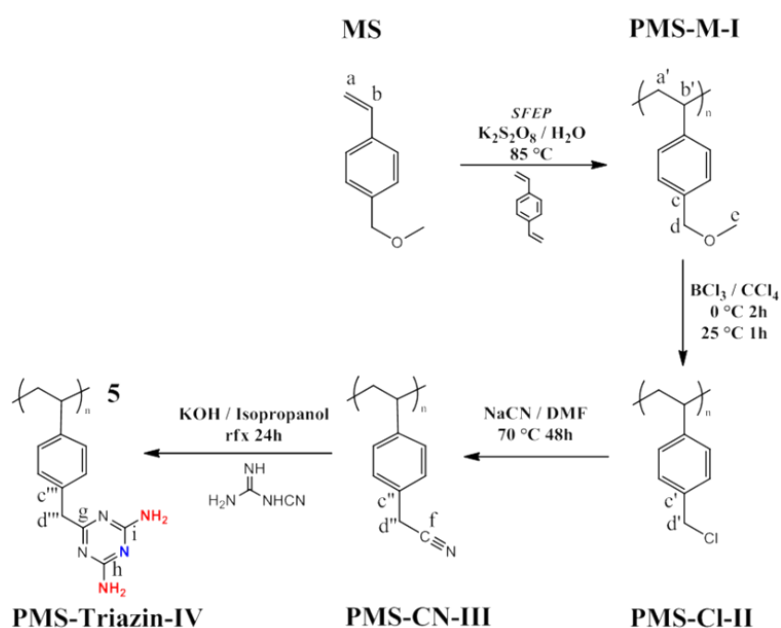
Figure 3.2 presents the <sup>13</sup>C spectrum of MMD. Due to its structure similar to MSD, MMD shows a similar <sup>13</sup>C spectrum compared with figure 3.1. The peaks of C<sub>29</sub> and C<sub>30</sub> shift to the high ppm range because of the C=C double bond in MMD. In addition, carbons C<sub>29</sub> and C<sub>30</sub> show a conjugation with C<sub>28</sub> and C<sub>31</sub> resulting in a shift to lower ppm values compared with MSD. Several small peaks appearing in the ranges of 45-80 ppm and 120-140 ppm indicate the presence of impurities.



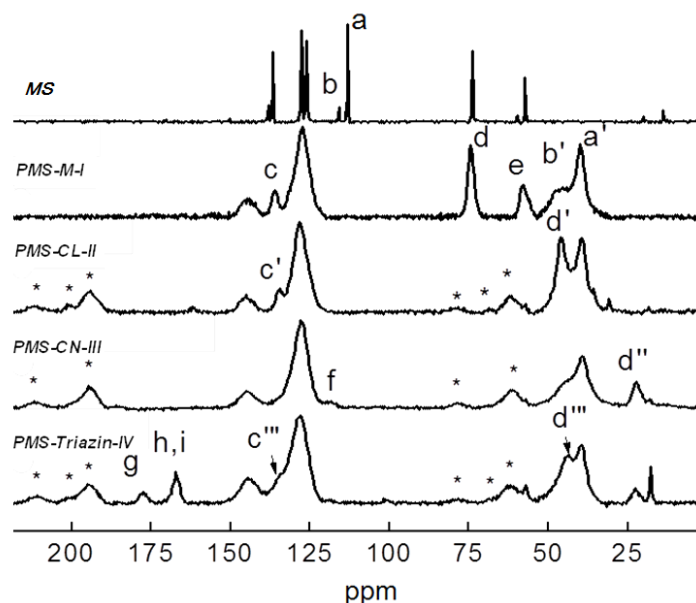
**Figure 3.2:**  $^{13}\text{C}$  spectrum and the assignments of MMD. Measured under CPMAS at  $\omega=5$  kHz at 298 K, 2048 scans.

### 3.2 Chemical modification of polymer colloids

Another important application of SSNMR is to verify chemical reactions, especially for insoluble products. In cooperation with Frank Bayer in Klaus Huber's group on the preparation of binary colloidal crystals, spectra of each reaction step proved that the functionalization of the colloids was successful.<sup>[88]</sup> The reaction steps and spectra are shown in figure 3.3 and figure 3.4, respectively.



**Figure 3.3:** Scheme of the synthesis of colloidal particles functionalized with a hydrogen-bond donor-acceptor-donor (DAD) group.



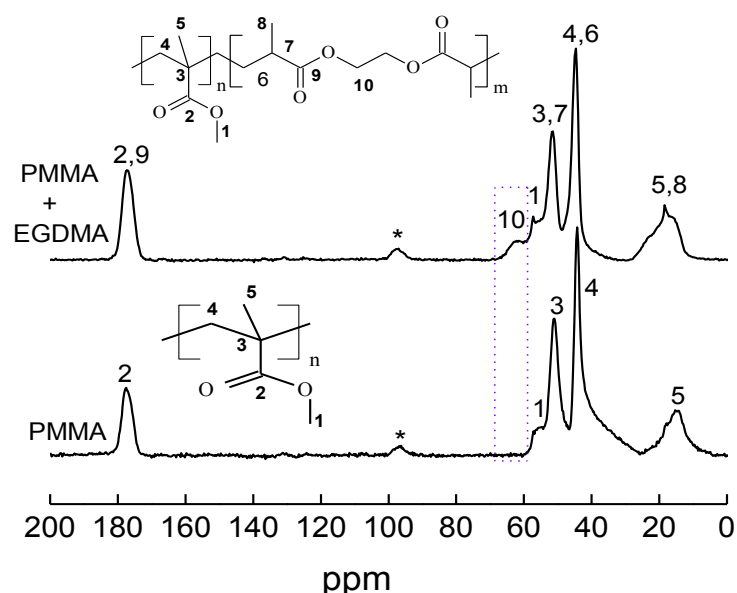
**Figure 3.4:**  $^{13}\text{C}$  CPMAS spectra of the monomer 1-(methoxymethyl)-4-vinylbenzene (MS) and the polymer colloids resulting after polymerization and several functionalization steps. Spectra were obtained at a spinning rate of 5 kHz. Peak labels refer to figure 3.3.

Figure 3.4 shows the spectra of the monomer and of the polymer colloids after each modification step. Two peaks at 113 and 116 ppm (labeled a and b) are assigned to the C=C group carbon atoms of monomer MS. These two peaks disappear in the spectrum of the 4-methoxymethyl functionalized colloid (PMS-M-I). However, two new peaks, a' and b', appear at 39 and 46 ppm, respectively. They can be assigned to the polymer backbone. This indicates that the polymerization was complete. The polymer peaks are much broader than those of the monomer or those of crystalline organic compounds like the diosgenin derivatives (cf. Fig. 3.1 and 3.2) since different constitutions and conformations of the amorphous atactic polymer lead to a spread in chemical shifts. The peak from the methoxy group of PMS-M-I (carbon atom e) at 58 ppm has vanished in PMS-Cl-II. Furthermore, due to the stronger negative inductive effect of chlorine compared to oxygen, the methylene peak at 74 ppm (d) is shifted to 45 ppm (d'). When chlorine is replaced by the nitrile group, the methylene peak formerly at 45 ppm (d') shifts further to 22 ppm (d'') in the spectrum of PMS-CN-III. An additional small peak appears at 118 ppm, which belongs to the carbon atom in the nitrile group

(f). Two distinguished peaks at 166 and 177 ppm stand for the amino-substituted carbon atoms h and i and for carbon atom g of the triazine group in the final colloid PMS-Triazin-IV. Two additional peaks are seen at 45 and 135 ppm, corresponding to carbon atoms d''' and c''', respectively. The remaining peak at 22 ppm shows that the last modification was not complete.

### 3.3 Composition determination

The properties and structure of colloid are directly dependent on the mass fraction of cross-linker in the colloidal polymer. To check the concentration of cross linkages in the polymer system,  $^{13}\text{C}$  spectra obtained by CPMAS can be used to determine the composition. Figure 3.5 shows well resolved spectra of pure poly(methyl methacrylate) (PMMA) and PMMA with cross-linker ethylene glycol dimethacrylate (EGDMA). The addition of EGDMA shows an additional peak (10) corresponding to carbon  $\text{C}_{10}$ . It overlaps with peak (1). Assuming that  $\text{C}_1$ ,  $\text{C}_2$ ,  $\text{C}_9$  and  $\text{C}_{10}$  share the same cross polarization rate, the relative concentration of cross linkage EGDMA may be roughly calculated from the integrated areas of these peaks.



**Figure 3.5:** Comparison of  $^{13}\text{C}$  spectra of PMMA with and without cross-linker ethylene glycol dimethacrylate (EGDMA). The chemical structure shown in the figure simply demonstrates the molar ratio of m and n, but not the actual cross-linked structure.

### 3.4 Determination of phase transitions of liquid crystals

For systems with phase transitions, such as liquid crystals, NMR offers an easy way to determine the phase transition temperature by measuring spectra or relaxation times as a function of temperature.

This is demonstrated here for the nematic-to-isotropic phase transition using  $^1\text{H}$  NMR. Figure 3.6 shows the temperature dependence of the  $^1\text{H}$  spectra of the liquid crystal 4-cyano-4'-pentylbiphenyl (5CB). At room temperature, 5CB shows a characteristic broad spectrum due to the strong dipolar interaction in the nematic phase. The doublet structure of the spectrum proves that the liquid crystal is aligned by the magnetic field. The sharp peaks on top of the broad spectra are from an impurity. Higher temperature reduces the molecular order of 5CB, which can be induced from the narrower line width of 5CB. The spectrum changes into very sharp peaks characteristic of an isotropic phase at 37 °C. No further change in the spectra is found under continued increase of the temperature to 39 °C. Therefore, 37 °C is the nematic-to-isotropic temperature  $T_{\text{NI}}$  of 5CB.

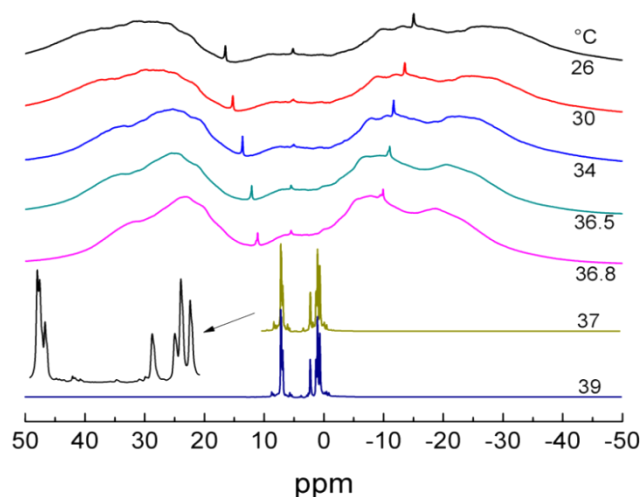


**Figure 3.6:** Temperature dependence of the  $^1\text{H}$  spectra of 5CB, measured under static conditions.

The overall doublet in the aligned nematic phase results from the couplings between the ortho and meta protons on one side of a phenyl ring. The axis between these protons is almost parallel to the director, which aligns parallel to the magnetic field.



Therefore, this particular proton pair has a stronger dipolar coupling than all other proton pairs and dominates the spectrum. The asymmetry of the doublet is due to differences in the chemical shifts of the protons. The total spectrum is a superposition of a large number of multiplets, each one centered at the chemical shift of a proton. Due to the huge number of peaks, they are not resolved and only broad humps are obtained.

As temperature increases the order parameter gets smaller and the molecules are aligned less and less along the director. Therefore all dipole couplings and therefore the overall width of the spectrum decreases. In the isotropic phase the dipole couplings are averaged to zero because of the isotropic tumbling of the molecules. Therefore, highly resolved spectra can be obtained (cf. Appendix A1.1).

The dipolar coupling is proportional to the nematic order parameter  $S$ . Although individual proton-proton couplings cannot be resolved, the overall splitting can be used to estimate the order parameters. (See Appendix A3 for Haller plot.)

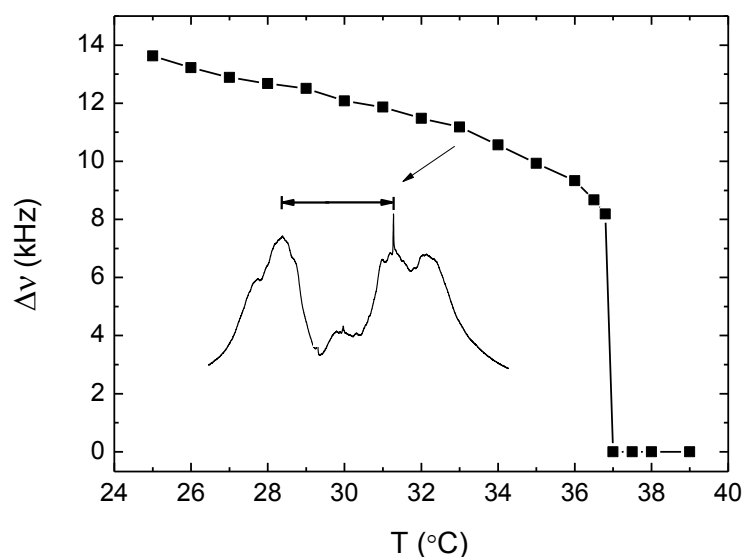


**Figure 3.7:** The splitting of the  $^1\text{H}$  spectra of 5CB as a function of temperature, the chosen splitting is indicated in the figure.

Figure 3.7 presents the temperature dependence of the dominating  $^1\text{H}$  splitting, which decreases as temperature increases. There is one big discontinuity when 5CB becomes isotropic. The phase transition  $T_{\text{NI}}$  measured here seems a little higher than 35 °C given

in reference.<sup>[89]</sup> This difference is probably due to the temperature gradient between the temperature sensor and the sample; the temperature control was not calibrated. This example demonstrates that NMR provides a simple approach for studying the phase transition of liquid crystals.

### **3.5 Conclusions**

In short,  $^{13}\text{C}$  CPMAS NMR can be a powerful tool to obtain well resolved spectra and provides a practical way for scientists to determine chemical structures and to distinguish or even quantify similar components in a system. Also wide-line  $^1\text{H}$  NMR has many applications, such as measuring phase transition temperatures and order parameters of liquid crystal molecules.

## Chapter 4 The PDLC System (P)TMPTA/E7: NMR Spectra and Polarizing Microscopy

In the previous chapters solid state NMR has been introduced and examples of its application have been given. This chapter will focus on the preparation of the PDLC system and the spectra assignments of the PDLC system and its precursors, on which the diffusion and relaxation measurements discussed in Chapter 5 and 6 have been performed. After an introduction of the system,  $^1\text{H}$  and  $^{13}\text{C}$  spectra of the liquid crystal E7 and the monomer TMPTA will be given. Then,  $^{13}\text{C}$  NMR spectra of the polymer PTMPTA and of the PDLC will be presented. Finally, the results of polarizing optical microscopy, applied to confirm the structure and the phase behavior of TMPTA/E7 mixtures, will be presented.

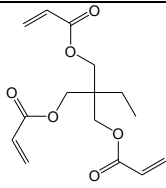
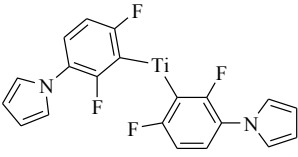
### 4.1 Materials

A PDLC system generally contains liquid crystal droplets dispersed in a polymer matrix. In this thesis, a PDLC based on the liquid crystal E7 and the monomer trimethylolpropane triacrylate (TMPTA) was chosen for the investigation. The liquid crystal E7 (purchased from Merck, Darmstadt, Germany) contains four nematic components. The composition of E7 is given in Table 4.1. TMPTA was purchased from UCB Chemicals, Belgium. Bis[2,6-difluoro-3-(1H-pyrrol-1-yl)phenyl]titanium (Irgacure 784, CIBA, Switzerland) is the photoinitiator for starting the polymerization. All chemicals were used without further purification and are listed in Table 4.2.

**Table 4.1:** Compositions of liquid crystal E7. Structures are shown in Fig.4.1a.

Component	Abbr	Sum formula	Weight fraction
4-cyano-4'-pentylbiphenyl	5CB	$\text{C}_{18}\text{H}_{19}\text{N}$	51 %
4-cyano-4'-pentylterphenyl	5CT	$\text{C}_{24}\text{H}_{23}\text{N}$	8 %
4-cyano-4'-heptylbiphenyl	7CB	$\text{C}_{20}\text{H}_{23}\text{N}$	25 %
4-cyano-4'-octyloxybiphenyl	8OCB	$\text{C}_{19}\text{H}_{21}\text{NO}$	16 %

**Table 4.2:** The structure and sum formula of monomer and photoinitiator.

Compound	Abbr	structure	Sum formula
Trimethylolpropane triacrylate	TMPTA		$C_{15}H_{20}O_6$
Bis[2,6-difluoro-3-(1H-pyrrol-1-yl)phenyl]titanium	Irgacure 784		$C_{20}H_{12}F_4N_2Ti$

## 4.2 Preparation of PDLCs

### Precursor mixtures

A typical example of the composition of a precursor mixture is 1 % Irgaruce 784, 49 % TMPTA, and 50 % E7. All components were dissolved in dichloromethane. Ultrasonication of the mixtures for 10 minutes results in homogeneous solutions. Mixtures were usually kept in the oven at 50°C for 24 h to completely evaporate the solvent.

Also mass fractions of 30, 50, 60, and 70 % liquid crystal E7 were chosen for the study. In the precursor mixtures, the concentration of the photoinitiator was always kept at 1 %.

### Polymerization-induced phase separation by laser

Holographic polymer-dispersed liquid crystals, studied by Andreas Redler in his PhD thesis<sup>[90]</sup> were fabricated by laser illumination. For better comparison with these systems, a PDLC sample containing 50 wt. % of the liquid crystal E7 and a sample of the pure polymer PTMPTA were generated by laser-initiated polymerization. The resulting products were used for diffusion measurements (cf. chapter 5). The photopolymerization was started with a laser beam from a frequency doubled Nd:YAG laser (532 nm) and focusing the resulting two beams on the precursor mixtures (two beams because we used the same laser set up as the one for holographic pattern

generation). The whole procedure was carried out in the dark room and it took about two hours.

### **Polymerization-induced phase separation by sun-light**

In contrast to the laser-induced polymerization, sun-light was applied to initiate polymerization. We found that this method is less energy and time consuming and it only took 10 minutes to complete the polymerization. Different precursor mixtures containing different concentrations of E7 were illuminated in this way. The PTMPTA and PDCLs considered in the following chapters were fabricated by this method, unless noted otherwise.

In the next section (4.3), the  $^1\text{H}$  and  $^{13}\text{C}$  NMR spectra of the precursor TMPTA and E7 will be discussed. Section 4.4.1 will present  $^1\text{H}$  NMR spectra for a polymer PTMTA and a PDLC sample under different spinning rates. These poorly resolved  $^1\text{H}$  spectra motivated us to measure  $^{13}\text{C}$  NMR spectra, which will be described in section 4.4.2.

### **4.3 Spectra of TMPTA, E7 and mixtures**

The spectra presented in this part were obtained with different spectrometers. Spectra recorded on different instruments look different because of different resolution. A 300 MHz Tecmag Apollo NMR spectrometer is used in our lab for solid state NMR measurements, while a 500 MHz Bruker Avance spectrometer with a high resolution probe was used for solution NMR without sample spinning. The spectra obtained with these 300 MHz and 500 MHz NMR spectrometers will be labeled as 300 MHz (UPB) and 500 MHz (UPB), respectively. The spectra, for which no information on the instrument is given, were all recorded on the 300 MHz Tecmag Apollo NMR (section 4.4).

#### **4.3.1 $^1\text{H}$ spectra**

##### **Pure E7 and TMPTA**

The chemical structures of the four components of E7 and the chemical shifts predicted by ChemDraw are shown in figure 4.1a. The species in the mixture are very

similar. Therefore, some peaks will not be resolved because they have very similar chemical shifts. In the following, atoms which share almost the same chemical shift are labeled with the same number. Due to the strong dipolar interaction, very high spinning rates ( $\sim 50$  kHz) would be needed to remove all spinning side bands and to get reasonably resolved  $^1\text{H}$  spectra in the nematic phase. Therefore, the spectrum measured at  $70^\circ\text{C}$  in the isotropic phase is chosen for peak assignment. The spectrum was measured on the bulk sample without solvent to avoid solvent effects on the chemical shift.

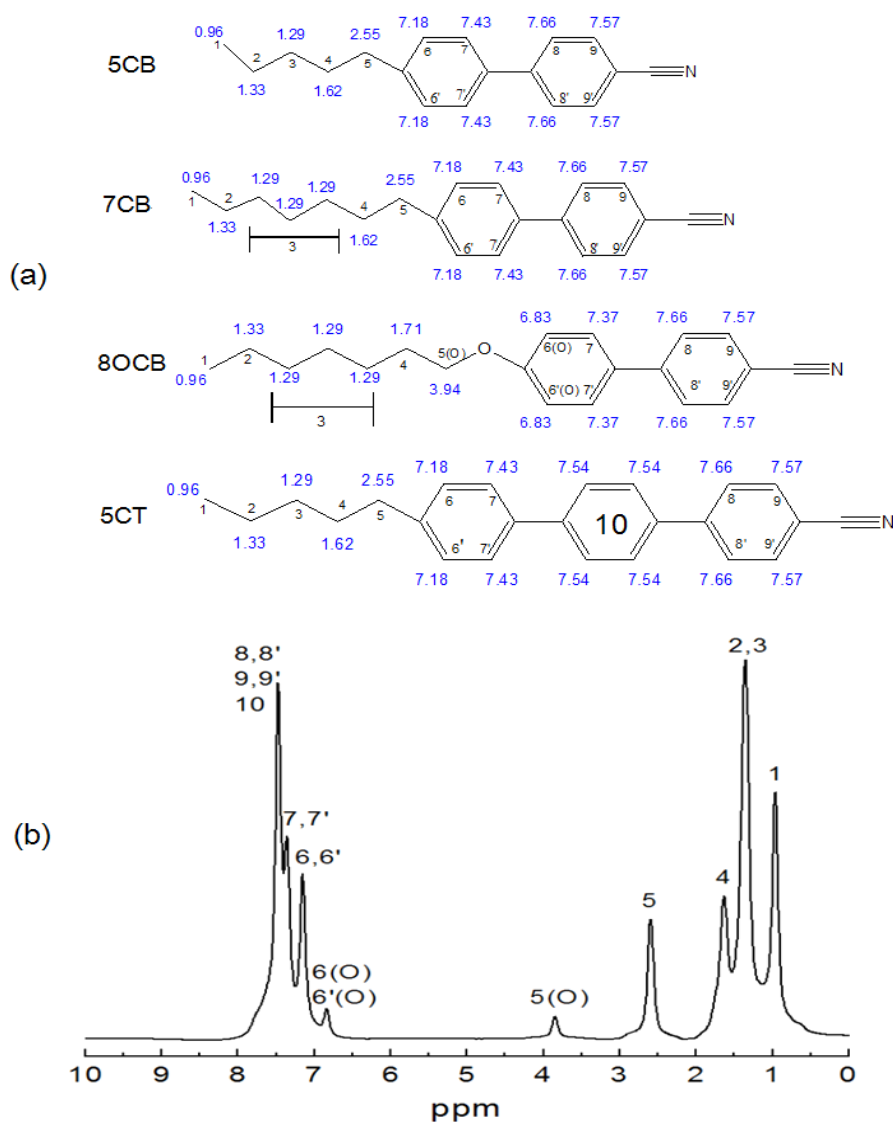


**Figure 4.1:** (a) The chemical shifts predicted by ChemDraw and the numbers of atoms used in the peaks assignments; (b)  $^1\text{H}$  spectrum of E7, measured at  $70^\circ\text{C}$  under static conditions, without solvent. The spectrum was recorded at 300 MHz (UPB).

Peaks in the range of 6.8-8 ppm can be attributed to the aromatic rings of the liquid crystals. The aliphatic protons show chemical shifts at higher field in the range of 1-1.6 ppm. The CH<sub>2</sub> groups connected to the benzene rings appear at 2.6 ppm. The small peak with low intensity at around 3.8 ppm presents the CH<sub>2</sub>O group in 8OCB, which has a mass fraction of 16 % in E7.

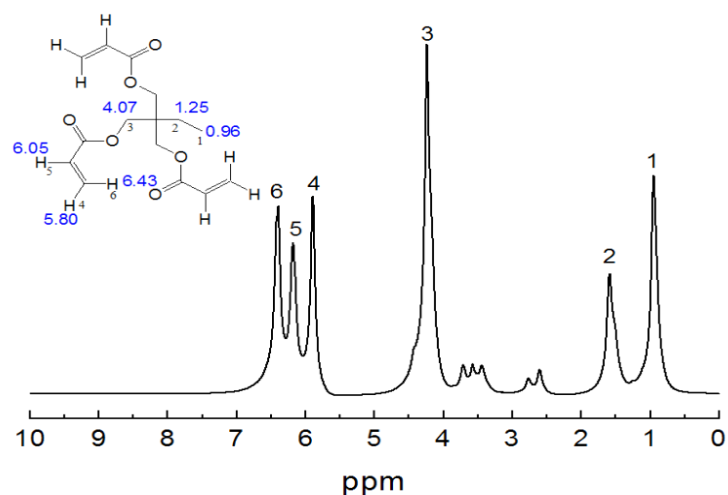


**Figure 4.2:** <sup>1</sup>H spectrum of TMPTA, measured at 25°C under static conditions, without solvent. The spectrum was recorded at 300 MHz (UPB). The atoms are labeled with numbers and chemical shift values calculated by ChemDraw.

TMPTA is an isotropic liquid at room temperature and its <sup>1</sup>H spectrum is presented in figure 4.2. The three peaks with high chemical shift values of 5.8-6.5 ppm correspond to the inequivalent protons attached to the carbon atoms of the C=C double bonds. The CH<sub>2</sub>O group appears at 4.2 ppm and has the largest intensity because 6 protons are contained in one molecule. The peak appearing at about 1 ppm comes from the protons of the CH<sub>3</sub> group and the one at 1.6 ppm from the CH<sub>2</sub> protons of the ethyl group. The small peaks around 2.5-3.8 ppm come from an impurity.

### Mixtures of E7 and TMPTA

Proton NMR spectra of some of the mixtures of E7 and TMPTA taken at 500 MHz with the high-resolution spectrometer are shown in figure 4.3. In the TMPTA/E7 system, E7 can be treated as a solvent for TMPTA. The property of solvent plays a

vital role for the chemical shift due to the interaction between solute and solvent.<sup>[91]</sup> These effects are due to hydrogen bonding, the anisotropy of the solvent molecules, polar effects, and van der Waals interactions.<sup>[92]</sup> Solvents with aromatic groups tend to produce high-field shifts in the solute due to the large diamagnetic anisotropy.<sup>[93]</sup> Indeed, it is observed that all peaks in the spectra shift to high field with increasing the mass fraction of E7, which is rich in  $\pi$  electrons in the aromatic rings of E7. With the addition of E7 to TMPTA, three large new peaks appear in the range from 7.0 to 8.0 ppm. These peaks correspond to the biphenyl fragments of the liquid crystal E7. In addition, a new peak is seen at 1.4 ppm corresponding to aliphatic protons in E7. On the other hand, the three peaks at  $\sim$ 5.8- 6.5 ppm belong to TMPTA and do not show any overlap with peaks of E7. From these resolved and separated peaks, we can easily obtain the diffusion constants for each component (cf. chapter 5).

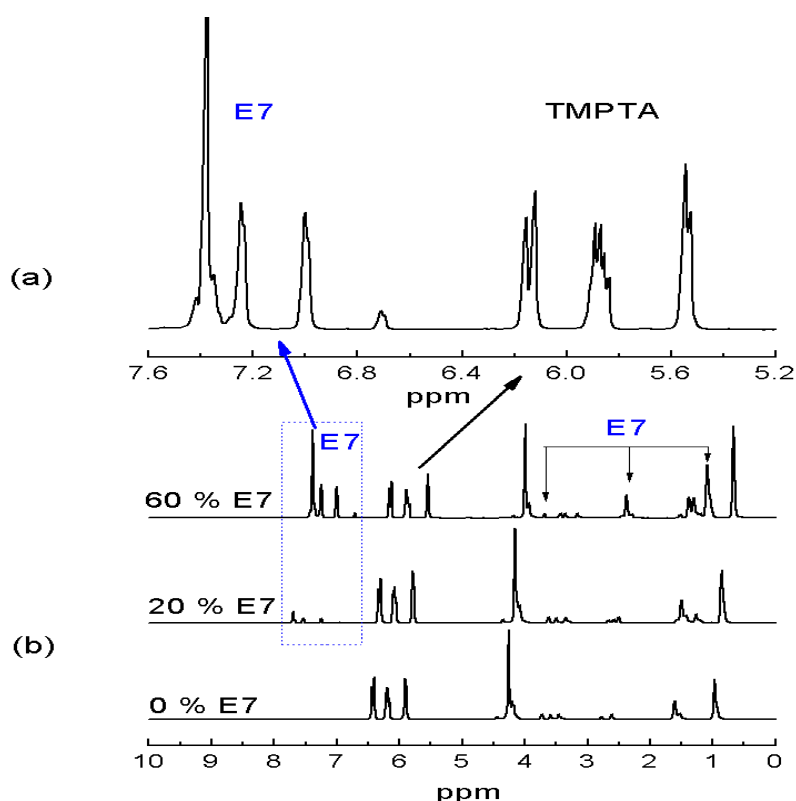


**Figure 4.3:** <sup>1</sup>H spectrum of TMPTA and its mixtures with E7, measured at 25°C under static conditions, without solvent. The spectrum was recorded at 500 MHz with a high-resolution NMR spectrometer (UPB). The spectrum of (a) is the enlargement of the spectral range of 5.2-7.6 ppm for the sample containing 60 % E7.



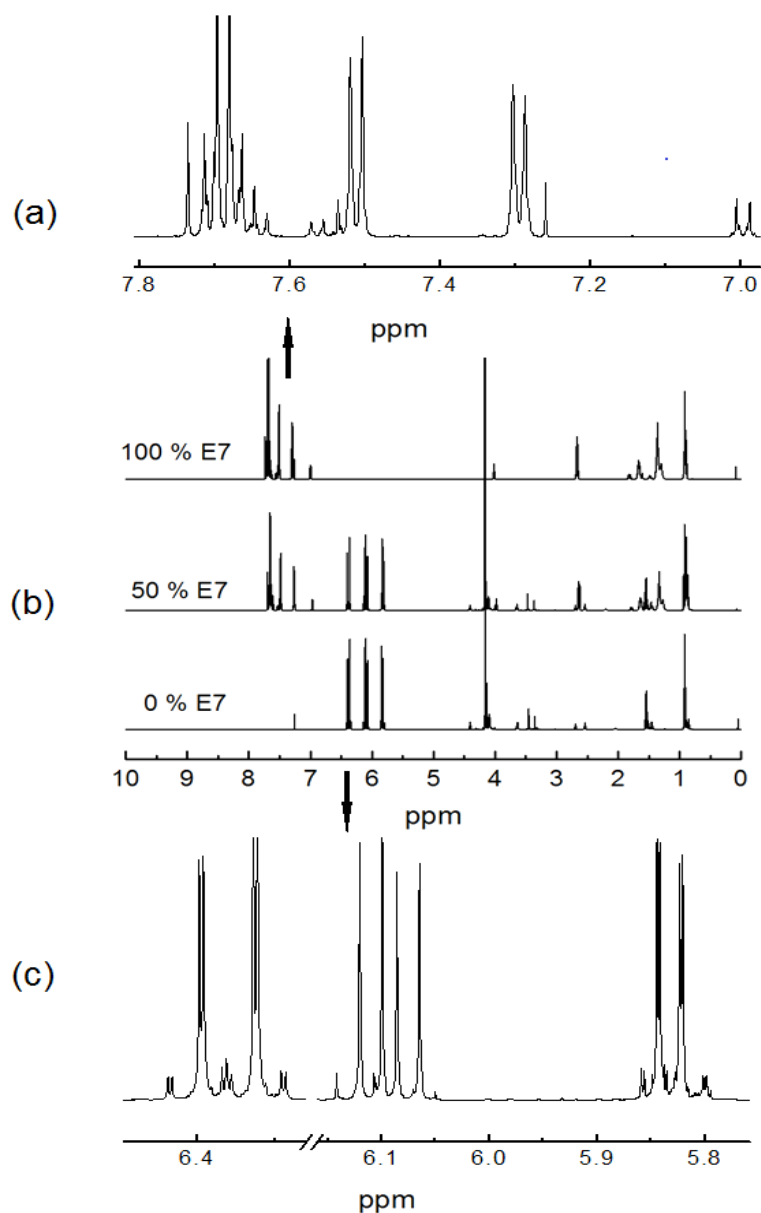


**Figure 4.4:** <sup>1</sup>H spectra of TMPTA, E7 and their mixture containing 50 % E7, measured at 25°C under static conditions, dissolved in CDCl<sub>3</sub>. The spectra were recorded at 500 MHz with a high-resolution NMR spectrometer (UPB) (b). Spectra of (a) and (c) are enlargements for the peaks at high ppm values for E7 and TMPTA, respectively.

For comparison with the spectra of the bulk samples, spectra in solution were also obtained. Figure 4.4 shows the spectra measured in CDCl<sub>3</sub>. They are much better resolved and the J couplings are much better recognized, compared with the spectra recorded without solvent (Fig. 4.3). Both the spectra measured with and without

solvent are consistent. In addition, in figure 4.4, all samples display the same solvent effect from  $\text{CDCl}_3$ ; no shifts depending on the molar ratio of E7 and TMPTA are observed here, in contrast to the spectra obtained without solvent shown in figure 4.3.

### 4.3.2 Determination of the nematic-to-isotropic phase transition from $^1\text{H}$ spectra

In figure 4.5 a proton spectrum of E7 in the nematic phase is shown on top. This spectrum shows the broad peaks characteristic of a liquid crystal with a dipolar splitting of  $\sim 30$  kHz. However, the spectra of a mixture of E7 and TMPTA (50 % E7) and of pure TMPTA show very sharp peaks in a small chemical shift range. Such narrow lines are characteristic of isotropic liquids. Adding TMPTA to the nematic phase of E7 reduces the nematic order and decreases the nematic-to-isotropic phase transition temperature  $T_{\text{NI}}$ . At room temperature the 50 % mixture is an isotropic homogeneous mixture. This is evident from the NMR spectrum. It is also confirmed by polarizing optical microscopy (cf. section 4.5).

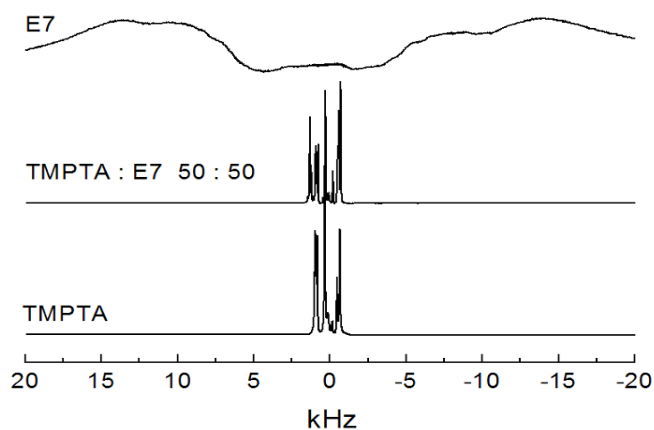


**Figure 4.5:** Proton NMR spectra of pure E7, TMPTA, and their mixture (50 % E7) measured under static conditions at room temperature. The spectra were recorded at 300 MHz (UPB).

Because of the large difference between the spectra in the nematic and in the isotropic phase, as described in Chapter 3 for the case of 5CB, NMR spectra can be used to determine the clearing point of liquid crystals. Here proton NMR is also used to

analyze the spectral splitting of E7 at different temperatures as shown in figure 4.6 and 4.7.

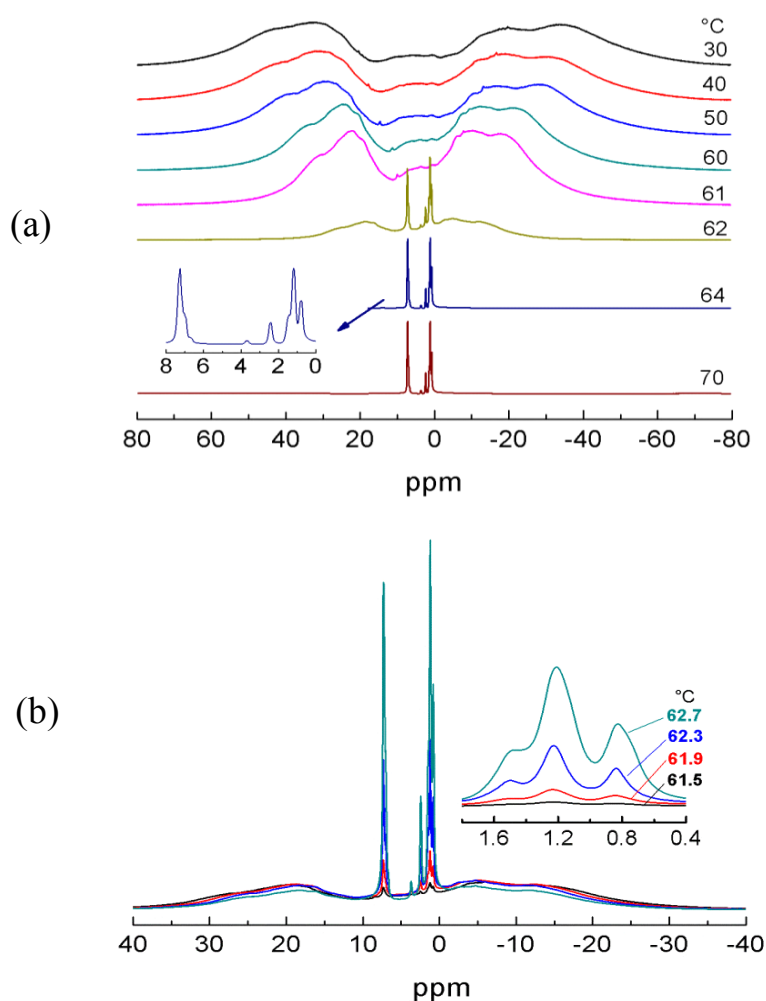


**Figure 4.6:** (a) Variation of the  $^1\text{H}$  spectra of E7 as temperature increases. The spectrum at the lower left corner is an enlargement of the one measured at 64  $^\circ\text{C}$ . The numbers marked on the right side indicate the temperatures which were applied to record the NMR spectra. The spectra were recorded at 300 MHz (UPB). (b)  $^1\text{H}$  spectra measured in the temperature range of the nematic to isotropic phase transition, in which two phases (nematic and isotropic) coexist.

In contrast to 5CB (cf. section 3.4), which shows a sharp transition, E7 shows a two-phase (nematic and isotropic) region between 61.5 and 63.7  $^\circ\text{C}$  (cf. Fig. 4.6). At around 61.5  $^\circ\text{C}$ , the isotropic sharp peaks appear in the range of 0-10 ppm, indicating the beginning of the nematic-to-isotropic phase transition. On further increasing the temperature, the sharp peaks increase in intensity. On the other hand, the broad peaks

decrease and the splitting becomes smaller. The broad peaks disappear at 63.7 °C and the central isotropic peaks reach a maximum. The finite width of the temperature range (~2.2 °C) for the phase transition is not surprising since E7 is a mixture of different liquid crystals. In addition,  $T_{NI}$  of E7 measured here is a little higher than 61 °C, the value given by Merck Company. As mentioned before, this is probably due to a temperature gradient between sample and temperature sensor. The results obtained here are in good agreement with the ones obtained from polarizing optical microscopy presented in section 4.5.

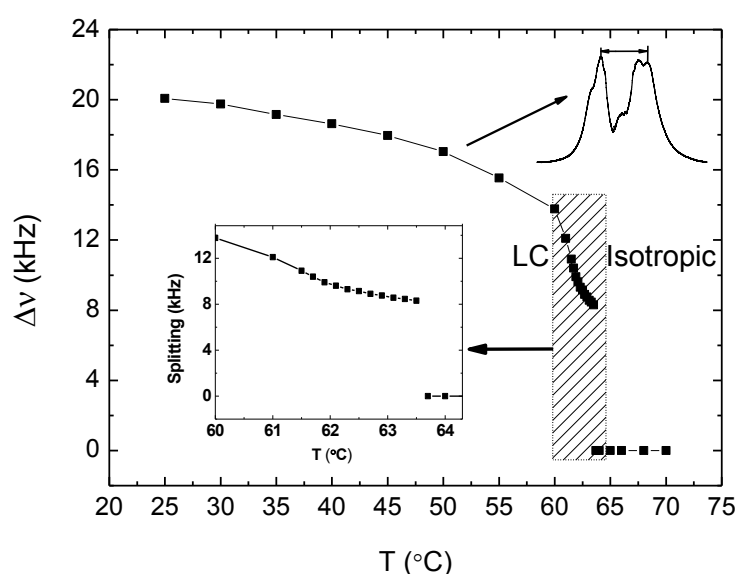


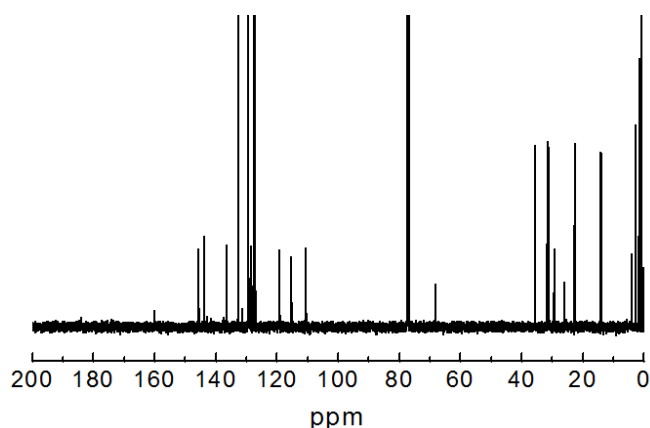
**Figure 4.7:** Proton spectra splitting of E7 as a function of temperature. The splitting is chosen as shown in the top-right corner. The hatched region is enlarged in the inset. N indicates the nematic phase and I the isotropic one.

A Haller plot of the temperature dependence of the spectral splitting shown in figure 4.7 yields the nematic order parameter (cf. Appendix A3). A reduction of the order parameter of E7 from ~0.7 to 0.425 in the temperature range from 25 °C to 61.5 °C is found. The nematic-to-isotropic phase transition of E7 is a first order transition (cf. Fig. 4.7), in good agreement with Maier-Saupe theory.

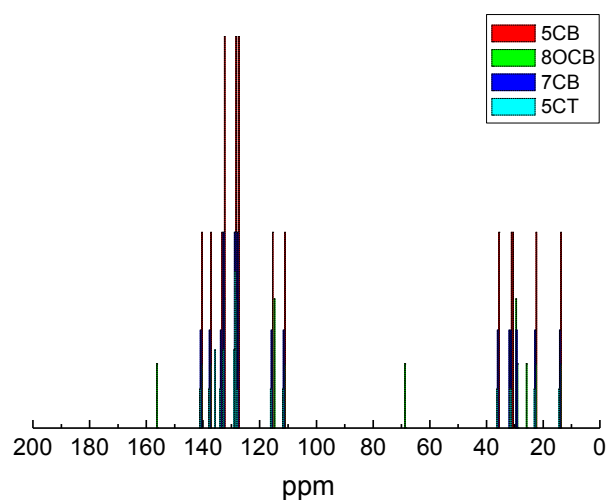
### 4.3.3 $^{13}\text{C}$ Spectra

Figure 4.8 shows the high resolution  $^{13}\text{C}$  spectrum of E7 in  $\text{CDCl}_3$  measured with the 500 MHz NMR spectrometer. The peaks above 100 ppm are due to the aromatic

carbons and the ones below 40 ppm belong to aliphatic carbons. The peak at around 68 ppm corresponds to the CH<sub>2</sub>O group in 8OCB. The single strong peak at 78 ppm comes from the solvent CDCl<sub>3</sub>. For comparison, a spectrum of E7 with chemical shifts predicted by ChemDraw is depicted in figure 4.9. The spectrum of E7 measured here is in good agreement with the one estimated by ChemDraw.



**Figure 4.8:** The <sup>13</sup>C spectrum of E7 dissolved in CDCl<sub>3</sub> recorded at 500 MHz (UPB). Large peaks are cut off in order to make smaller peaks visible. The peaks at around 0 ppm may come from impurities.



**Figure 4.9:** The ChemDraw prediction of the <sup>13</sup>C spectrum of E7. Peak intensities were calculated according to the composition of E7.

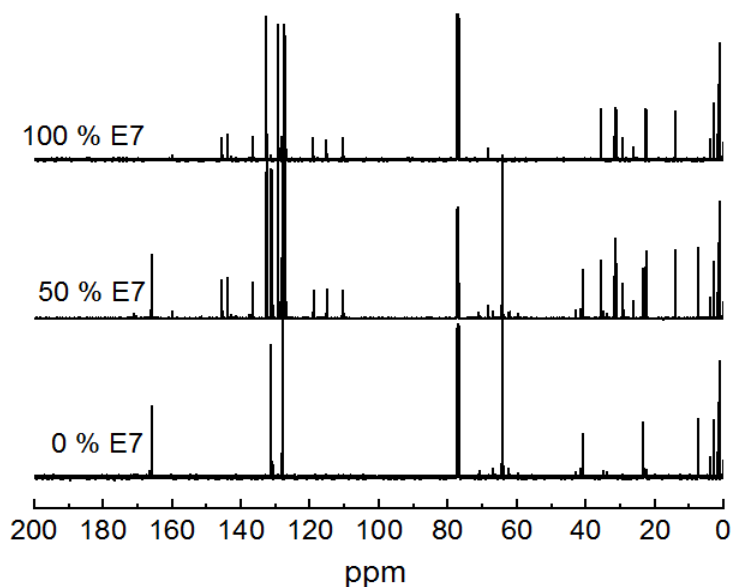


**Figure 4.10:**  $^{13}\text{C}$  spectra of TMPTA, E7 and their mixture containing 50 % E7, measured at 298 K, dissolved in  $\text{CDCl}_3$ . The spectra were recorded at 500 MHz NMR spectroscopy (UPB). The peaks at around 0 ppm may come from impurities.

In figure 4.10, spectra of TMPTA, E7, and a mixture of the two components are shown. The peak of  $\text{CDCl}_3$  appears at 78 ppm in all the spectra. Some peaks of TMPTA and E7 overlap in the mixture. The peak at 166 ppm in TMPTA is attributed to the carbonyl  $\text{C}=\text{O}$  and the one at 64 ppm to  $\text{CH}_2\text{O}$  of TMPTA.

#### 4.4 Spectra of the polymer PTMPTA and of PDLCs

##### 4.4.1 $^1\text{H}$ spectra

The polymer PTMPTA is solid-like and shows a typical quite broad spectrum due to the lack of reorientation of molecules. Figure 4.11 presents the spinning rate dependence of the  $^1\text{H}$  spectra of PTMPTA. As the spinning rate increases, the resolution become better and better. However, due to the strong proton dipolar interaction, poorly resolved spectra were obtained even when spinning the sample at 10 kHz.

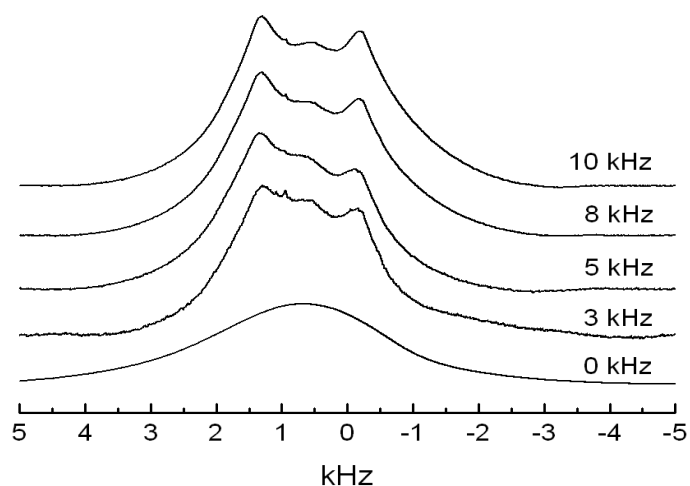


**Figure 4.11:**  $^1\text{H}$  NMR spectra of polymer PTMPTA as a function of spinning speed.

The spectra were obtained under MAS at 298 K.

A similar situation also applies to the PDLC system shown in figure 4.12. However, the PDLC sample shows additional relatively well resolved peaks. These sharp peaks come from the liquid crystal E7, but they are much less resolved compared with the ones of pure E7 in the nematic phase (cf. Chapter 5). In summary,  $^1\text{H}$  spectra of polymer/LC are poorly resolved even when spinning the samples at higher spinning rate under MAS. Therefore, the  $^1\text{H}$  spectra are of little use, whereas the  $^{13}\text{C}$  spectra will offer more useful information for the investigation of polymer/LC systems.

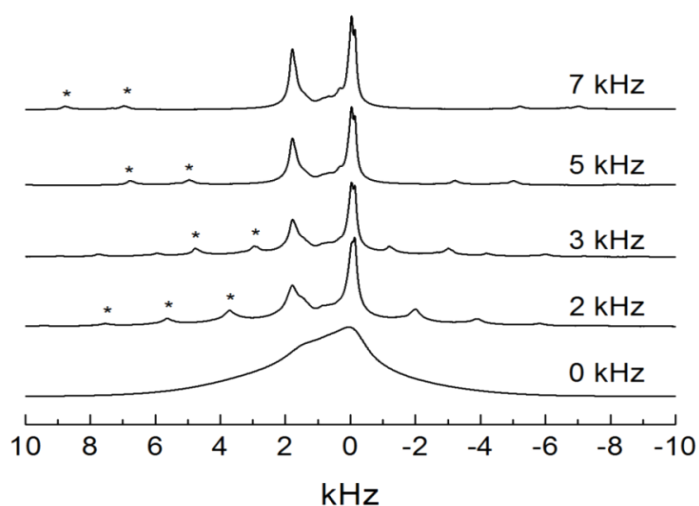


**Figure 4.12:**  $^1\text{H}$  NMR spectra of a PDLC sample as a function of spinning speed.

The spectra were obtained under MAS at 298 K.

#### 4.4.2 $^{13}\text{C}$ spectra

As discussed in the previous chapter, static measurements result in broad spectra with low signal-to-noise ratio (cf. spectrum of a PDLC sample labeled “0 kHz” in figure 4.13) even though 8192 scans were recorded. Spinning the sample at 5 kHz at the magic angle and cross polarization (bottom spectrum in Fig. 4.13) improve the spectral resolution and intensity, although only 2048 scans were recorded.

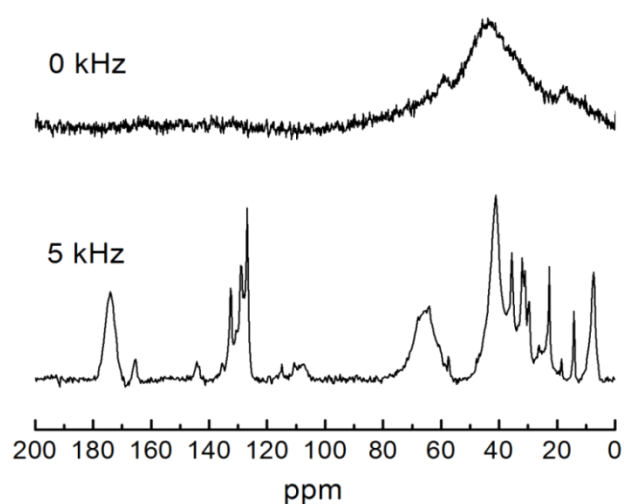


**Figure 4.13:**  $^{13}\text{C}$  NMR spectra of a PDLC sample (50 wt. % E7). The spectra were obtained at 298 K under static conditions (top) and under MAS (bottom).

Different spinning rates were used to identify any spinning side bands (SSB) and consequently correctly assign the signals to the different components. Figure 4.14 shows the  $^{13}\text{C}$  spectra of PTMPTA at different spinning rates under CPMAS. The peak at around 110 ppm is the SSB of the central peak of 176 ppm (C=O) separated by  $\omega=5$  kHz. At the higher spinning rate of 9 kHz, this SSB is farther away at around 58 ppm as marked in the spectrum. No additional change occurs, which indicates that only the C=O bond has spinning side bands because it has a large chemical shift anisotropy compared to other single bonds and is not mobile after polymerization.



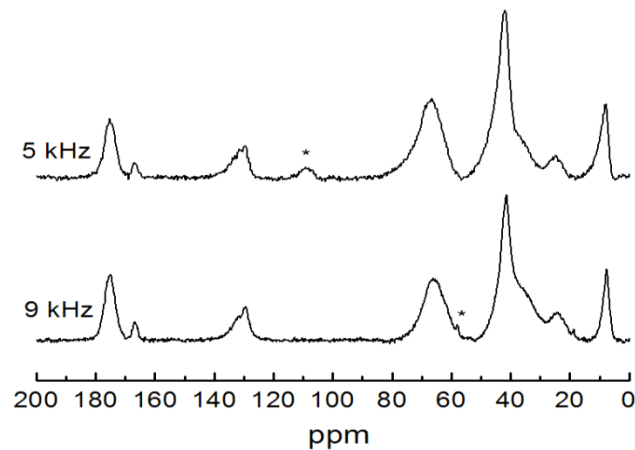


**Figure 4.14:**  $^{13}\text{C}$  NMR spectra of PTMPTA as a function of spinning rate. The spectra were obtained under CPMAS at 298 K.

The small sharp peak at 166 ppm from the C=O group of residual monomer originates from TMPTA still present in the polymer PTMPTA and from groups of the trifunctional monomer that have not reacted. So does the peak at 130 ppm corresponding to the C=C double bond.

Spectra of several PDLC samples with different E7 concentrations are presented in Figure 4.15. The higher the concentration of E7, the higher is the intensity of several sharp peaks which appear in the range of 110-140 and 18-35 ppm. Photographs of the different samples can be found in appendix A2.

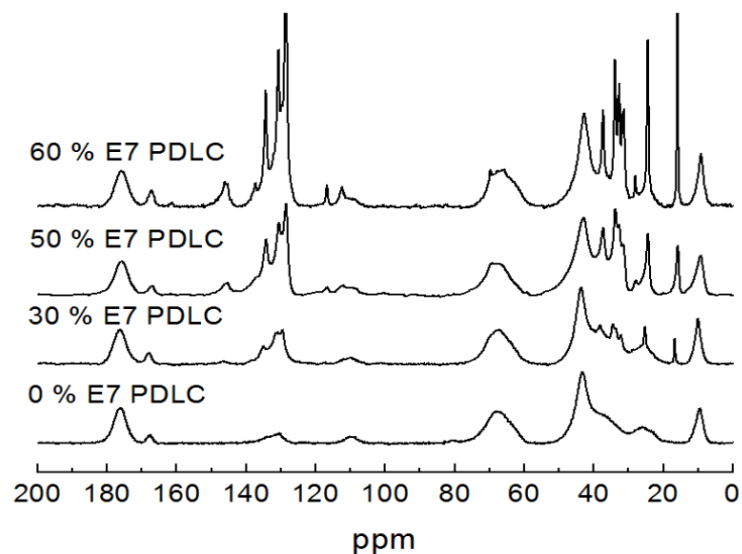


**Figure 4.15:**  $^{13}\text{C}$  NMR spectra of PDLCs as a function of mass fraction of E7. The spectra were obtained under CPMAS at 298 K,  $\omega=5$  kHz.

The success of the polymerization reaction is verified by the  $^{13}\text{C}$  spectra shown in figure 4.16. All spectra were measured under CPMAS at 5 kHz, except the one of the liquid TMPTA, which was recorded under static conditions without CPMAS. The peaks around 166 ppm can be assigned to the carbonyl group of TMPTA. The peaks of  $\text{C}=\text{O}$  shift to higher ppm values for PTMPTA and PDLCs. This is due to the change of the neighboring  $\text{C}=\text{C}$  group into a carbon single bond by the polymerization. The  $\text{C}=\text{C}$  peaks at about 130 ppm are reduced profoundly in intensity and the intensity of the peak at 40 ppm is increased when going from TMPTA to PTMPTA. This proves that the polymerization is successful. However, the remaining peaks at 166 and 130 ppm indicate that the three  $\text{C}=\text{C}$  bonds in TMPTA cannot react completely due to the steric hindrance. In the PDLC spectrum, the peaks at 176, 65, 42 and 9 ppm are from the polymer PTMPTA, while the peaks at 110-145 and 23-36 ppm are superpositions of PTMPTA and E7 signals. Only the peak at 14 ppm completely originates from E7. The peaks of PTMPTA have a much larger linewidth than that of pure TMPTA because pure TMPTA is a liquid.

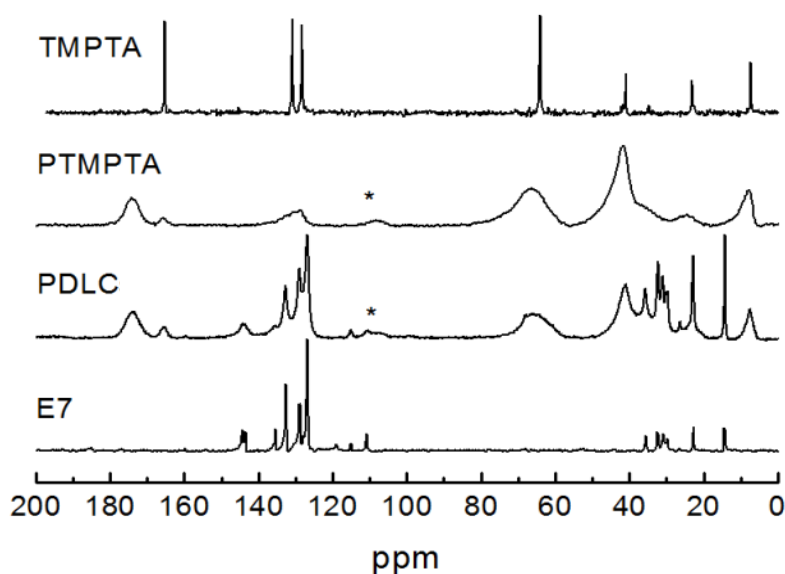


**Figure 4.16:** Comparison of  $^{13}\text{C}$  NMR spectra of TMPTA, PTMPTA, PDLC (50 wt. % E7) and pure E7. The spectra were obtained under CPMAS at 298 K, except the one of TMPTA, which was obtained under static conditions using direct  $^{13}\text{C}$  excitation.

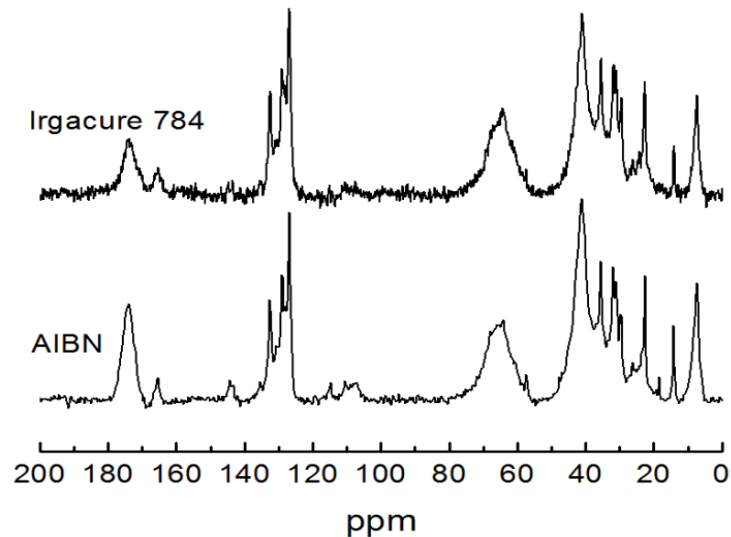


**Figure 4.17:**  $^{13}\text{C}$  NMR spectra of PDLCs prepared using different initiators. The spectra were obtained under CPMAS at 298 k,  $\omega=5$  kHz.

In order to check the effect of initiator on the preparation of PDLCs, azobisisobutyronitrile (AIBN) was chosen for comparison with Irgacure 784. The spectra of PDLCs made with different initiators are shown in figure 4.17. Based on the spectra, both initiators play the same role in the polymerization.

#### 4.5 Textures of TMPTA/E7 by polarizing optical microscopy

Polarizing optical microscopy is a direct way to study the textures of liquid crystals. It gives us a direct impression of the microstructure of the samples. Another application is that the phase of the liquid crystals can be deduced from the texture. In particular phase transitions, for example, from a smectic to a nematic phase or from a nematic to an isotropic phase, can be determined. Here, polarizing optical microscopy was applied to confirm the nematic-to-isotropic phase transition of pure E7 and the destabilization of the nematic phase in TMPTA/E7 mixtures observed by NMR spectroscopy, as discussed in section 4.3.2.

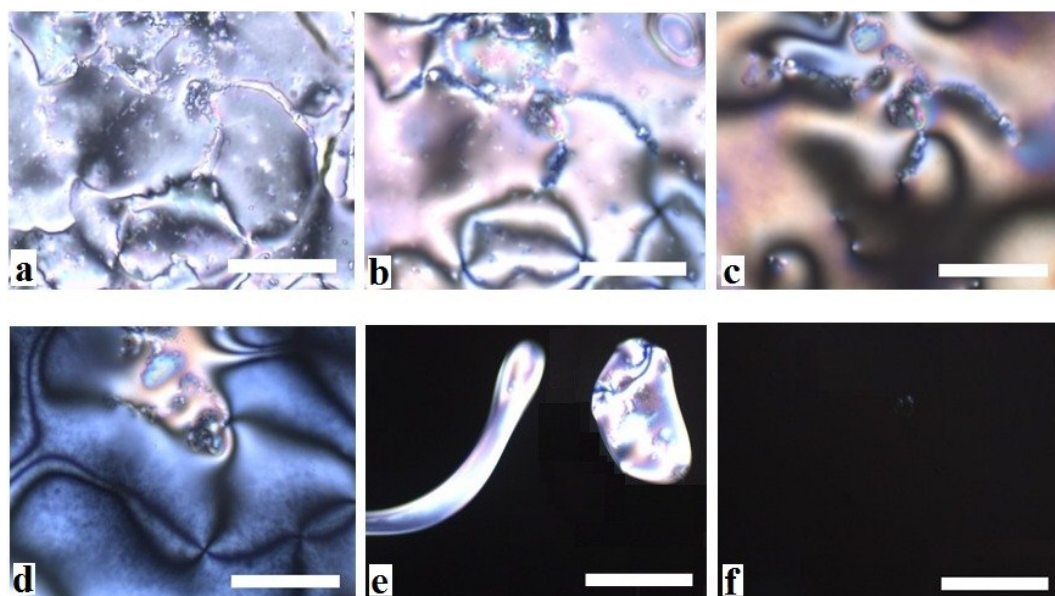
##### 4.5.1 Microscopy measurements

A series of homogenous mixtures of E7 and TMPTA was investigated. A drop of the sample was placed on a microscope slide, and a cover slide was employed to cover the sample such that a thin film of the mixture could be investigated. Liquid  $\text{N}_2$  was used

to cool the mixtures into the nematic phase. The textures and the nematic-to-isotropic transition temperatures  $T_{NI}$  were recorded while heating the samples at a rate of 1.0 K/minute. At the transition point, the temperature was held constant for an additional 3 minutes to make sure that the transition is complete.

#### 4.5.2 Textures and phase behavior of TMPTA/E7

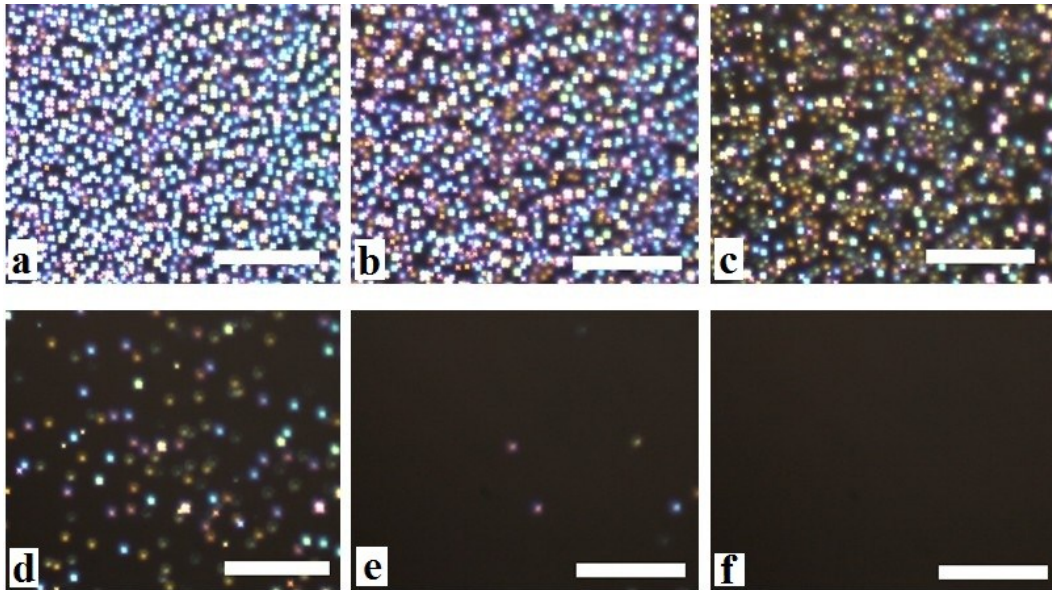
The textures of pure E7 are shown in figure 4.18. No big change occurs during heating the sample from 50 to 58 °C. At 59 °C it begins to change color. At 60 °C, the transition of E7 from nematic to isotropic started. Around 61 °C, most liquid crystal textures have disappeared. Therefore for the pure liquid crystal E7 the nematic-to-isotropic phase transition is at 61 °C, which is the same as the transition temperature given by Merck Company. The measurement for pure E7 confirms that the temperatures measured by NMR are about 2 K too high.



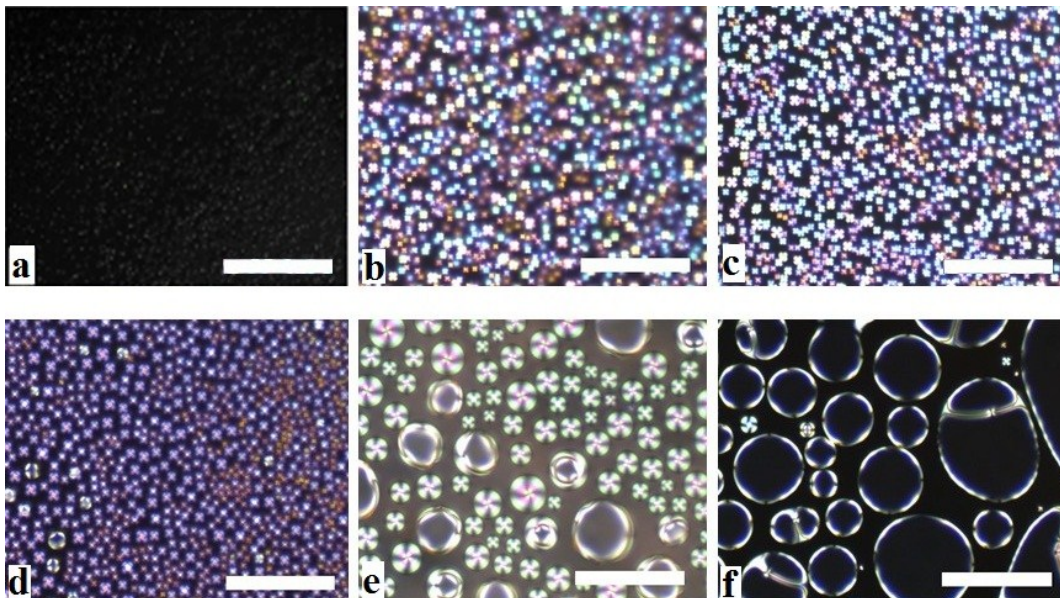
**Figure 4.18:** Textures of pure E7. Temperatures from a to f are 50, 59, 59.5, 60, 61 and 61.5 °C, respectively. The scale bar corresponds to 50  $\mu m$ .

Figure 4.19 shows an example for the microscopy measurements of the mixtures. One finds that the nematic-to-isotropic transition temperature for the mixture containing 50 wt. % E7 is around 8-9 °C, which confirms the observations by proton NMR spectra on the pure E7 and the mixture TMPTA/E7. It can be seen from figure 4.19 that, below

8 °C not only the nematic phase is present but both nematic and isotropic phases coexist.



**Figure 4.19:** Textures of a mixture containing 50 % E7. Temperatures from a to f are -3, 0, 3, 6, 8 and 9 °C, respectively. The scale bar corresponds to 50  $\mu\text{m}$ .



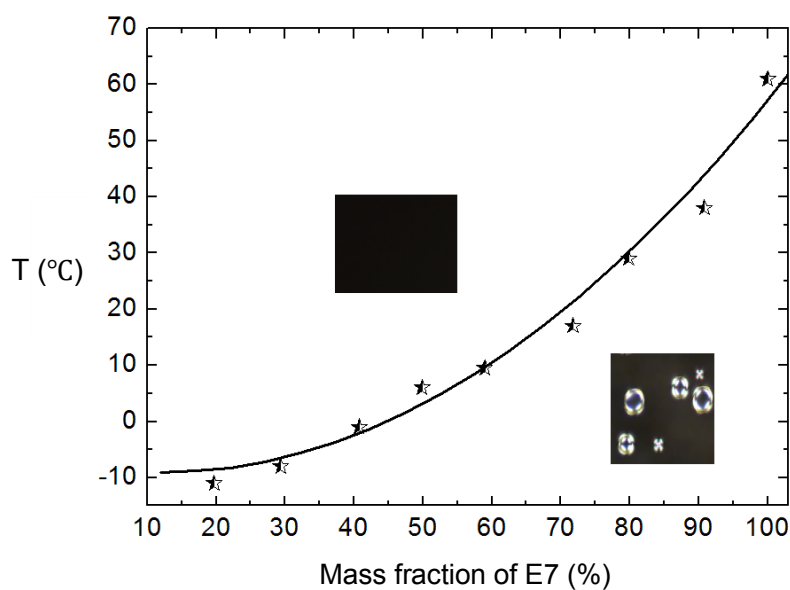
**Figure 4.20:** Textures of different mixtures at 0 °C. The mass fraction of E7 from a to f are of 40, 50, 60, 70, 80 and 90 %, respectively. The scale bar corresponds to 50  $\mu\text{m}$ .

Figure 4.20 shows the textures for mixtures with different concentrations of E7. The



droplets of the liquid crystal E7 increase in size with increasing concentration of E7. In fact, the mixtures with less than 70 % of E7 are transparent, while those containing more than 70 % E7 appear turbid in observations with the naked eye at room temperature.

The influence of TMPTA on the nematic-to-isotropic phase transition temperature has been verified by polarizing microscopy. Figure 4.21 shows the nematic-to-isotropic phase transition temperatures for several mixtures. These values are in good agreement with the values reported for a similar system containing mixtures of 2-ethylhexylacrylate and E7.<sup>[94]</sup> Obviously, mixtures containing up to 70 % E7 are isotropic at room temperature. These findings support the results of the NMR measurements.



**Figure 4.21:** Nematic-to-isotropic transition temperatures of the mixtures. The star-shaped symbols represent the transition temperatures measured by polarizing optical microscopy, while the line serves as a guide to the eye.

#### 4.6 Conclusions

$^1\text{H}$  and  $^{13}\text{C}$  NMR spectra of the pure components, of TMPTA/E7 mixtures, of the pure polymer and of PDLCs have been analyzed and peaks have been assigned to the different species. The temperature dependence of the  $^1\text{H}$  spectra of E7 shows that E7

starts to become isotropic at 61.5 °C, but the nematic broad spectra disappear completely only at 63.7 °C. Thus, E7 shows a finite transition range, in which narrow isotropic peaks and broad nematic peaks coexist. NMR also indicates that adding TMPTA to E7 lowers the nematic-to-isotropic phase transition temperature. This is confirmed by polarizing optical microscopy, which shows the nematic phase at lower temperatures in the mixtures of TMPTA/E7. Mixtures containing less than 70 % E7 are isotropic (transparent to the naked eye) at room temperature.

## **Chapter 5 Self-Diffusion in the PDLC Systems TMPTA/E7 and Their Precursor Mixture**

Holographic polymer-dispersed liquid crystals (HPDLCs), particular polymer-dispersed liquid crystals with periodic pattern, become more and more useful in many optic-electronic fields due to their unique properties. The diffusion coefficients of the liquid crystals and of the photo-reactive monomer are essential parameters for the speed of formation, the resulting morphology and the final diffraction efficiency of the structure of HPDLCs. TMPTA/E7-based HPDLCs have been investigated by Andreas Redler, who used a reaction-diffusion model to simulate the formation of the holographic grating generated by illuminating the precursor mixture with lasers.<sup>[95]</sup> The lack of experimental values of the diffusion coefficients motivated us to measure the diffusion constants by NMR. The measurements were performed at Lund University in cooperation with Daniel Topgaard.

Besides, diffusion coefficients provide us a way to probe the structure and dynamics at a molecular level. The information includes the size and shape of the molecules. There are several advantages of using NMR to measure diffusion constants, such as fast measurement with high sensitivity. One unique advantage of NMR diffusometry is that diffusion coefficients of different species in one mixture can be measured. This chapter will first focus on the principle of NMR diffusometry. It follows closely the treatment of the topic given by Maki and Loening.<sup>[96]</sup> Second, NMR diffusometry is applied to measure the self-diffusion coefficients of E7 and TMPTA in mixtures of the two components, and the variation as a function of E7 concentration is investigated. In addition, self-diffusion measurements are carried out for polymer/LC systems under MAS to investigate the mobility and structure of the LC dispersed in the polymer matrix.

### **5.1 Diffusion**

Diffusion measured by NMR attracted more and more attention in the last years.



Examples for previous diffusion studies in our group include the PhD thesis by Felix Kleinschmidt, who studied diffusion in anisotropic media such as lyotropic liquid crystals and polymer hydrogels,<sup>[97]</sup> and the investigation of dye aggregation carried out by Richard Szopko.<sup>[98]</sup> More information and details about the diffusion investigation on liquid crystals by NMR can be found in the review written by Dvinskikh.<sup>[99]</sup>

The random motion of particles above 0 K can be described as diffusion. It includes translational, rotational, and spin diffusion from an NMR point of view. Figure 5.1 demonstrates two kinds of basic diffusion: translational diffusion and rotational diffusion. Translational diffusion results from the kinetic energy and the interactions with other particles or molecules. Rotational diffusion, that is the reorientation of a molecule, arises due to kinetic energy. Spin diffusion is the random movement of spin polarization through dipolar couplings. This thesis is focusing on translational diffusion measured by NMR.

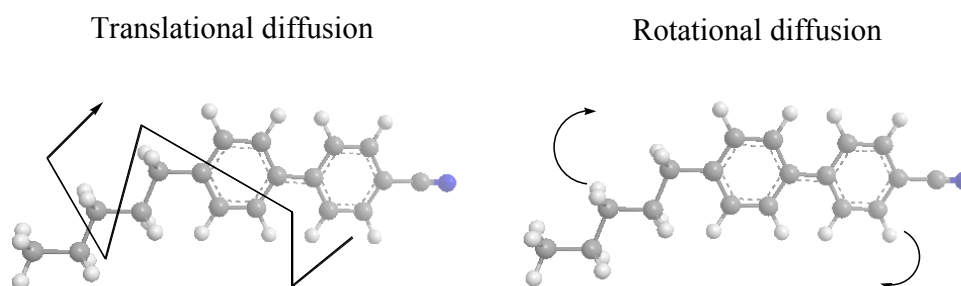


**Figure 5.1:** Schematic of diffusion for 5CB. Left: Translational diffusion; right: rotational diffusion.

In fact, the individual molecules can move even when they are bonded to other molecules by intermolecular force. This happens easily for the molecules in a gas or in liquid sample, but even for the molecules in a solid sample when given sufficient time. The rate of molecular movement is determined by the shape and size of molecules. It also depends on the solvent and the temperature. The average rate of the movement of the molecules is described by the diffusion coefficient  $D$ . The displacement  $Z$  of a moving molecule in time  $t$  is Gaussian distributed:

$$P(Z) = \frac{1}{\sqrt{4\pi Dt}} \exp\left(-\frac{Z^2}{4Dt}\right) \quad (5.1)$$

The mean-square displacement for one-dimensional diffusion is

$$\overline{Z^2} = \int_{-\infty}^{\infty} Z^2 P(Z) dZ = 2Dt$$

and the root-mean-square (rms) displacement for a molecule is

$$Z_{rms} = \sqrt{\overline{Z^2}} = \sqrt{2Dt} \quad (5.2)$$

In three dimensions, the root-mean-square displacement for a molecule is

$$R_{rms} = \sqrt{\overline{R^2}} = \sqrt{6Dt}$$

Combining the kinetic energy and the friction of solvent leads to the famous Stokes-Einstein equation:

$$D = \frac{k_B T}{f} = \frac{k_B T}{6\pi\eta R_h} \quad (5.3)$$

Here  $f$  is a proportionality constant known as the friction coefficient,  $k_B$  is the Boltzmann constant and  $T$  is the temperature,  $\eta$  is the viscosity of the solvent and  $R_h$  is the hydrodynamic radius of the diffusing molecule.

## 5.2 NMR diffusometry

The general NMR methods for measuring diffusion coefficients can be found in references.<sup>[61, 64]</sup> A spatially-dependent magnetic field, in addition to the local magnetic field  $B_0$ , is needed for diffusometry by NMR. The spatially-dependent field is called gradient field. It is generated by using gradient coils. The sum of the local magnetic field and the gradient field will produce different Larmor frequencies for molecules at different positions in space. Additionally, an echo experiment (cf. Chapter 2) is required for the measurement of diffusion by NMR.

### 5.2.1 The pulsed gradient spin echo (PGSE)

The simplest way for measuring diffusion goes back to Stejskal and Tanner<sup>[60, 100]</sup> who were the first to modify the Hahn echo experiment, using a pulsed gradient. Figure 5.2 shows the PGSE pulse sequence for the diffusion experiment. It contains an echo and two gradient pulses inserted in the evolution delays before and after the refocusing pulse.

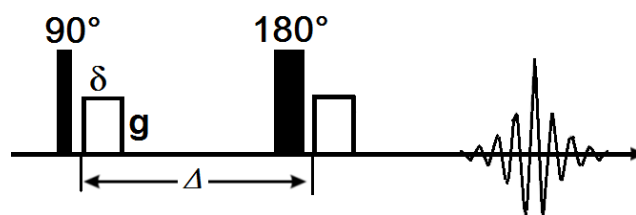


**Figure 5.2:** Schematic of PGSE pulse sequence which contains an echo rf pulse sequence and two gradient pulses with magnitude  $g$ , duration  $\delta$  and separation  $\Delta$ .

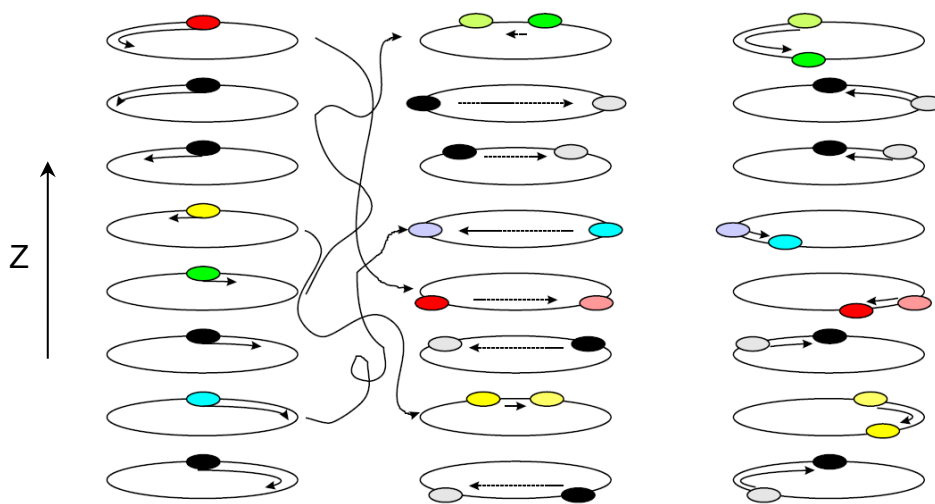


**Figure 5.3:** Phase evolution during gradients and echo formation.<sup>[97]</sup> The first column corresponds to the first gradient pulse (cf. Fig. 5.2), the second to phase shifts by the  $180^\circ$  pulse and the third to the refocussing gradient pulse. Black molecules do not change their  $z$ -axis position and colored molecules change their  $z$ -position.

Figure 5.3 shows phase evolution according to the gradients and echo formation during the PGSE pulse sequence of figure 5.2. During the first gradient the magnetization dephases and a magnetization helix along the  $z$ -axis is built up. The magnetization refocuses during the second gradient and an echo is formed. To completely refocus the magnetization, the molecules of the sample must not move during the time period in between the gradients (black). On the opposite, the moved molecules (colored) will not be able to restore the transverse magnetization to their initial phase completely (Fig. 5.3, right column) due to the changed Larmor frequency. Therefore, an attenuated signal will be observed due to incomplete refocusing.

### 5.2.2 Stimulated echo

The traditional spin echo uses a  $180^\circ$  pulse to refocus transverse magnetization. Diffusion can be measured only under the time limitation of the transverse relaxation  $T_2$ . In practice, however, some systems, such as liquid crystals, have a relatively small  $T_2$ , which is insufficient for the diffusion measurement. In the stimulated echo (STE) the  $180^\circ$  pulse is replaced by two  $90^\circ$  pulses. After the first of those pulses longitudinal magnetization exists and the larger longitudinal relaxation time  $T_1$  is the limiting time constant for the diffusion measurement (Fig. 5.4a).

Since the phases of the transverse magnetization vectors are averaged over all spins in the sample the echo is not phase shifted but attenuated. The degree to which diffusion attenuates the signal can be calculated based on a modified version of the Bloch equations (which are a set of differential equations that provide a semi-classical description of the NMR experiment). The result of this derivation is that the attenuation of the signal ( $M$ ) relative to the signal in the absence of diffusion ( $M_0$ ) is given by<sup>[101]</sup>

$$M = M_0 \exp(-bD) \quad (5.4)$$

where  $D$  denotes the diffusion coefficient, and  $b = \gamma^2 A_g^2 t_d$ . Here,  $\gamma$  is the gyromagnetic ratio,  $t_d$  is the effective diffusion time, and  $A_g$  is the area of the gradient pulse or pulse pair.  $A_g = g\delta$  for rectangular gradients as in figure 5.4a and for the sequence with a pair of ramped gradients shown in figure 5.4b, whereas  $A_g = 2g\delta/\pi$  for the sequence with a pair of sine-shaped gradients of length  $\delta/2$  as shown in figure 5.4c.<sup>[102]</sup>  $t_d$  is approximately equal to  $\Delta$ , except for a small correction that depends on the details of the pulse sequence. The diffusion during the period  $\Delta$  is determined by a series of measurements with increasing gradient strengths. The details are described in appendix A6.

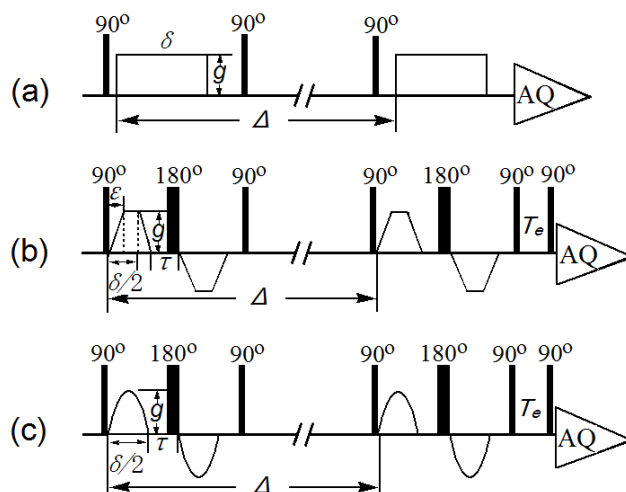


**Figure 5.4:** PFG-STE pulse sequence for diffusion experiments. The standard PFG stimulated-echo (a), the ramped (b) and the sine-shaped BPP-LED (bipolar pair pulse longitudinal eddy-current delay) (c) diffusion sequence. In (b) and (c) the encoding gradients of the stimulated-echo are applied as symmetrical bipolar pulse pairs and the LED part of the sequence is an extension with an eddy current delay period  $T_e$ . The program code is shown in appendix A7.

## 5.3 Experimental aspects

### 5.3.1 Sample preparation

Precursor mixtures containing the monomer TMPTA and the liquid crystal E7 were mixed at different concentrations of up to 60 wt. % E7. All the mixtures were ultrasonically treated for 10 minutes at room temperature to obtain a homogeneous solution. For the polymer samples, please refer to section 4.2.

### 5.3.2 NMR measurements

All NMR experiments presented in this chapter were carried out at Lund University, using a Bruker Avance 500 spectrometer.  $^1\text{H}$  spectra of isotropic liquids, that is, of TMPTA and its mixtures with E7, were measured at 500 MHz using Bruker standard pulse sequences under static conditions. The spectra of the nematic pure E7 and of the polymer systems were measured under magic-angle spinning (MAS) at 5 kHz. The NMR chemical shift values are given in ppm relative to TMS measured in pure TMPTA.

The diffusion measurements were carried out at a temperature of 298 K with pulsed-field-gradient stimulated-echo (PFG-STE) pulse sequences. For the experiments under static conditions and under MAS, different probes and pulse sequences were used. For proton spectra and diffusion experiments under static conditions a DIFF-25 diffusion probe was used. The gradient strength varied between 1 % and 100 % of its maximum value 3.0 T/m. A high-resolution 4-mm-MAS-probe with pulsed field gradient capabilities was employed to measure spectra and diffusion under MAS. The MAS frequency was set to 5 kHz and the maximum gradient was calibrated to 0.59 T/m for the MAS probe with variation of the gradient strength in the linear range between 10 % and 90 % of a set maximum value. Further details are given in appendix A6.

The static spectrum of the liquid crystal is very broad due to the anisotropic dipolar coupling in the liquid crystalline phase as discussed in Chapter 4. A combination of MAS with pulsed field gradients was used in the measurement of the diffusion coefficient of the pure liquid crystal.<sup>[103-105]</sup> MAS has two advantages. First, the increased resolution on the ppm scale permits one to observe separately each individual group with identical electronic surroundings. Second, the enhanced transverse relaxation time under MAS conditions allows for a sufficient time for the implementation of the used magnetic field gradients.<sup>[106]</sup>

Since the samples studied here have short transverse relaxation times,  $T_2$ , of the order of only tens of milliseconds, the pulsed-field-gradient stimulated-echo (PFG-STE) method<sup>[107]</sup> was used to determine the diffusion coefficients. Using this pulse sequence (Fig. 5.4) the magnetization is stored along the z-axis and decays with the time constant  $T_1$  of longitudinal relaxation, which is of the order of hundreds of milliseconds (see section 6.2), providing sufficient time for diffusion.

For the static experiments the pulse sequence shown in figure 5.4b was used. The total duration of each gradient pulse was  $(\delta/2)+\varepsilon=1.4$  ms with up- and down-ramps of  $\varepsilon=0.4$  ms. The windows between the  $90^\circ$  and  $180^\circ$  pulses were 2.1 ms. The second and fourth  $90^\circ$  pulses are followed by spoiler gradients of 2.1 ms (not shown). The eddy

current delay  $T_e$  was 22.4 ms. For each gradient step 8 scans were accumulated, using a recycle delay of 1 s. The diffusion measurements under MAS were performed using the pulse sequence of figure 5.4c with the following parameters:  $g$  from 0.0531 – 0.4779 T/m,  $\delta = 5$  ms,  $\tau = 1$  ms,  $T_e = 10$  ms. The spoiler gradients had a duration of 1 ms. The number of scans was 8, and the recycle delay was 3 s. For both static and MAS experiments the effective diffusion time  $t_d$  was about 100 ms. Further details can be found in appendix A6 and reference.<sup>[108]</sup>

## 5.4 Results and discussion

### 5.4.1 Proton spectra

The NMR instrument used here is optimized for diffusion measurements but not for spectral resolution. The proton spectra obtained with the same spectrometer as used for diffusometry are presented in this section.  $^1\text{H}$  spectra of high resolution were shown in Chapter 4.

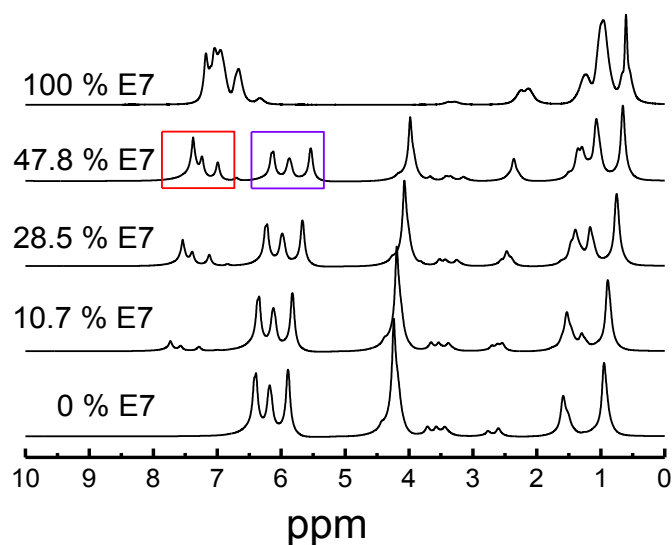


**Figure 5.5:** Proton spectra of mixtures of TMPTA and E7 and of the pure components measured under static conditions, except for the 100 % E7 sample, which was measured under MAS at 5 kHz (Lund).

Since the addition of TMPTA to E7 decreases the nematic-to-isotropic transition temperature  $T_{\text{NI}}$ , the mixtures are isotropic at room temperature (see Chapter 4). Figure 5.5 shows the resolved spectra in static measurements without MAS, whereas the

spectrum of pure E7 was measured under MAS at 5 kHz. Peak assignments were given in Chapter 4. The spectra shown here are less resolved compared to the high-resolution spectra presented in Chapter 4. However, the spectra here are sufficiently resolved to measure diffusion of the components. The diffusion coefficients can be obtained by analyzing the groups of peaks in the range from 7.3-8.0 ppm (E7) and from 5.5-6.8 ppm (TMPTA).

Figure 5.6 shows the spectra of E7, TMPTA, PTMPTA, (P)TMPTA and a PDLC sample with 50 wt. % E7 for comparison. Except for the spectrum of the liquid TMPTA, those spectra were obtained under MAS. (P)TMPTA refers to a sample measured as obtained after polymerization, whereas PTMPTA is a polymer sample after extraction of residual monomers and oligomers with  $\text{CH}_2\text{Cl}_2$ .

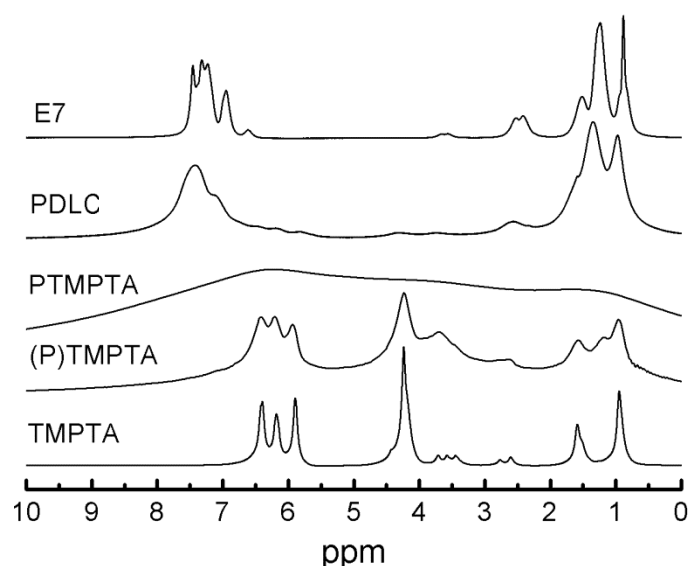


**Figure 5.6:** Proton NMR spectra of E7, TMPTA, PTMPTA (purified polymer), (P)TMPTA (polymer with residual monomer) and a PDLC sample obtained from a 50 % mixture. The spectra of E7, PDLC and the polymers were obtained under MAS at 5 kHz. The spectrum of TMPTA was measured under static conditions.

The spectrum of the monomer TMPTA in the bottom of figure 5.6 shows very sharp peaks even without MAS. The peaks around 5.8-6.6 ppm represent the protons attached to the carbon atoms of the double bonds. Its polymer, denoted as PTMPTA,



shows one very broad signal even under MAS due to the immobile polymer backbone. In the case of (P)TMPTA, the additional peak at 1.2 ppm means that the polymerization was partly successful. However, most peaks, for example, the peaks at 5.8-6.6 ppm are still fairly narrow. This demonstrates that the polymerization was not complete, and quite a lot of monomer remained in the polymer matrix after polymerization.

The spectrum of the PDLC sample is very similar to that of E7 but several weak additional peaks in the ranges of 5.8-6.6 ppm and 3.5-4.5 ppm can be assigned to the monomer. The peaks in PDLC are less resolved and broader compared to that of pure E7 due to the boundary to the polymer network. Compared to the spectrum of (P)TMPTA, the monomer peaks have surprisingly low intensity in the PDLC sample, considering that the sample contains 50 wt. % polymer. Apparently, the polymerization reaction of the TMPTA/E7 is more complete than that of pure TMPTA.

#### **5.4.2 Diffusion in isotropic mixtures**

Taking the TMPTA/E7 mixture containing 47.8 % E7 as an example, the procedure of obtaining the diffusion coefficients of the two components is illustrated. Figure 5.7 shows spectra obtained using the PFG-STE pulse sequence, where the gradient amplitude  $g$  is varied. Each peak can be analyzed according to equation 5.4. Here, the peak amplitudes at 7.3 and 5.4 ppm are used to obtain the diffusion coefficients of E7 and TMPTA, respectively. The full spectra are shown in appendix A4. The fitting according to eq. 5.4 shown in the bottom of figure 5.7 results in diffusion coefficients of  $1.5 \times 10^{-11} \text{ m}^2 \text{ s}^{-1}$  and  $9.4 \times 10^{-12} \text{ m}^2 \text{ s}^{-1}$  for E7 and the monomer TMPTA, respectively. The slight deviation from a straight line observed for E7 is probably due to the fact that E7 is a mixture of different molecules.

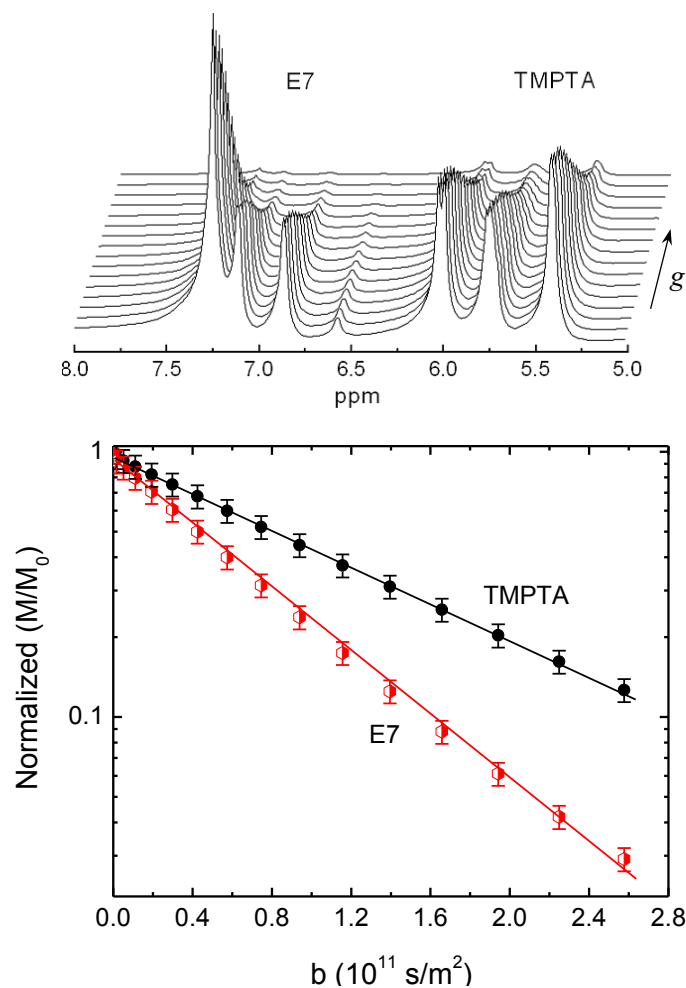


**Figure 5.7:** Top: Spectra as a function of gradient amplitude  $g$ ; bottom: Semi-logarithmic plot of the relative NMR signal intensity  $M/M_0$  versus  $b = (\gamma g \delta)^2 t_d$ , where  $\gamma$  is the gyromagnetic ratio of  $^1\text{H}$ ,  $g$  the variable gradient strength,  $\delta$  the gradient width, and  $t_d$  the effective diffusion time. From the signal decay curves diffusion coefficients are obtained. The error bar is 5 % of the data.

To determine the diffusion trends with increasing ratio of TMPTA/E7, diffusion was measured for a series of mixtures. Figure 5.8 shows that the diffusion coefficients of both E7 and TMPTA increase with increasing mass fraction of E7. The diffusion coefficient of E7 is always higher than that of TMPTA in the same mixture. Between an E7 content of 10 and 60 %, the diffusion coefficients of E7 and TMPTA increase by factors of 143 % and 120 %, respectively. TMPTA has a larger hydrodynamic radius and higher viscosity compared to the smaller rod-like molecules of E7. Therefore, as the concentration of E7 increases, the viscosity of the mixture decreases. The

dependence of the diffusion coefficients on the composition of the mixtures reflects the change of viscosity and is in good agreement with equation 5.3. The fact that E7 has a higher diffusion coefficient is also consistent with eq. 5.3. However, the  $D$  value of pure E7 (100 %) seems a little higher than predicted by the diffusion trends in Figure 5.8. This is not surprising. First, a model for the variation of diffusion with composition is not easily obtained, since it contains many factors, such as viscosities, free volume, phase structure and so on. Second, the diffusion of pure E7 was obtained in a different way, namely, under MAS and not under static conditions as the other values. Viel found that the high spinning rate under MAS produces a deviation of the measured diffusion coefficient from its intrinsic  $D$  value obtained under static conditions.<sup>[104]</sup> The diffusion constant measured under MAS for E7 may be higher than the real diffusion coefficient.

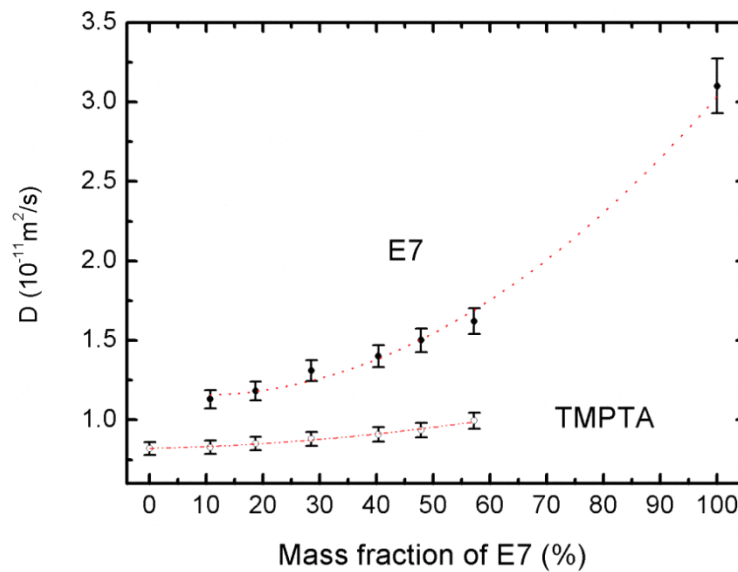


**Figure 5.8:** Diffusion coefficients of TMPTA and E7 as a function of composition.

The  $D$  value for pure E7 (100 %) was obtained by measuring under MAS, while all other values were measured under static conditions. The error bar is 5 % of the data.

The numerical  $D$  values are reported in appendix A6.1.3.

The measured diffusion coefficient of TMPTA was used in Redler's simulations of the temporal evolution of the diffraction efficiency during the preparation of an HPDLC sample.<sup>[108]</sup> Good agreement between the simulation and experimental results was

found. As can be seen in figure 5.8, the diffusion coefficients of TMPTA are slightly lower than  $10^{-11} \text{ m}^2 \text{ s}^{-1}$ . Hence, our values measured for TMPTA are almost three orders of magnitude larger than the reported value of  $1.89 \times 10^{-14} \text{ m}^2 \text{ s}^{-1}$ , which was obtained by an analysis of the initial change of the first-order diffraction efficiency measured during the grating formation in a system similar to the one investigated here.<sup>[109]</sup> Although the precursor mixture used in that work was a different one, its viscosity can be expected to be similar to the one of our mixture. Therefore, a TMPTA diffusion coefficient of the order of  $10^{-14} \text{ m}^2 \text{ s}^{-1}$  appears much too low. The poor estimate is possibly due to large uncertainties in the analysis of the onset of grating formation.

### 5.4.3 Diffusion in PDLCs

Diffusion measurements were also carried out for E7 in the nematic phase as discussed in the previous section already, for the polymer sample labeled (P)TMPTA, which contains residual monomer, and for a PDLC sample made from a 50 % mixture. Due to the broad NMR signals of liquid crystals and polymers, these experiments had to be carried out under MAS. Details of the diffusion coefficient analysis can be found in appendix A5 and A6.2.

Figure 5.9 presents the signal decay curves due to diffusion for these samples. For comparison the curves for the components TMPTA and E7 in the 50 % precursor mixture are also shown. Two different gradient strengths offer different range of  $b$ . TMPTA and E7 in the 50 % mixture were measured under static conditions and the rest were obtained under MAS at 5 kHz. The diffusion constants obtained from these decay curves are listed in Table 5.1, Table A6.1.3 and Table A6.2.3. The fastest diffusion is found in pure E7 due to its large mobility (low viscosity) and rod-like molecular shape. The diffusion coefficient obtained for pure E7 is  $D=3.10 \times 10^{-11} \text{ m}^2 \text{ s}^{-1}$ . This is in good agreement with values reported in the literature as being in the range of  $2.8\text{-}8.0 \times 10^{-11} \text{ m}^2 \text{ s}^{-1}$  for 5CB,<sup>[99]</sup> which is one of the E7 components. E7 in the mixture of TMPTA/E7 moves more slowly due to the more viscous environment. The diffusion constant of E7 in the PDLC sample is between the ones for bulk E7 and E7 in the

TMPTA/E7 mixture. This will be discussed later.

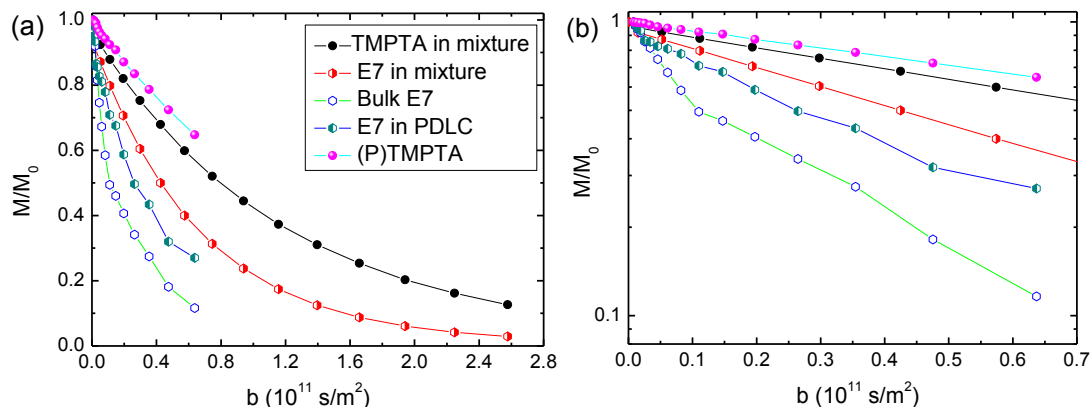


**Figure 5.9:** The attenuation of intensity as a function of pulsed field strength. The larger slope corresponds to larger diffusion coefficients. (b) the enlargement of (a) in the range of  $b$  between 0 and  $0.7 \times 10^{11} \text{ s/m}^2$ .

According to figure 5.9, the smallest mobility is found in the polymer. The diffusion coefficient measured as  $0.68 \times 10^{-11} \text{ m}^2 \text{ s}^{-1}$  in (P)TMPTA actually represents the diffusion of residual monomer (and perhaps small oligomers) in the polymer matrix. The  $D$  value is smaller than that of the pure monomer TMPTA measured under static conditions, which can be deduced from the diffusion curve in figure 5.9 as  $0.87 \times 10^{-11} \text{ m}^2 \text{ s}^{-1}$ . This reduction of the  $D$  value is attributed to the hindrance by the polymer matrix and/or branches. The diffusion coefficient of pure polymer cannot be measured because there is no resolved polymer peak in the spectrum. But one can easily predict that the diffusion coefficient of pure polymer is very small or equal to zero and therefore not accessible by NMR. For the same reason, the diffusion measurement for PDLC is expected to mainly reveal the diffusion process of the liquid crystal molecules. Obviously, the crosslinked polymer should not diffuse on the time scale of the measurement.

In the PDLC containing 50 % E7, a diffusion coefficient of  $2.09 \times 10^{-11} \text{ m}^2 \text{ s}^{-1}$  is obtained. This is about 2/3 of the value of pure E7 ( $3.10 \times 10^{-11} \text{ m}^2 \text{ s}^{-1}$ ). One may conclude that the diffusion of the liquid crystal is slowed down in the droplets perhaps

due to the influence of the polymer interface or that the molecules begin to “feel” the restriction due to the polymer matrix. The polymer surface induces a slowing-down of molecular translational diffusion at the interface.<sup>[106, 110-113]</sup> Romanova found that  $D$  reduces by a factor of about 1.5 or less from bulk liquid crystal to a confined system.<sup>[106]</sup> Vilfan pointed out the reduction of diffusion coefficients of 5CB from bulk to confined systems is strongly determined by the structure and size of the pores.<sup>[41]</sup> E7 has a reduction in diffusion rate from bulk LC to PDLC droplets with a diameter of  $\sim 1$   $\mu\text{m}$  depending on the diffusion time  $t_d$ .<sup>[110]</sup>

**Table 5.1:** Diffusion constants obtained by MAS for the liquid crystal E7, for a sample of the polymer ((P)TMPTA), and for E7 in a PDLC sample.

Sample	D(E7)/ $10^{-11} \text{ m}^2 \text{ s}^{-1}$	D(TMPTA)/ $10^{-11} \text{ m}^2 \text{ s}^{-1}$
E7	3.10	-----
(P)TMPTA	-----	0.68
PDLC	2.09	-----
E7:TMPTA (50:50)	1.56	0.96 (cf. page 58 and 99)

One can estimate if the droplet size can affect the measured diffusion constant. The distance or walking length can be calculated from the diffusion constant of bulk E7 and the effective diffusion time. The three-dimensional displacement during a diffusion time of  $t_d=96.2$  ms is  $\sqrt{\langle r^2 \rangle} = \sqrt{6Dt_d} = 4.2$   $\mu\text{m}$ . On the other hand, the diameter of the liquid crystal droplets is about 1.0-1.6  $\mu\text{m}$  according to polarizing optical microscopy measurements. Therefore, one can expect that the E7 molecules really feel the hindrance by the boundary to the polymer phase and a reduced apparent  $D$  value is measured for the PDLC.

When comparing E7 in the monomer mixture and in the PDLC, both at 50 % E7, it seems paradoxical that E7 in the polymer matrix ( $2.09 \times 10^{-11} \text{ m}^2 \text{ s}^{-1}$ ) diffuses faster than in the mixture with the TMPTA monomer ( $1.50 \times 10^{-11} \text{ m}^2 \text{ s}^{-1}$ ). From the monomer

mixture point of view, the solution is homogenous and each E7 molecule can feel the high viscosity of the mixture. On the other hand, this does not happen in the case of PDLCs due to the phase separation. In this case, the E7 molecules are in a less viscous environment.

## **5.5 Conclusions**

Diffusion results indicate that both TMPTA and E7 diffuse faster when the weight fraction of E7 increases. In each mixture, TMPTA diffuses more slowly than E7 due to the larger hydrodynamic radius of TMPTA. Diffusion in the PDLC system shows that the interface of polymer and E7 restricts the diffusion of the liquid crystal molecules, resulting in a reduced apparent diffusion coefficient compared to bulk E7.

## Chapter 6 Relaxation Study of PDLC Systems PTMPTA/E7 and Their Precursor Mixture

This chapter will focus on the relaxation in the different samples and an attempt will be made to obtain information on how the different environments of a molecular species influence its mobility. The temperature dependence of the proton spin-lattice relaxation times ( $T_1$ ) will be shown for the samples with resolved spectra, such as E7, TMPTA and their mixtures. For comparison with polymer and PDLC sample, which have broad proton spectra and do not yield site-specific relaxation rates, spin-lattice relaxation times in the rotating frame ( $T_{1\rho}$ ) obtained by cross polarization measurements will be discussed. In the beginning of this chapter (sections 6.1 and 6.2), the principal relationship between spin relaxation rates and correlation times of molecular motions as well as the experimental procedure of measuring  $T_{1\rho}$  will be discussed. Section 6.3 concentrates on the results and discussion of the relaxation data, including spin-lattice relaxation studies on pure E7 and its mixtures with TMPTA (6.3.1), carbon spin-lattice relaxation times in the rotating frame ( $T_{1\rho,C}$ ) (6.3.2), and proton relaxation times in the rotating frame ( $T_{1\rho,H}$ ) (6.3.3). Section 6.4 will summarize the conclusions obtained from the relaxation experiments.

### 6.1 Correlation function, spectral density and relaxation rates

Relaxation in NMR<sup>[63, 70]</sup> can be used to probe motions of molecules, ranging from molecular rotation and self-diffusion to internal motion in non-rigid molecules. The relationship between spin relaxation and molecular motion can be described by the semi-classical Bloembergen, Purcell and Pound (BPP) model.<sup>[114]</sup> In the BPP model, relaxation times are related to a correlation time,  $\tau_c$ , which is the characteristic time between significant fluctuations in the local magnetic field experienced by a spin due to molecular motions or reorientations of a molecule or segment of a molecule. In this part, the origin of the relationship between different types of spin relaxation times ( $T_1$ ,  $T_2$  and  $T_{1\rho}$ ) and the correlation time  $\tau_c$  is described.



Molecular motion leads to time-dependent spin interactions such as dipolar-dipolar couplings or anisotropic chemical shifts. They cause randomly fluctuating local magnetic fields which can induce transitions of the spins enabling them to relax. The field fluctuations can be described by an autocorrelation function  $g(t)$ . For thermal motion of molecules, such as Brownian motion,  $g(t) = e^{-t/\tau_c}$  in the simplest case. The function  $g(t)$  reflects the degree to which the molecule reorients in a given time interval. Fourier transforming the correlation function yields the spectral density function  $J(\omega) = 2 \int_0^\infty g(t)e^{-i\omega t} dt$ , which describes the distribution of the frequencies  $\omega$  of the motion and is relevant for NMR relaxation.<sup>[63, 115]</sup>

$$J(\omega) = \frac{C'\tau_c}{1+\omega^2\tau_c^2} \quad (6.1)$$

The constant  $\tau_c$  is the correlation time.  $\tau_c$  corresponds to the time during which the molecules rotate by one radian;  $C'$  is a constant and  $C'=1/5$ .<sup>[66]</sup>

In case of the spin-lattice ( $T_1$ ) and spin-spin ( $T_2$ ) relaxation for protons and carbons, the inverse relaxation time or relaxation rate (denoted by  $R$ ) can be written as the expressions given below containing spectral density functions.<sup>[66, 70]</sup>

The contribution of proton-carbon dipolar coupling to the spin-lattice relaxation is given by:

$$R_{1,H}(H, C) = \frac{1}{T_{1,H}} = \frac{C\gamma_H^2\gamma_C^2}{r_{HC}^6} [J(\omega_H - \omega_C) + 3J(\omega_H) + 6J(\omega_H + \omega_C)] \quad (6.2)$$

$$R_{1,C}(H, C) = \frac{1}{T_{1,C}} = \frac{C\gamma_H^2\gamma_C^2}{r_{HC}^6} [J(\omega_H - \omega_C) + 3J(\omega_C) + 6J(\omega_H + \omega_C)] \quad (6.3)$$

For proton  $T_1$  relaxation caused by homonuclear dipolar couplings one obtains

$$R_{1,H}(H, H) = \frac{1}{T_{1,H}} = \frac{3C\gamma_H^4}{r_{HH}^6} [J(\omega_H) + 4J(2\omega_H)] \quad (6.4)$$

Spin-spin relaxation caused by proton-carbon dipolar coupling is described by:

$$R_{2,H}(H, C) = \frac{1}{T_{2,H}} = \frac{C\gamma_H^2\gamma_C^2}{2r_{HC}^6} [4J(0) + J(\omega_H - \omega_C) + 3J(\omega_H) + 6J(\omega_C) + 6J(\omega_H + \omega_C)] \quad (6.5)$$

$$R_{2,C}(H, C) = \frac{1}{T_{2,C}} = \frac{C\gamma_H^2\gamma_C^2}{2r_{HC}^6} [4J(0) + J(\omega_H - \omega_C) + 3J(\omega_C) + 6J(\omega_H) + 6J(\omega_H + \omega_C)] \quad (6.6)$$

and  $T_2$  caused by homonuclear proton-proton dipolar is given by:

$$R_{2,H}(H, H) = \frac{1}{T_{2,H}} = \frac{3C\gamma_H^4}{2r_{HH}^6} [3J(0) + 5J(\omega_H) + 2J(2\omega_H)] \quad (6.7)$$

In the equations above  $C = \frac{1}{10} \left(\frac{\mu_0 \hbar}{4\pi}\right)^2$ ,  $\omega_H$  and  $\omega_C$  are the Larmor frequencies in the local magnetic field  $B_0$  of proton and carbon, respectively;  $r_{HC}$  and  $r_{HH}$  are the distances between proton-carbon and proton-proton, respectively. Both equations 6.4 and 6.7 are true for relaxation by carbon-carbon dipolar coupling as well, but the corresponding parameters  $r_{CC}$ ,  $\gamma_C$  and  $\omega_C$  of carbon must be used.

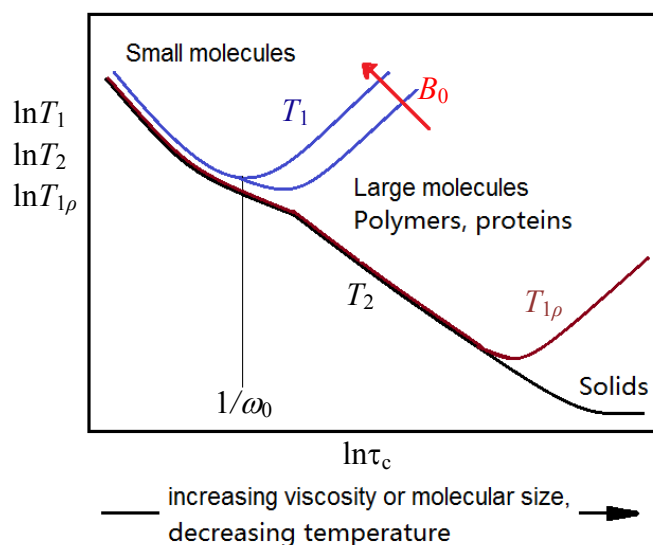


**Figure 6.1** : NMR relaxation times as a function of correlation time  $\tau_c$ . The spin-lattice relaxation time  $T_1$  reaches the minimum value at  $\tau_c \approx 1/\omega_0$ , where  $\omega_0$  is the Larmor frequency. In the case of  $T_{1\rho}$ ,<sup>[116]</sup> the minimum occurs at  $\tau_c \approx 1/\omega_1$  with nutation frequency  $\omega_1$ .

For a weakly interacting spin 1/2 pair, the spin–lattice relaxation rate in the rotating frame is given by:<sup>[66, 116, 117]</sup>

$$\frac{1}{T_{1\rho}} = \frac{3C\gamma^4}{2r^6} [3J(2\omega_1) + 5J(\omega_0) + 2J(2\omega_0)] \quad (6.8)$$

where  $\omega_0$  is the Larmor frequency in the local magnetic field  $B_0$ ,  $\omega_0 = \omega_H$  and  $\omega_0 = \omega_C$  for proton and carbon respectively;  $\omega_1 = \gamma B_1$  with  $B_1$  the amplitude of the field induced by the radiofrequency in the rotating frame,  $r$  is the distance between the nuclear spin pair.  $T_{1\rho}$  depends on the angular frequencies  $\omega_1$  and  $\omega_0$ . If the experiment is carried out in a constant external magnetic field, i.e., in our case of  $\omega_0 = 2\pi \times 300$  MHz for protons, the last two terms of eq. (6.8) are constant, and the expression can be simplified to

$$\frac{1}{T_{1\rho}} = \frac{9c\gamma^4}{2r^6} [J(2\omega_1) + K] \quad (6.9)$$

where  $K=(5/3)J(\omega_0)+(2/3)J(2\omega_0)$  is a constant depending on the molecular motions that are effective for the involved spectral densities at the Larmor frequency  $\omega_0$  and  $2\omega_0$ .

$T_{1\rho}$  is kind of the same as  $T_2$  except in cases, in which chemical exchange or/and anisotropy are involved.<sup>[118]</sup>  $T_2$  decreases with increasing viscosity or molecular size in the full range of temperatures. Both  $T_1$  and  $T_{1\rho}$  have minimum values at the correlation times of  $\tau_c=1/\omega_0$  or  $\tau_c=1/\omega_1$ . Large (that is, slowly moving) molecules or groups reach the minimum value at higher temperature. Combining all those consideration yields a schematic plot of relaxation times as function of correlation time  $\tau_c$  as shown in figure 6.1.

## 6.2 Determination of spin-lattice relaxation in the rotating frame, $T_{1\rho}$

In this section, the experimental techniques for measuring spin-lattice relaxation times in the rotating frame of carbons ( $T_{1\rho,C}$ ) and protons ( $T_{1\rho,H}$ ) are described. Figure 6.2 shows the pulse sequences. As shown in the left in figure 6.2, in the cross polarization measurement, fixing the CP time, varying the spin lock time  $\tau$  of carbon after magnetization transfer from protons to carbons, and fitting the signal decay as a function of  $\tau$  gives  $T_{1\rho,C}$ . The right part of figure 6.2 shows the pulse sequence for determining  $T_{1\rho,H}$  for protons.

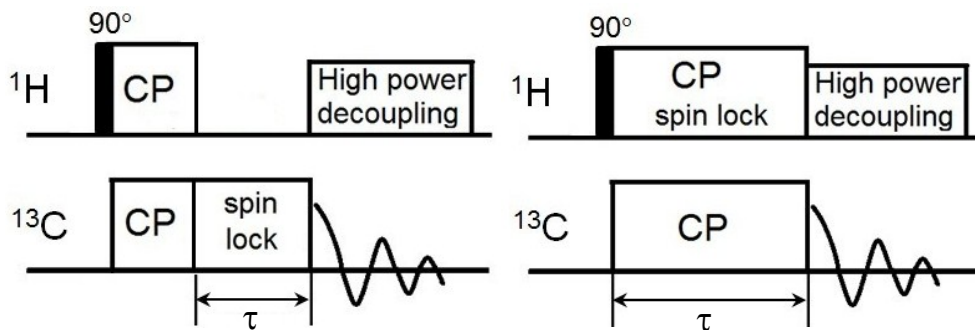


**Figure 6.2:** The pulse sequences for measurement of the spin-lattice relaxation time in the rotating frame  $T_{1\rho}$  under CP. Left:  $T_{1\rho,C}$  experiment by varying the spin lock time  $\tau$  after CP. Right:  $T_{1\rho,H}$  measurement by varying the CP contact time  $\tau$ .

$T_{1\rho,C}$  can be calculated by equation (2.3) repeated here:

$$M(t) = M_{\infty} + (M_0 - M_{\infty}) \exp\left(\frac{-t}{T_{1\rho,C}}\right)$$

where  $M_{\infty}$  is the final value of intensity,  $M_0$  is the initial intensity.  $T_{1\rho,C}$  depends on the spin lock power, which is proportional to  $\omega_1$  (cf. eq. 6.9).

During the cross polarization period, both proton and carbon magnetization eventually decay since relaxation is effective during the whole pulse sequence. However, the magnetization for carbons increases initially due to magnetization transfer at the beginning of the CP contact. As a result the full curve of carbon magnetization as a function of time shows a maximum. With the pulse sequence in the right part in figure 6.2, both relaxation times of protons and carbons can be obtained:<sup>[82, 119, 120]</sup>

$$M(t) = M_0 \lambda^{-1} \left[ 1 - \exp\left(\frac{-\lambda t}{T_{CH}}\right) \right] \left[ \exp\left(-\frac{t}{T_{1\rho,H}}\right) - \exp\left(-\frac{t}{T_{CH}} - \frac{t}{T_{1\rho,C}}\right) \right] \quad (6.10)$$

Where  $\lambda = 1 + \frac{T_{CH}}{T_{1\rho,C}} - \frac{T_{CH}}{T_{1\rho,H}}$

If  $T_{CH} \ll T_{1\rho,C}$ , then equation (6.10) can be simplified as:

$$M(t) = M_0 \lambda^{-1} \left[ 1 - \exp\left(\frac{-\lambda t}{T_{CH}}\right) \right] \exp\left(-\frac{t}{T_{1\rho,H}}\right) \quad (6.11)$$

Here,  $T_{CH}$  is the cross polarization time constant, characteristic of the rate of magnetization build-up between protons and carbons;  $T_{1\rho,H}$  is the relaxation time for protons and  $T_{1\rho,C}$  for carbons.

In fact, equation (6.10) is only applicable for systems with very fast spin diffusion among protons. For some systems with a slow spin diffusion rate or an “isolated H-C pair”, the magnetization oscillates between the abundant and dilute nuclei. The oscillation of magnetization between carbon and proton is observed in liquid crystals E7 in this PhD work. In this case, the above equation is modified and the following equation is obtained:<sup>[121-126]</sup>

$$M(t) = M_0 \exp\left(-\frac{t}{T_{1\rho,H}}\right) \left[ 1 - \frac{1}{2} \exp\left(-\frac{t}{T_{df}}\right) - \frac{1}{2} \exp\left(-\frac{3t}{2T_{df}}\right) \cos\left(\frac{dt}{2}\right) \right] \quad (6.12)$$

Here  $T_{df}$  is the spin diffusion constant of protons and  $d$  is a factor determined by the orientation of the molecules with respect to the local magnetic field  $B_0$ .

## 6.3 Results and discussions

### 6.3.1 Proton spin-lattice relaxation, $T_{1,H}$

#### Spinning rate dependence

In order to study the effect of the spinning rate on the proton relaxation of molecules, figure 6.3 presents the relaxation times of E7 for several central lines, which were measured for a series of spinning rates. Already at small spinning rates a well resolved proton spectrum is observed, as shown in figure 5.6. It is found for both aromatic (1) and aliphatic protons (2 and 3) that the longitudinal magnetization relaxes faster when the spinning rate is increased. A profound influence of the spinning rate on the relaxation times was also reported by Gil and Albertir.<sup>[127]</sup> They found that the  $^1\text{H}$  relaxation times in a system of low mobility, such as glycine, decrease with increasing spin rate. On the other hand, a system with high mobility, such as adamantane, shows an increase in  $T_1$  at higher spinning rate. These effects are explained by a weakening of the spin diffusion efficiency with increasing spinning rate.

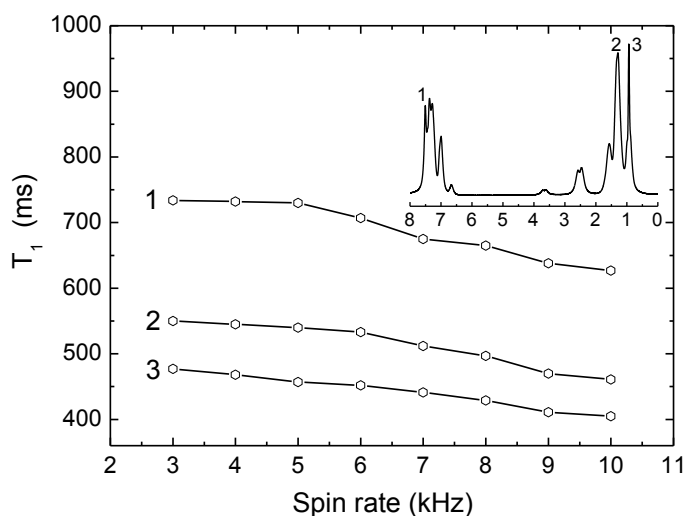


**Figure 6.3:** Plot of  $^1\text{H}$  relaxation times  $T_{1,H}$  of central peaks of pure E7 as a function of the spinning rate under MAS at 298 K.

Due to well-ordered molecules E7 has a strong dipolar interaction in the nematic phase (cf. large splitting in  $^1\text{H}$  spectra in Chapter 4), which may explain why it behaves similar to glycine. Therefore,  $T_{1,H}$  of E7 decreases at higher spinning rate at 298 K. For better comparison, the same spinning rate of  $\omega=3$  kHz was chosen for the  $T_1$

measurement of all samples, reported in the following.

### **Temperature dependence**

$^1\text{H}$  spectra of pure E7 are temperature dependent and show a big change from the nematic phase to the isotropic phase (cf. Fig. 4.6 in Chapter 4). Therefore, an effect of the phase transition should be expected in the relaxation experiments. In the following, the temperature dependence of the spin-lattice relaxation time  $T_{1,\text{H}}$  will be presented to study the phase behavior and dynamics of E7 and its mixture with TMPTA.

In figure 6.4 the relaxation times as a function of temperature are shown for pure E7 and a mixture containing 50 % E7. The empty hexagonal symbols represent pure E7 and the half-filled hexagons correspond to E7 in the mixture. For pure E7, a discontinuity appears around 62 °C at the phase transition from the nematic to the isotropic phase. The pure E7 has smaller relaxation times in the nematic phase compared with the isotropic one due to the more restricted and slower motion in the ordered nematic phase. Within each phase,  $T_{1,\text{H}}$  increases continuously with increasing temperature. No discontinuity or jump, however, is observed for  $T_{1,\text{H}}$  of E7 in the mixture upon variation of the temperature. This demonstrates that no phase transition occurs in the mixture in the measured temperature range. The observation is in good agreement with the results obtained from the analysis of the  $^1\text{H}$  spectral splitting and from polarizing optical microscopy, cf. Chapter 4.

Higher temperature induces faster motions and therefore results in longer relaxation times (see high temperature region of figure 6.1). As can be seen in figure 6.4, the same types of protons of E7 relax faster in the E7/TMPTA mixture than in pure E7 at a given temperature. This can be attributed to the increase of the viscosity by mixing with TMPTA.

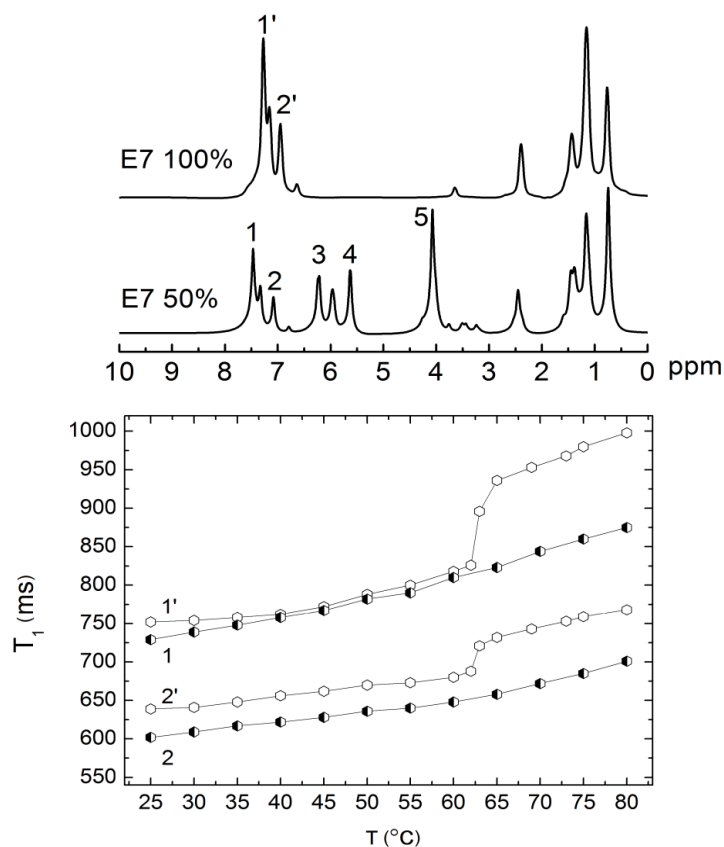


**Figure 6.4:** Comparison of the temperature dependence of  $T_1$  relaxation times for pure E7 and for E7 in a 50 % mixture with TMPTA. All experiments were carried out under MAS at 3 kHz. Corresponding peaks are shown on top. The empty hexagons represent pure E7 and the half-filled hexagons represent E7 in the mixture.

The proton spin-lattice relaxation of the different components in the 50 % TMPTA/E7 mixture and of the different proton sites in a given molecule are analyzed for investigating the temperature dependence of motion. Figure 6.5 presents the temperature dependence of spin-lattice relaxation times of the mixture. Curves 1 and 2 represent the aromatic protons of E7. Their relaxation times increase steadily with increasing temperature. Curves 3 and 4, which share a similar temperature dependence, give the trends of protons attached to carbons of C=C double bonds in TMPTA. The protons of the CH<sub>2</sub>O group located in the center of the TMPTA molecules relax faster (curve 5) than the protons in C=C groups (curves of 3 and 4). This may have two reasons. First, the center of the molecule has a smaller mobility than the C=C in the periphery of the molecules. Second, the dipolar coupling networks

of the different types of protons are different. However, the higher mobility of the C=C protons is reflected in the position of the  $T_1$  minimum (only seen as a plateau for the C=C protons). The C=C atoms with faster motion reach the minimum in  $T_{1,H}$  at a lower temperature compared with the protons with slower motion. Here, protons in CH<sub>2</sub>O and CH=CH<sub>2</sub> groups follow the correlation time theory in section 6.1. Peak 7 is a superposition of E7 and TMPTA and shows a biexponential relaxation behavior which is not given here.

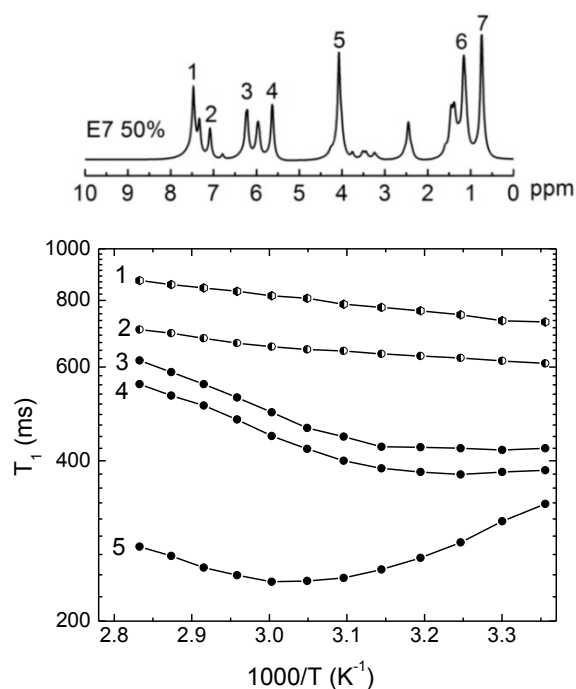


**Figure 6.5:** The longitudinal relaxation times  $T_{1,H}$  of a TMPTA/E7 mixture containing 50 % E7 as a function of temperature. The half-filled hexagons represent the aromatic protons of E7 in the mixture and the full circles are the TMPTA protons.

### Concentration dependence

The aromatic protons of E7 having larger relaxation times than TMPTA (shown in figure 6.5) is true also for mixtures of other concentrations. Figure 6.6 shows  $T_{1,H}$  as a function of increasing mass fraction of E7 in the mixtures. The overall trends show that the aromatic protons of E7 relax more slowly than TMPTA protons throughout the range of the mixtures.



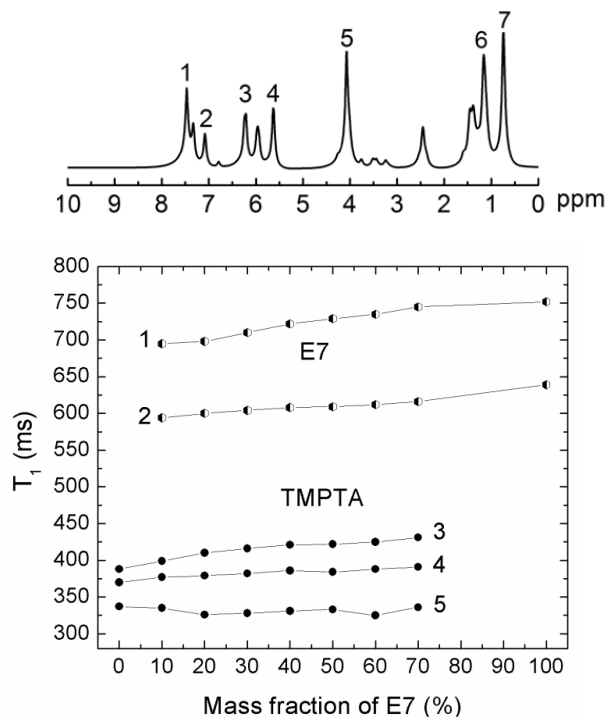


**Figure 6.6:** Relaxation times  $T_{1,H}$  as a function of increasing mass fraction of E7 in the mixtures, measured under MAS at 3 kHz, 303 K. The half-filled hexagons represent the aromatic protons of E7 in the mixture and the full cycles TMPTA protons.

The increase of  $T_{1,H}$  shows that the motion of molecules becomes faster with increasing weight fraction of E7 in the mixtures. The results here are in good agreement with the ones obtained from diffusion measurement for the mixtures, see Chapter 5.

Figure 6.7 presents relaxation data for different sites of E7 as a function of the E7 concentration in the mixtures. Both aromatic (1) and aliphatic (6) protons of E7 relax more slowly at higher concentration of E7. When comparing the 50 % values in Fig. 6.7 with Fig. 6.5, one finds that the aliphatic E7 protons have relaxation times similar to those of TMPTA, whereas the aromatic protons have much larger relaxation times. This difference cannot be explained on the basis of different correlation times (which should be larger for aromatic protons) but must be due to different relaxation strength based on different dipolar coupling networks. The relaxation times of aromatic protons do not change as much as those of the aliphatic ones. This can be explained by the

more rigid structure of the aromatic rings. From 10 % to 100 % mass fraction of E7, the change of relaxation times of the benzene rings is about a factor of 1.07 (750/700) compared to a factor of 1.44 (475/330) for aliphatic protons. This means that the long chains of the aliphatic protons are more flexible and consequently more strongly affected by the mixing with another component.

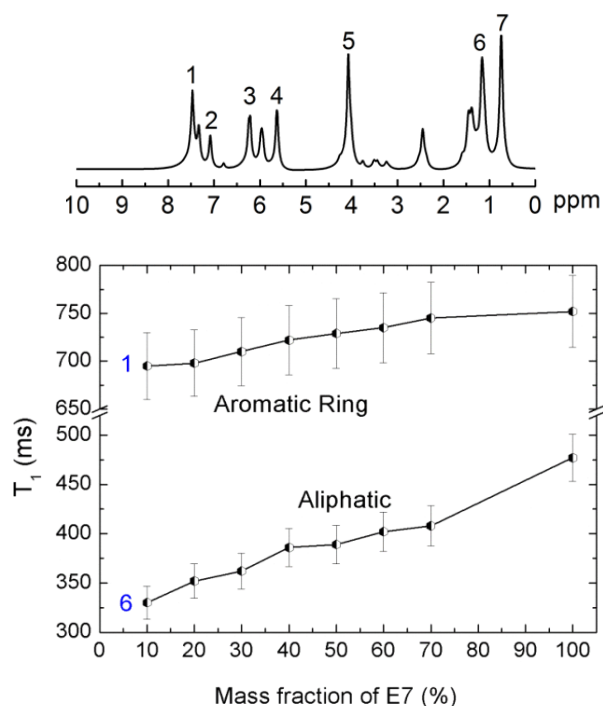


**Figure 6.7:** Relaxation times  $T_{1,H}$  of E7 as a function of increasing mass fraction of E7 in the mixtures, measured under MAS of 3 kHz at 303 K. The error bars represent an estimated error of 5 %.

### 6.3.2 Carbon spin-lattice relaxation in the rotating frame, $T_{1\rho,C}$

Due to the strong homonuclear coupling of protons in the polymer, its NMR spectra are broad and featureless and  $T_{1,H}$  cannot be resolved for different proton sites in this system. The measurement of  $T_1$  of carbon atoms, which show resolved spectra under MAS, requires long experiment time because direct  $^{13}\text{C}$  excitation instead of cross polarization must be used. A more easily accessible relaxation time is that of spin-lattice relaxation in the rotating frame,  $T_{1\rho}$ . This relaxation time can be obtained from the well resolved  $^{13}\text{C}$  spectra by applying cross polarization from protons or direct excitation of carbons for detection. By variation of a carbon spin lock period following

cross polarization from protons, the decay of  $^{13}\text{C}$  magnetization with increasing spin lock period  $\tau$  can be observed. The theory and pulse sequence are described in section 6.2. Alternatively, for samples with fast reorientation, which are not suitable for cross polarization, a direct  $90^\circ$  pulse was used to excite the carbon magnetization directly. In the case of TMPTA, the latter pulse sequence without CP was applied (the pulse sequence is listed in appendix A8). The same spin lock power (72 kHz) and spin rate ( $\omega=5$  kHz) were used in the experiments. The temperature dependence of the  $^{13}\text{C}$  spin-lattice relaxation in the rotating frame,  $T_{1\rho,C}$ , for different samples (E7, TMPTA, PTMPTA, PDLC) is presented in the following.

### Bulk E7

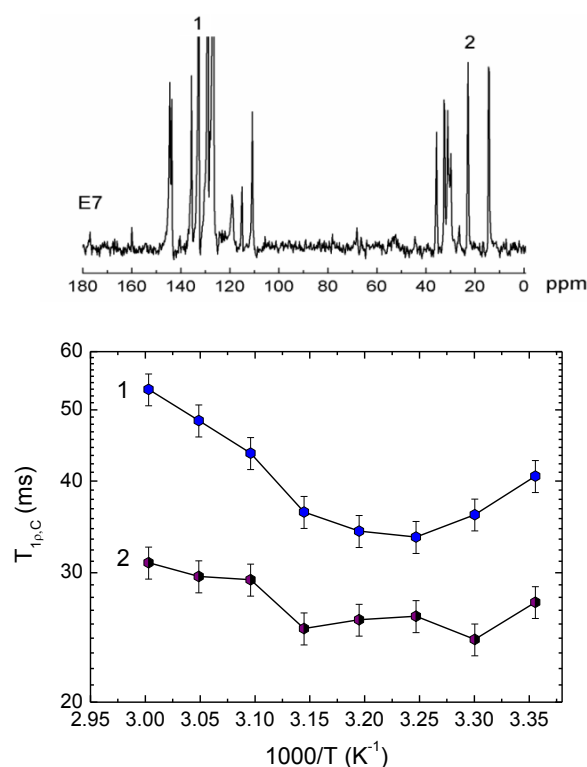


**Figure 6.8:**  $T_{1\rho,C}$  of E7 as a function of temperatures. Curve 1 represents the aromatic carbons shown in the top spectra. Curve 2 is for the aliphatic carbons at about 23 ppm indicated in the spectra. All measurements were carried out under CPMAS at 5 kHz. The error bars represent an estimated error of 5%.

Figure 6.8 presents the temperature dependence of  $T_{1\rho,C}$  for aromatic and aliphatic carbons of pure E7 below the phase transition temperature  $T_{\text{NI}}$ . The relaxation time of

the aromatic carbons (curve 1) goes through a minimum. For the aliphatic protons (curve 2) no minimum can be assigned because of the scattering of the data. At the same temperature, aromatic carbons relax more slowly than aliphatic carbons due to the smaller number of directly bonded protons. This is in analogy to  $T_{1,H}$  shown in figures 6.5 and 6.7. Furthermore, the aromatic carbons show stronger temperature dependence than the aliphatic carbons.

## TMPTA

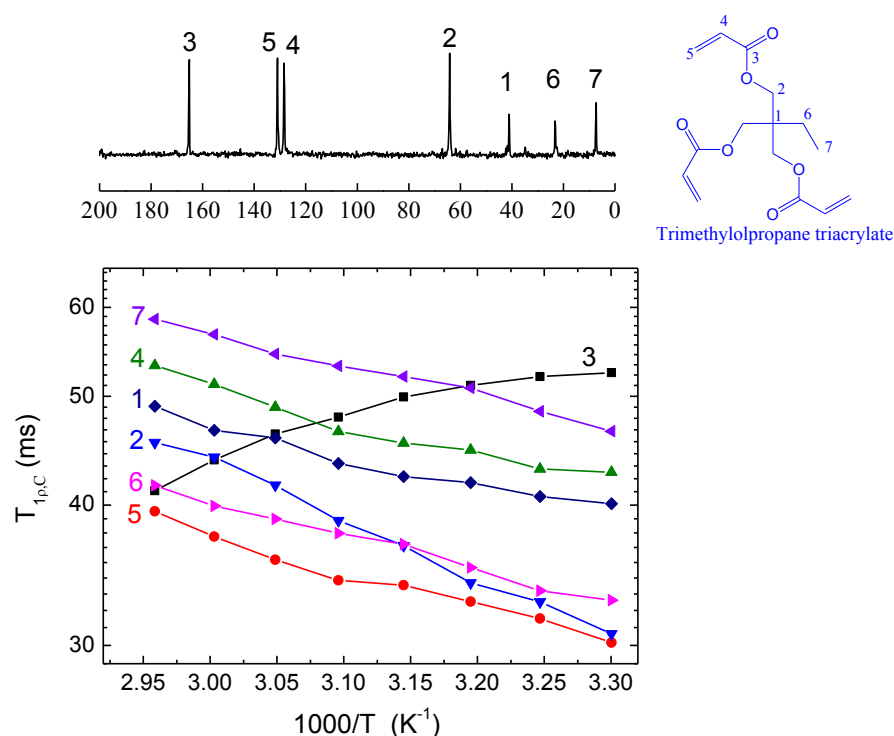


**Figure 6.9:**  $T_{1\rho,C}$  of TMPTA as a function of temperature. The data here were obtained by direct excitation of  $^{13}\text{C}$  without cross polarization from  $^1\text{H}$  due to the fast reorientation of TMPTA and under MAS with a spinning rate of 5 kHz and the same spin lock power (72 kHz) as for E7. The structure and  $^{13}\text{C}$  spectrum assignments of TMPTA are shown on top.

Figure 6.9 shows the temperature dependence of  $T_{1\rho,C}$  for TMPTA. As anticipated for the small TMPTA molecule, all carbon relaxation rates decrease as the temperature increases except the carbons (3) of the carbonyl  $\text{C}=\text{O}$  group. The relaxation time of  $\text{C}=\text{O}$  carbons shows an opposite trend which may be attributed to a different relaxation process. Looking at the relaxation times at higher temperature (cf. Fig. 6.9) we obtain

the following sequence, starting from the group with the shortest relaxation time: =CH<sub>2</sub> (5), ethyl-CH<sub>2</sub> (6), CH<sub>2</sub>O (2), quaternary C (1), CH= (4), CH<sub>3</sub> (7). To understand this sequence both the mobilities and the dipolar coupling networks of the different carbon sites must be considered. The long relaxation time of the CH<sub>3</sub> group, for example, is due to the very high frequency of methyl rotation. The slow relaxation of the quaternary carbon, on the other hand, is due to the lack of directly bonded protons.

## PTMPTA

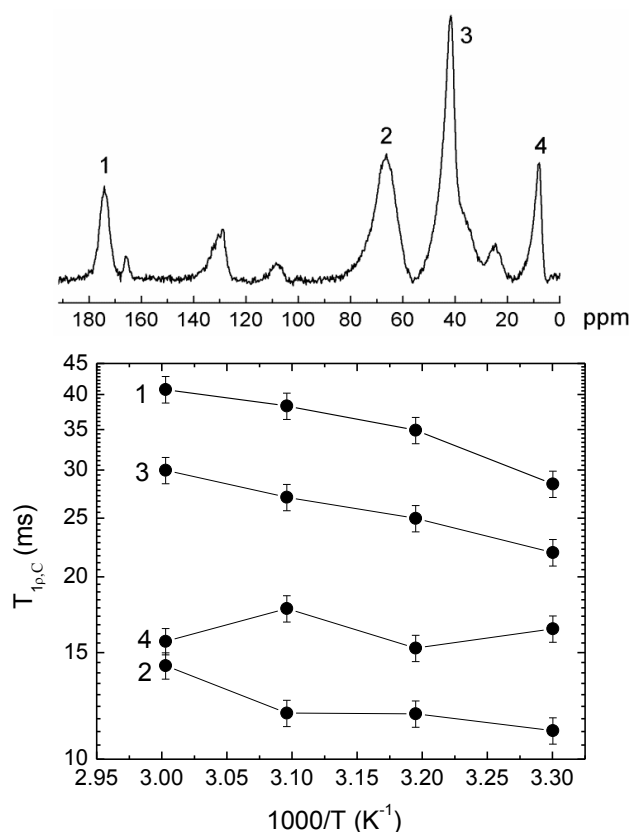


**Figure 6.10:**  $T_{1,\rho,C}$  of the polymer PTMPTA as a function of temperature. The data were obtained under CPMAS at 5 kHz. The error bars represent an estimated error of 5 %.

The relaxation times for PTMPTA as a function of temperature are shown in figure 6.10. All carbons show only little changes in  $T_{1,\rho,C}$  with increasing temperature. The largest temperature dependence is observed for the carbons (1) of the carbonyl (C=O) group. The end group carbon CH<sub>3</sub> (4) and the central carbons (2) (CH<sub>2</sub>O) do not change too much.

## Comparison of PTMPTA and PDLC

In order to check the change of dynamics when going from the precursor mixture TMPTA/E7 to the final polymer system, the relaxation behavior of different samples will be compared in following. At first, PTMPTA and a PDLC sample containing 50 % E7 will be compared.

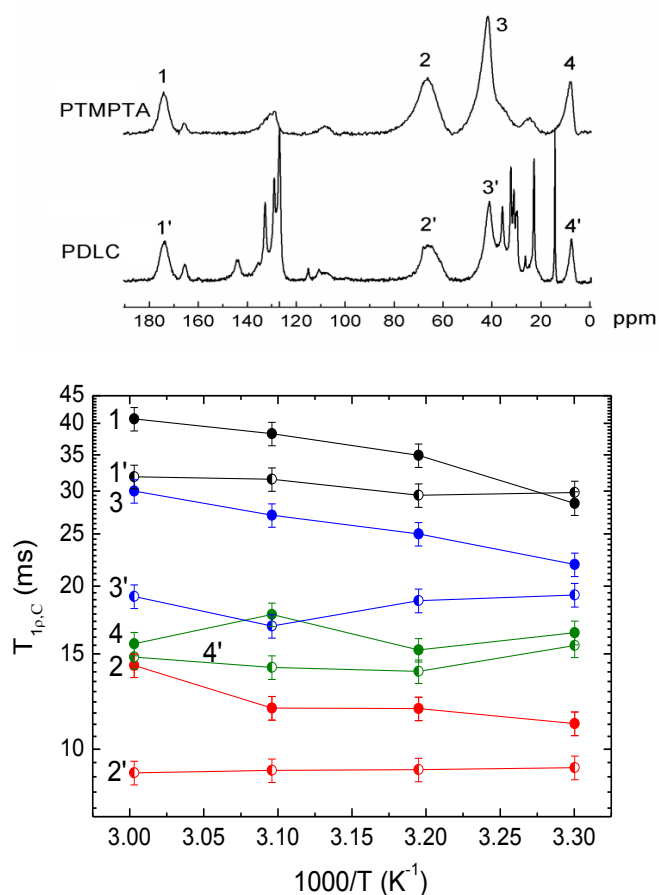
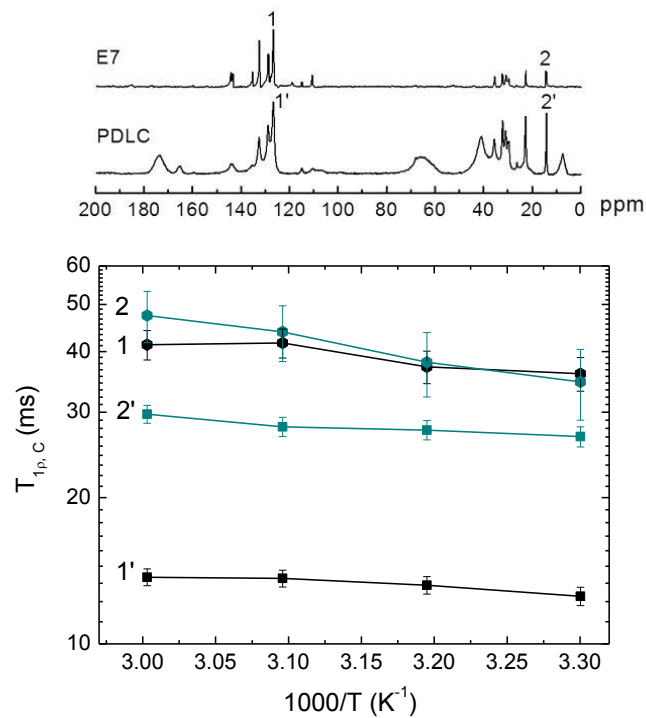


**Figure 6.11:**  $T_{1,\rho,C}$  of a PDLC sample containing 50 % E7 as a function of temperature. The data were obtained under CPMAS at 5 kHz. The full cycles represent PTMPTA and half cycles PDLC. The same color stands for the same peak sharing the same chemical shift. The error bars represent an estimated error of 5 %.

In figure 6.11 the relaxation times  $T_{1,\rho,C}$  for the pure polymer PTMPTA and for a PDLC containing 50 % E7 are compared to probe the influence of the liquid crystal droplets on the polymer matrix. Overall, the relaxation times of both PTMPTA and PDLC become larger when increasing the temperature. In addition, the relaxation times  $T_{1,\rho,C}$  in the pure polymer PTMPTA are larger than in the PDLC throughout the

temperature range under investigation. In PTMPTA, the network or chains can be somewhat flexible or/and mobile due to the space between atoms in the amorphous structure of the polymer. However, in the PDLC sample, some of the LC molecules may penetrate into the polymer matrix to occupy the free volume in PTMPTA making the matrix more rigid. Therefore, LC shows an anti-softening effect on the polymer matrix. This is similar to observations on polycarbonate.<sup>[128]</sup> Schmidt and coworkers found that the addition of small molecules increases the correlation time  $\tau_c$  of polycarbonate.<sup>[128]</sup> Furthermore, the variations of PTMPTA are larger than those of PDLC, indicating that PTMPTA is more temperature sensitive than PDLC.

### Comparison of E7 and PDLC



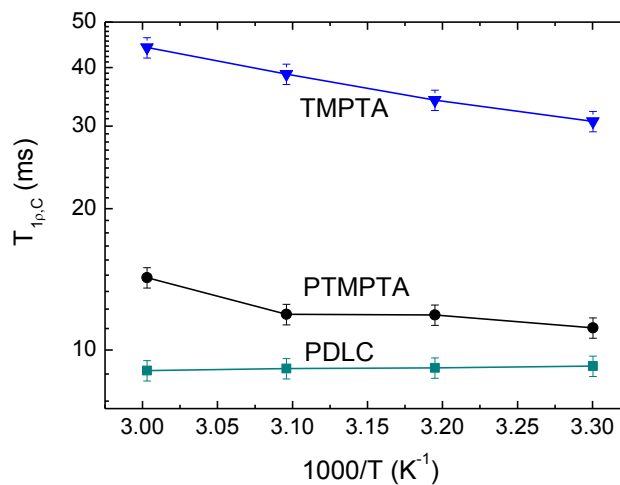
**Figure 6.12:** Temperature dependence of  $T_{1\rho,C}$  for E7, and a PDLC sample containing 50 % E7. The hexagons are for E7 and squares for PDLC. The same color stands for the same type of peak sharing the same chemical shift. The error bars represent an estimated error of 5 %.

Figure 6.12 shows the temperature dependence of  $T_{1\rho,C}$ , of the liquid crystal E7 in the bulk and in a PDLC sample containing 50 % E7. Both aromatic carbons (1) and

aliphatic carbons (2) of E7 are hindered by the polymer matrix to slow down the motion of E7, resulting in shorter relaxation times. The polymer surface induces order of the LC molecules along the boundary but increases the relaxation rate in the LC dispersion compared to the bulk LC.<sup>[41, 110, 129]</sup> In addition, the reduction in  $T_{1\rho,C}$  of aromatic carbons seems about twice as much as of aliphatic carbons. This may demonstrate that the aromatic cores in E7 droplets are probably aligned parallel to the interface. Furthermore, higher temperature induces larger  $T_{1\rho,C}$ , which is consistent with the correlation time theory.

### Comparison of TMPTA, PTMPTA and PDLC

Figure 6.13 shows the temperature dependence of  $T_{1\rho,C}$  of the  $\text{CH}_2\text{O}$  groups in the monomer unit for TMPTA, PTMPTA and a PDLC sample containing 50 % E7. It is very clear that  $T_{1\rho,C}$  shows a large reduction after polymerization to PTMPTA or PDLC.



**Figure 6.13:** Comparison of temperature dependence of  $T_{1\rho,C}$  for TMPTA, PTMPTA and a PDLC sample containing 50 % E7. The values for the  $\text{CH}_2\text{O}$  peaks at 63 ppm denoted 2 and 2' in figure 6.11 and 3 in figure 6.9 are shown. The error bars represent an estimated error of 5 %.

Obviously, the monomer TMPTA became rigid after polymerization to PTMPTA and all monomer units are confined in a local cage. The strong steric interaction with other segments reduces the frequency of their motion and shortens the relaxation times. In



the PDLC, the motion is further slowed down since the polymer network is penetrated by the liquid crystal molecules, as discussed above (cf. Fig. 6.11).

### 6.3.3 Proton spin-lattice relaxation in the rotating frame, $T_{1\rho,H}$

Varying the contact time in cross polarization experiments and measuring the  $^{13}\text{C}$  intensities can be used to determine  $T_{1\rho,H}$ . The details of the pulse sequence and of the analysis are shown in section 6.1. One can easily distinguish the difference of the relaxation rate from the intensity curves. Furthermore, the optimum contact time can be found in these curves. The cross polarization curves of the different samples are shown below.

#### PTMPTA and PDLC

Figure 6.14 presents the intensities of the C=O peak in PTMPTA and the 50 % PDLC sample as function of contact time. PDLCs have a larger relaxation rate. In the PDLC the maximum magnetization is reached faster ( $\sim 1.5$  ms) than in the polymer PTMPTA ( $\sim 3.8$  ms). These contact times for maximum intensity can be further used in the spectra and other measurements, such as  $T_{1\rho,C}$ .

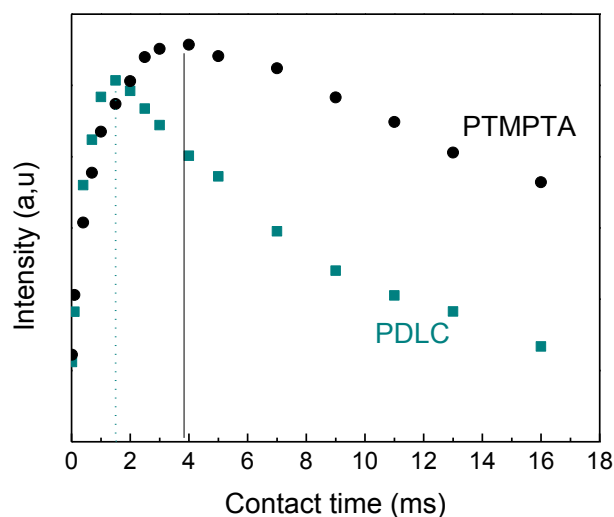


**Figure 6.14:** Intensity of  $^{13}\text{C}$  spectra as a function of CP contact time. The half blue cycles represent the C=O peak of 175 ppm in PDLCs and the black cycles are the same peak in PTPMPTA (peaks 1' and 1 in figure 6.11 respectively). Measured at 298 K.

## Cross polarization oscillations

Figure 6.15 shows the comparison of the CP curves for pure E7 and E7 in a PDLC sample containing 50 % E7. Pure E7 has stronger dipolar coupling and the magnetization for carbon can be built up very quickly. The magnetization of pure E7 shows an oscillation in the CP measurement. This phenomenon of an oscillating intensity is absent when E7 is dispersed in a polymer matrix, namely in the PDLC.

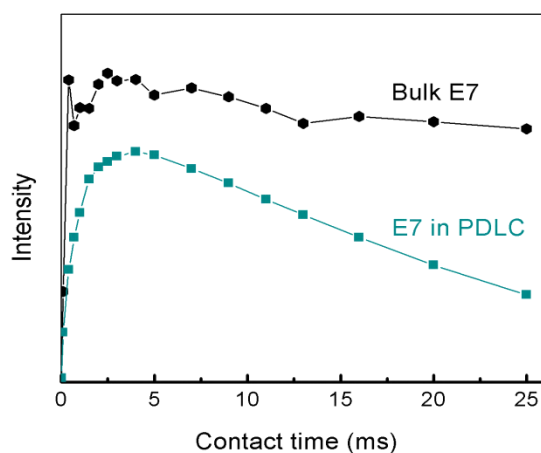


**Figure 6.15:** Intensity of  $^{13}\text{C}$  signal (peaks 2 and 2' of figure 6.12) of E7 and a PDLC sample containing 50 % E7 as a function of CP contact time, measured at 303 K under MAS with  $\omega=5$  kHz.

It should be kept in mind that a smooth cross polarization curve results from fast spin diffusion. If the rate of spin diffusion away from the C-H pair is not large enough compared with the cross polarization rate, then the magnetization oscillates between the proton and carbon nuclei of the pair. Mueller and coworkers first found that the magnetization goes back and forth in single crystals of ferrocene<sup>[121]</sup> by measuring protonated  $^{13}\text{C}$  spectra with short CP contact times. Oscillations also have been observed in other cases when the dipolar couplings of a carbon to its nearest neighbor protons are much larger than the coupling of this spin system to the rest of spins.<sup>[121, 130]</sup> Tian and Cross investigated the  $^1\text{H}$ - $^{15}\text{N}$  cross polarization in gramicidin A oriented in a hydrated lipid bilayer.<sup>[131]</sup> The oscillation disappeared for the deuterated sample. For weak H-C heteronuclear dipolar interactions and moderate or strong H-H homonuclear dipolar interactions, the CP behavior follows the conventional smooth

curve without oscillation.

In liquid crystals this oscillation was first found by Pratima and Ramanathan.<sup>[130]</sup> They applied the oscillation in CP to determine the H-C dipolar couplings and the order parameters of C-H bond axes with respect to the director in the case of the liquid crystal *N*-4-methoxybenzylidene-4-butylaniline (MBBA). Chattah studied H-C and H-H couplings of 8CB by fitting the oscillation in CP with different models,<sup>[132]</sup> namely anisotropic, purely dipolar and isotropic models. They found that the anisotropic model provides the best fittings. Levstein et al. modified polarization echoes to investigate the dynamics through the oscillation in MBBA.<sup>[133]</sup>

These oscillations, once observed, are orientation and temperature dependent. Figure 6.16 shows the temperature dependence of cross polarization of the liquid crystal E7. Higher temperature increases the spin diffusion rate and increases the smoothness of the CP curve. All oscillations show a decrease of the oscillation frequency at higher temperature due to the change of the rate of spin diffusion and the weakening of heteronuclear coupling.

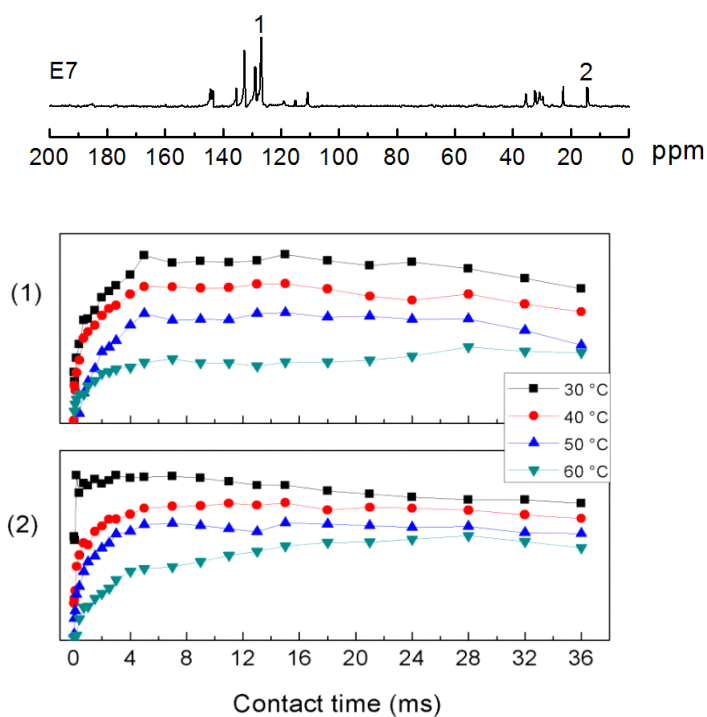


**Figure 6.16:** Intensity of <sup>13</sup>C spectra as a function of CP contact time. Squares represent 30 °C, circles for 40 °C, triangles for 50 °C and inverted triangles for 60 °C.

Back to the PDLC system under investigation, not only the layer close to the boundary but also the deeper layers can feel the effect of anchoring from the polymer. In bulk E7, the well-ordered rod-like molecules exhibit a unique H-C dipolar coupling, similar to an isolated H-C pair, which leads to oscillations in the cross-polarization curve.<sup>[131]</sup> However, in PDLCs, the anchoring effect at the boundary between the polymer and LC droplets disturbs the molecular order. It is difficult to get all E7 molecules aligned even when immersed into a magnetic field  $B_0$  (see the random anchoring points in figure 1.1). On the other hand, the reduced average order of the LC molecules due to the anchoring effect and the director distribution in each droplet averages the heteronuclear coupling. As a result, a smooth cross polarization curve is obtained for E7 in PDLC.

### Temperature dependence of cross polarization of E7 in PDLC

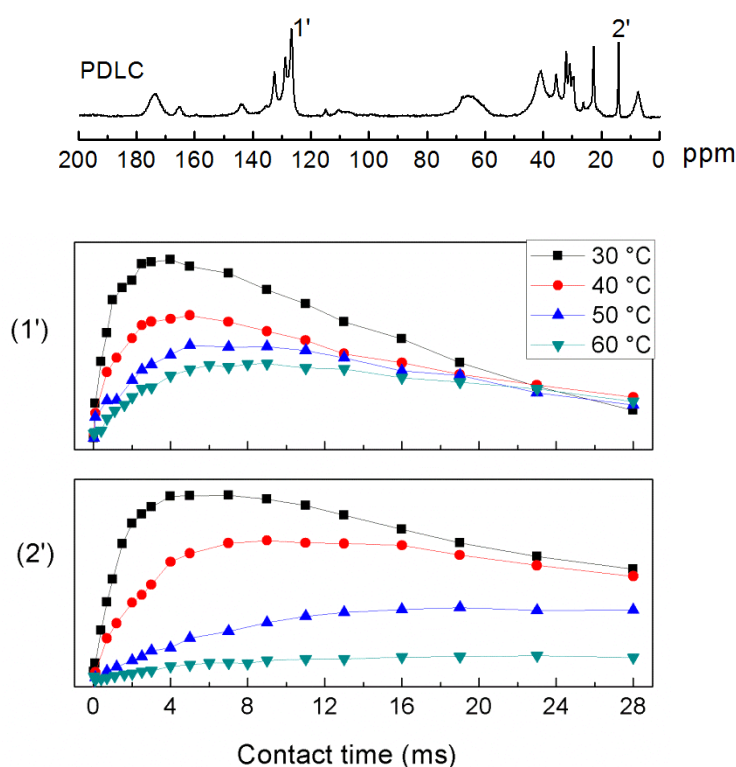


**Figure 6.17:** Intensity of  $^{13}\text{C}$  spectra as a function of CP contact time. Squares represent 30 °C, circles for 40 °C, triangles for 50 °C and inverted triangles for 60 °C.

Figure 6.17 indicates the cross polarization between proton and carbon atoms of

different positions for a PDLC sample containing 50 % E7. Higher temperature weakens the dipolar-dipolar interaction and results in longer times for the carbon magnetization to reach its maximum for both aromatic and aliphatic carbons. Additionally, the maximum intensity of carbons decreases, so does the relaxation rate, which can be observed from the smaller slope of the CP curves.

The observed increase in  $T_{1\rho,H}$  with higher temperature is good in agreement with the  $T_{1\rho,C}$  results obtained from varying the spin locking time (section 6.2.2). Results from fitting the aromatic peak (1') at 135 ppm to get the CP contact times  $T_{CH}$  and  $T_{1\rho,H}$  using eq. (6.11) are summarized in table 6.1.

**Table 6.1:** The cross polarization time constants and  $T_{1\rho,H}$  of PDLCs:

$T$ (°C)	30	40	50	60
$T_{CH}$ (ms)	0.994	1.24	2.66	2.87
$T_{1\rho,H}$ (ms)	18.84	24.55	26.82	32.69

#### 6.4 Conclusions

The phase transition temperature  $T_{NI}$  of E7 obtained by proton  $T_1$  measurements is in good agreement with the results obtained from the analysis of the  $^1H$  spectra and by polarizing optical microscopy. Both  $T_1$  and  $T_{1\rho}$  increase with increasing temperature (with the exception of  $T_{1\rho,C}$  of the C=O group of TMPTA). Thus all data fall on the high-temperature (short  $\tau_c$  correlation time) branch of the  $T_1$  curve (cf. Fig 6.1), which means that faster motion leads to larger  $T_1$ . Larger  $T_1$  values in the mixtures with higher E7 concentration can be explained by the lower viscosity. This result is in good agreement with the faster diffusion in liquid crystal rich mixtures. The  $T_{1\rho,C}$  reduction from bulk E7 to PDLC indicates that E7 molecules are hindered by the polymer matrix. Similarly, the  $T_{1\rho,C}$  reduction from TMPTA to PDLC and PTMPTA is due to the immobile polymer networks, which slow down the motion of the monomer units. Most interestingly, the relaxation results indicate that the mobility of the polymer segments in the pure polymer is higher than in the PDLC matrix. This is explained by an anti-softening of the matrix by E7 molecules. Oscillations during cross polarization,

which are present in bulk E7, disappear in the PDLC, indicating that the anchoring of the liquid crystal molecules at the droplet surface reduces the order of the liquid crystals.

## Chapter 7 Summary

The structure and dynamics of polymer-dispersed liquid crystals (PDLCs) and their precursor mixtures consisting of the liquid crystal E7 and the monomer trimethylolpropane triacrylate (TMPTA) were investigated by solution and solid state  $^1\text{H}$  and  $^{13}\text{C}$  NMR spectroscopy, by NMR relaxometry, and by NMR diffusometry using pulsed field gradients (PFG).

First of all, the  $^{13}\text{C}$  CPMAS technique had to be implemented on a 300 MHz Tecmag Apollo NMR spectrometer. The spinning angle was adjusted to the magic angle, the cross polarization condition was optimized, and the pulse sequences for the measurement of spectra and relaxation times were set up. Well-resolved  $^{13}\text{C}$  CPMAS NMR spectra of crystalline and amorphous organic compounds and polymers were obtained showing that the set-up was successful.  $^{13}\text{C}$  CPMAS NMR was used to verify a series of chemical modifications of polymeric colloid particles and may be used to approximately quantify the concentration of cross-linker in PMMA colloids.

For the investigation of the PDLC system,  $^1\text{H}$  and  $^{13}\text{C}$  NMR spectra of the pure components TMPTA and E7, of TMPTA/E7 mixtures, of the pure polymer, and of PDLCs have been analyzed and peaks have been assigned to the different species. The temperature dependence of the  $^1\text{H}$  spectra of E7 shows that E7 starts to become isotropic at 61.5 °C, but the nematic broad spectra disappear completely only at 63.7 °C. The transition range has a finite width, in which narrow isotropic peaks and broad nematic peaks coexist, because E7 is a mixture of several LC compounds. The temperature dependence of the splitting in the proton spectra of liquid crystals was used for determining the nematic order parameters by employing a Haller analysis. NMR spectra demonstrate that adding TMPTA to E7 lowers the nematic-to-isotropic phase transition temperature  $T_{\text{NI}}$ . This is confirmed by polarizing optical microscopy, which shows the nematic phase at lower temperatures in the mixtures of TMPTA/E7. Mixtures containing less than 70 % E7 are isotropic at room temperature.

The properties of PDLCs strongly depend on the degree of phase separation, the size and orientation of liquid crystal droplets, which are determined by the composition of precursor mixtures and the formation rate. In a simple reaction-diffusion model for the formation of a holographic PDLC (HPDLC), the diffusion coefficient of the monomer in the precursor mixture is an important parameter. NMR diffusometry with a pulsed-field gradient stimulated echo (PFG-STE) pulse sequence offered a reliable way to measure the diffusion coefficients of each component in the precursor mixture. The diffusion coefficient obtained here was used in the reaction-diffusion model and good agreement was found between the simulation and experimental results. In addition, both TMPTA and E7 were found to diffuse faster when the weight fraction of E7 increases. In each mixture, TMPTA diffuses more slowly than E7 due to the larger hydrodynamic radius of TMPTA. Furthermore, diffusion in the PDLC system shows that the interface of polymer and E7 restricts the diffusion of the liquid crystal molecules, resulting in a reduced apparent diffusion coefficient compared to bulk E7. This is consistent with the diffusion distance (displacement:  $4.2\mu\text{m}$ ) of E7 molecules in the bulk being larger than the average diameter of E7 droplets ( $\sim 1.4\mu\text{m}$ ) measured by polarizing optical microscopy.

The spin-lattice relaxation time  $T_1$  increases discontinuously in bulk E7 when heating through the nematic-to-isotropic transition temperature. The phase transition temperature  $T_{\text{NI}}$  of E7 obtained from the  $T_1$  curve is in good agreement with the results obtained from the analysis of the  $^1\text{H}$  spectra and polarizing optical microscopy. E7 relaxes more slowly in the isotropic phase than in the nematic phase due to the higher mobility in the isotropic liquid. The concentration dependence of  $T_1$  in the mixtures of E7 and TMPTA shows that increasing the concentration of E7 promotes the molecular motions in the mixtures, which is attributed to the higher mobility of the rod-like E7 molecules, which are smaller than the bulky monomer molecules. This is also in good agreement with the results obtained for the diffusion coefficients in liquid crystal rich mixtures.

The  $^1\text{H}$  spectra of PDLCs and polymer present poorly resolved features providing little



information. And  $T_1$  measurements of carbon require long experimental time because direct  $^{13}\text{C}$  excitation must be used. Therefore, only spin-lattice relaxation times in the rotating frame,  $T_{1\rho}$ , which can be measured fast, were obtained from the well resolved  $^{13}\text{C}$  spectra by applying cross polarization.

Relaxation in the rotating frame shows that the relaxation times of both TMPTA and E7 decrease after polymerization to PDLC because of the restrictions by the solid polymer matrix. Similarly, the  $T_{1\rho,\text{C}}$  reduction from TMPTA to PTMTA is due to the almost immobile polymer network, which slows down the motion of the monomer units. In addition, the pure polymer PTMPTA has a larger  $T_{1\rho,\text{C}}$ , which indicates higher mobility, than PDLC throughout the temperature range under investigation. This is because the E7 molecules penetrate into the polymer matrix to occupy the space between polymer chains or segments, resulting in a less flexible chain network. The LC has an anti-softening effect on the polymer matrix.

Bulk E7 shows an oscillation phenomenon in the cross polarization curve due to well-ordered molecules. The spin system can be treated as a unique isolated H-C pair, which is only weakly coupled to the proton reservoir. The PDLC sample, however, shows a smooth cross polarization curve. This could be attributed to the anchoring effect at the boundary between the polymer and LC droplets, which reduces the order of the liquid crystal molecules.

In summary, both relaxation times and diffusion behavior were found to yield detailed structural and dynamic information on a molecular scale for PDLC systems.

## Appendix

### A1 Additional NMR spectra

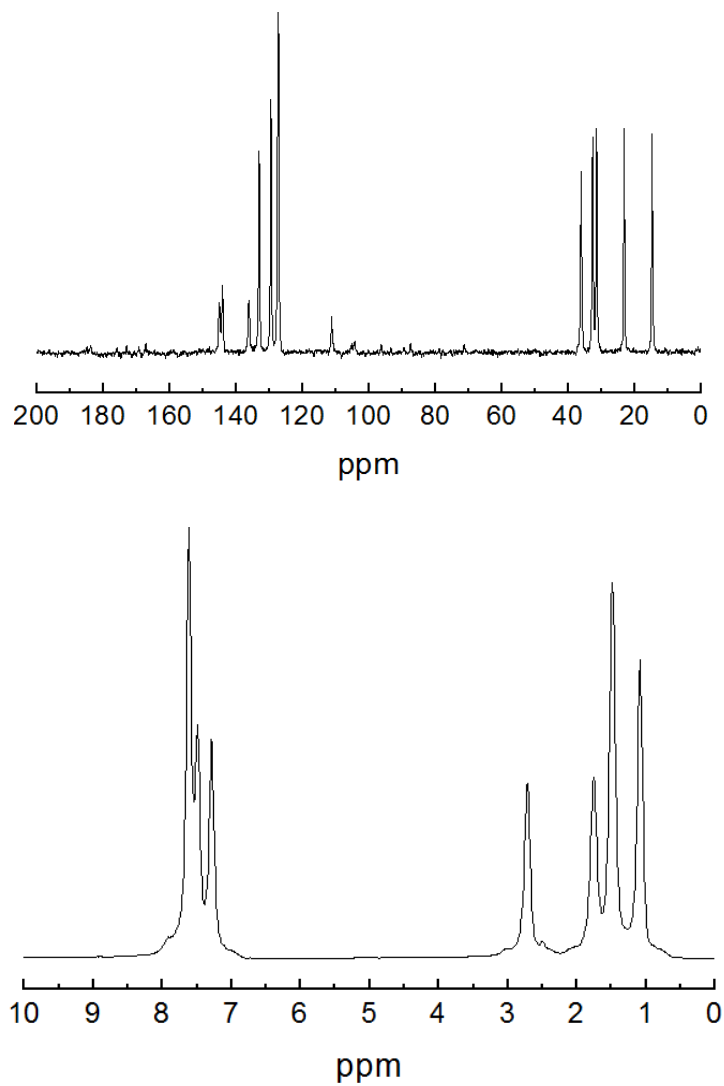


**Figure A1.1:** NMR spectra of 5CB. Top:  $^{13}\text{C}$  spectrum measured at 25°C under CPMAS. Bottom:  $^1\text{H}$  spectrum obtained at 40°C under static conditions without solvent. The spectra were recorded at 300 MHz (UPB).

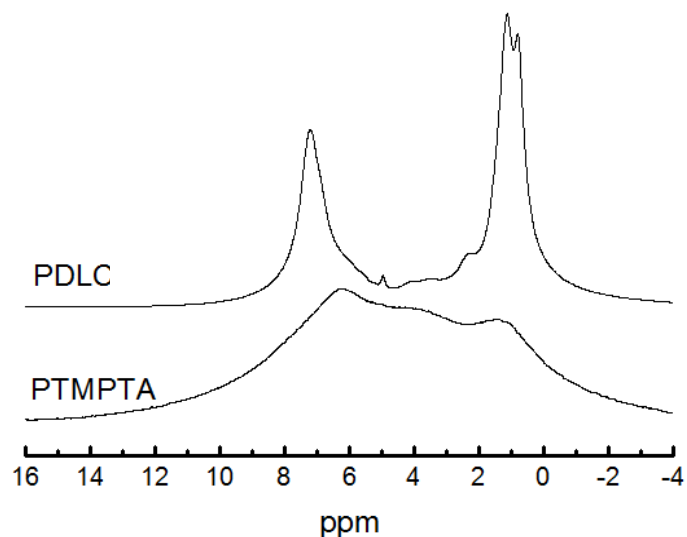


**Figure A1.2:**  $^1\text{H}$  spectra of a PDLC and PTMPTA, measured at 25 °C under MAS at 5 kHz. The spectrum was recorded at 300 MHz (UPB). The samples were illuminated by sunlight to initiate polymerization.

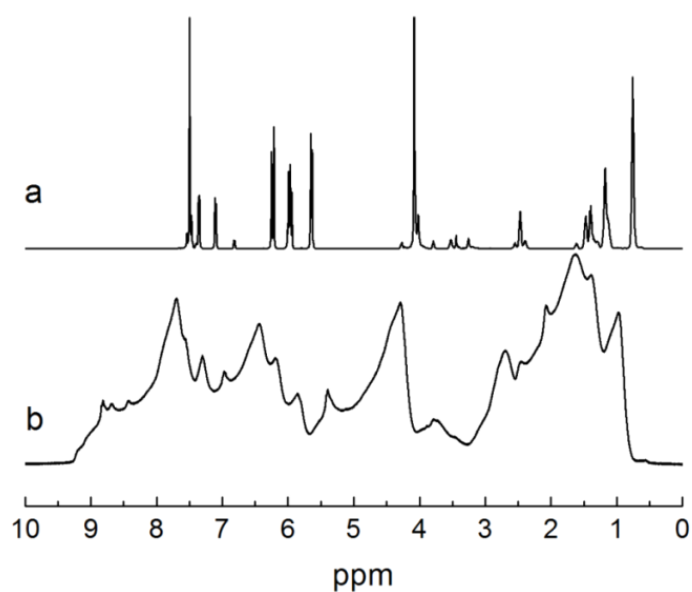


**Figure A1.3:** a:  $^1\text{H}$  spectrum of a mixture containing 40 % E7, measured at 25 °C under static conditions without solvent. b: Spectrum of the same sample which was deliberately placed outside of the homogeneous region of the  $B_0$ -field. The spectra were recorded at 500 MHz with a high-resolution NMR spectrometer (UPB).

## A2 Photographs of PDLCs

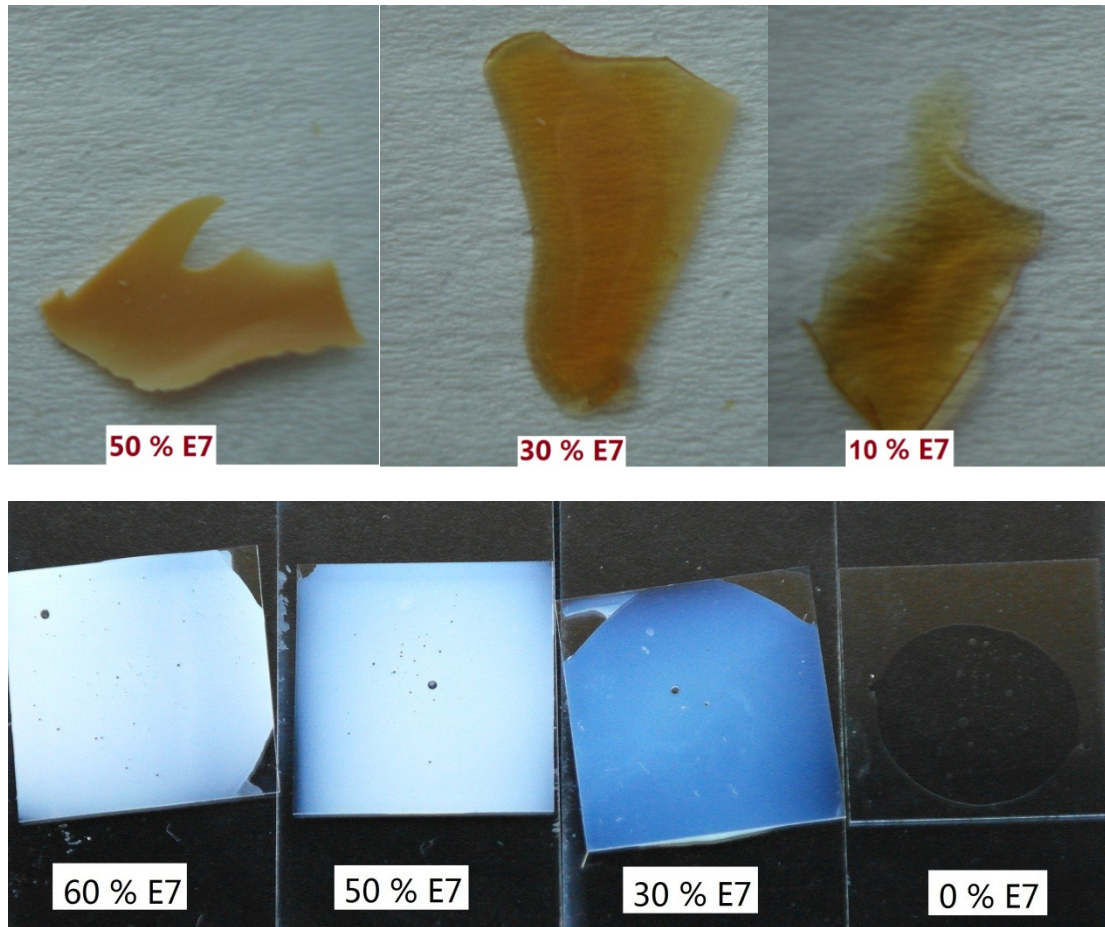


**Figure A2.1:** Photographs of PDLC samples with different mass fraction of E7. A larger concentration of E7 reduces the transparency of PDLCs due to the stronger scattering of the liquid crystal droplets. The samples were obtained by illuminating the precursor mixture on an evaporating dish (top) or between microscopy slides (bottom) with sunlight.

### A3 Haller plot

The splitting of  $^1\text{H}$  NMR spectra, which is a measure of the order parameter  $S$ , as a function of temperature can be described by

$$\Delta\nu = \Delta\nu_0 \left(1 - \frac{T}{T_{\text{NI}}}\right)^B$$

$$\frac{\Delta\nu}{\Delta\nu_0} = S$$

where  $\Delta\nu$  is the splitting of the spectra and  $\Delta\nu_0$  the splitting when the sample is perfectly ordered with order parameter  $S=1$ ;  $T$  is the absolute temperature and  $T_{\text{NI}}$  is the nematic-to-isotropic phase transition temperature.

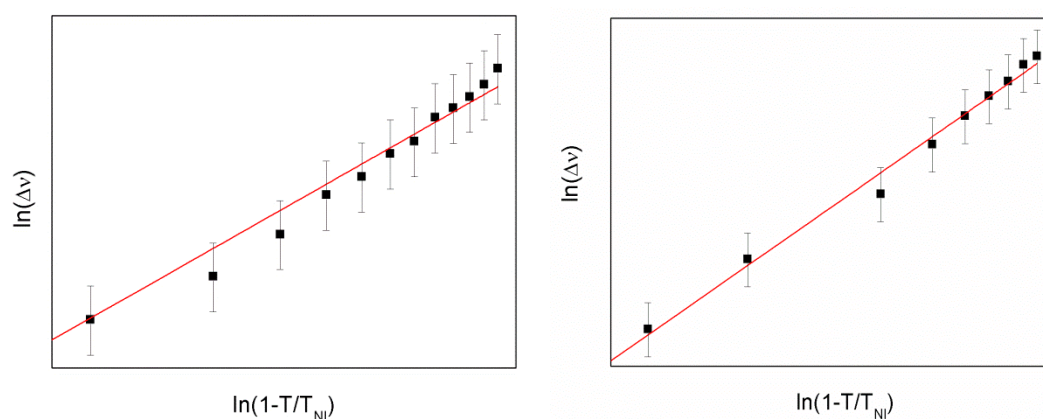


**Figure A3:** Haller plot of splittings, obtained from  $^1\text{H}$  spectra, for the liquid crystals 5CB (left) and E7 (right).

**Table A3:** Fitting results for the Haller plots of E7 and 5CB.

Liquid crystals	$T_{\text{NI}}$ ( $^{\circ}\text{C}$ )	B	$\Delta\nu_0$ (kHz)	S (25 $^{\circ}\text{C}$ )	S ( $T_{\text{NI}}$ )
5CB	37	0.125	19.65	0.694	0.417
E7	61.5	0.117	25.67	0.782	0.425

As can be seen in Table A3, the order parameter at  $T_{\text{NI}}$  obtained by using Haller analysis<sup>[134]</sup> is in good agreement with Maier-Saupe theory and with reported values in references.<sup>[135-137]</sup>

#### A4 Diffusion measurement: example of spectra

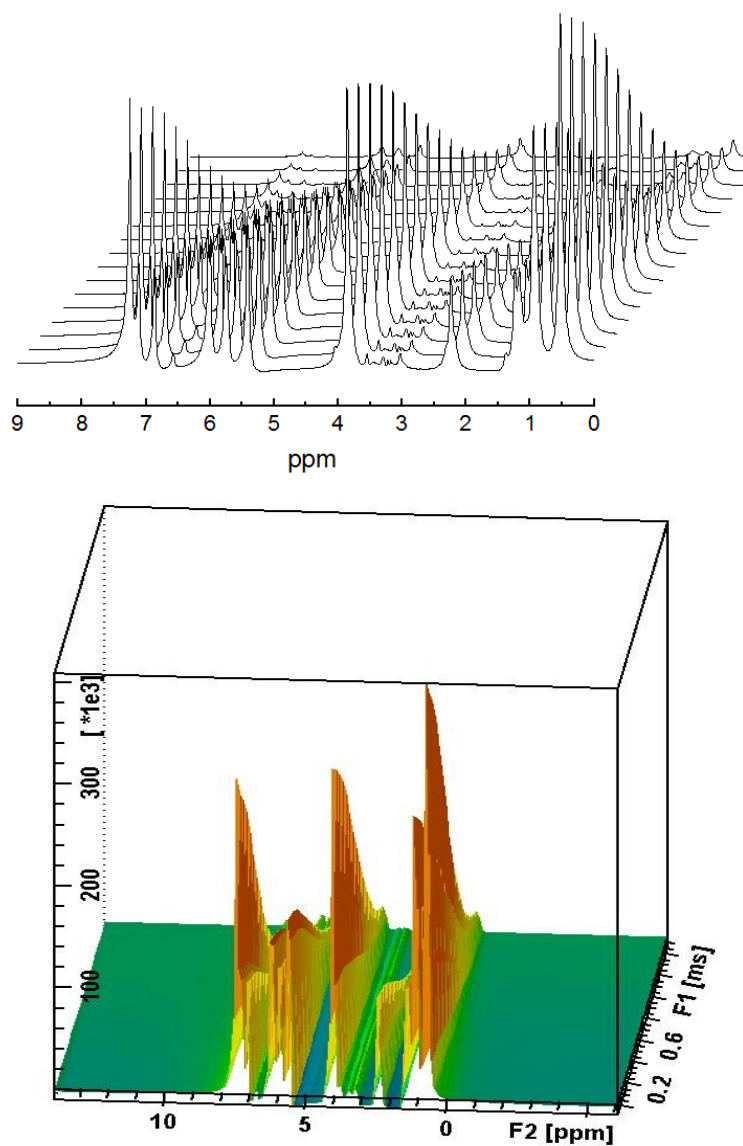


**Figure A4:** Top: Spectra intensity as a function of gradient strength  $g$ . Bottom: The attenuation of intensity in Topspin version. Mixture contains 47.8 % E7.

## A5 Determination of diffusion coefficients for E7 and PDLC

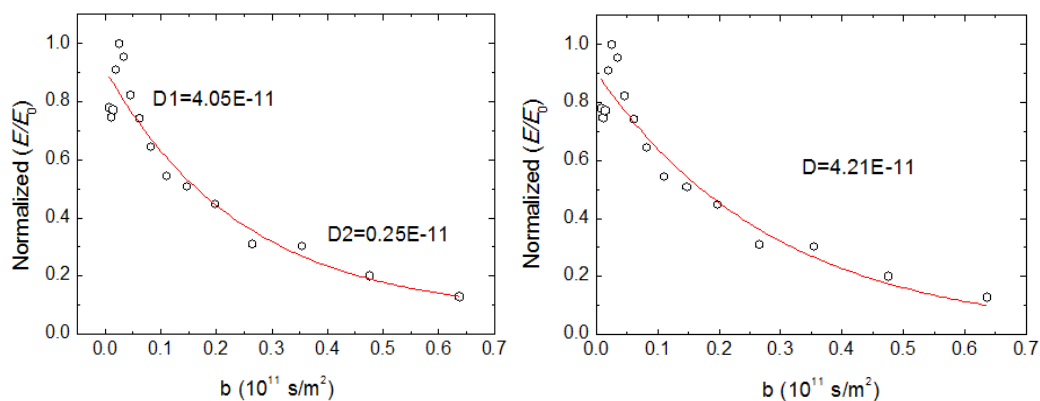


**Figure A5.1:** Diffusion fitting for pure E7 (peak at 7.4 ppm) with full data set using biexponential (left) and exponential (right) decay.

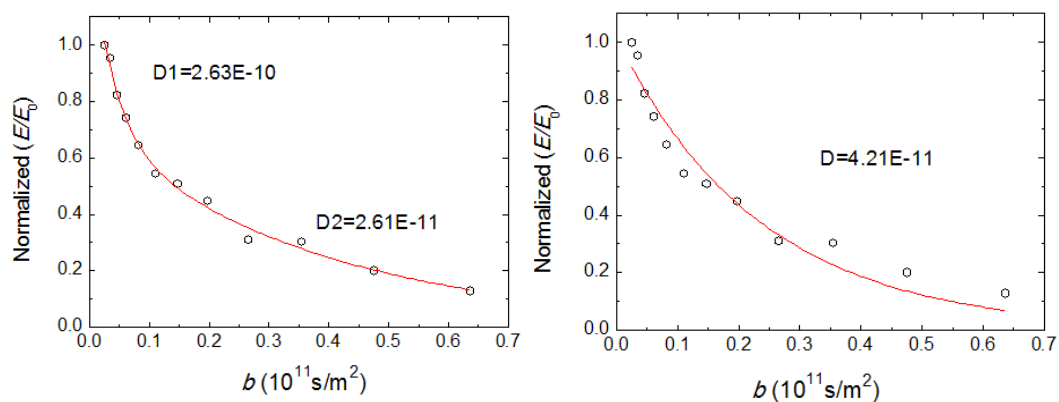


**Figure A5.2:** Diffusion fitting for pure E7 without the first 4 points using biexponential (left) and exponential (right) decay.

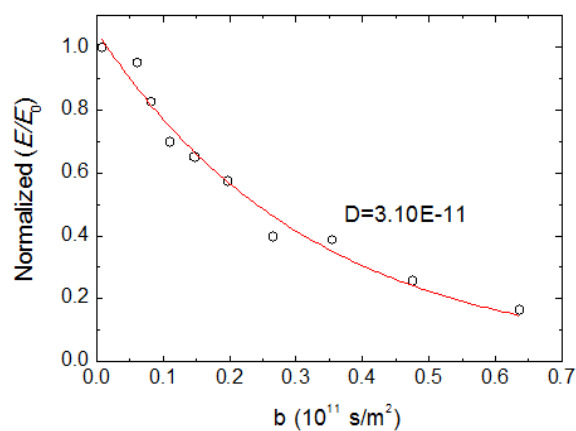


**Figure A5.3:** Diffusion fitting for pure E7 without data from point 2 to 6 by exponential fitting.

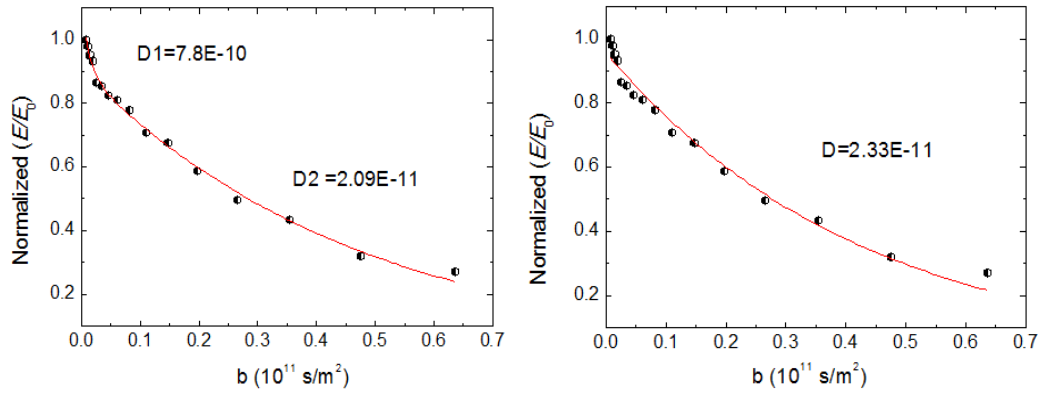


**Figure A5.4:** Diffusion fitting for PDLC (peak at 7.4 ppm) with full data set using biexponential (left) and exponential (right) decay, respectively.

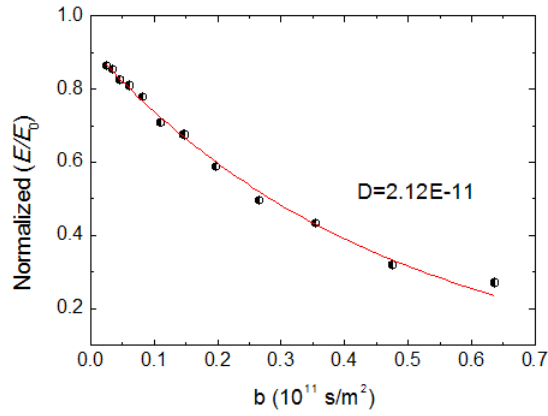


**Figure A5.5:** Diffusion fitting for PDLC without the first 4 points using exponential fitting.

**Table A5:** The diffusion fitting results for E7 and PDLC,  $D$  in units of  $10^{-11} \text{ m}^2/\text{s}$ .

	full data set			without the first 4 points			without point 2-6
	$D_1$	$D_2$	$D$	$D_1$	$D_2$	$D$	$D$
E7	4.05	0.25	4.21	26.3	2.61	4.21	<b>3.10</b>
PDLC	78.0	<b>2.09</b>	2.33	----	----	<b>2.12</b>	----



## A6 Experimental parameters of diffusion experiments

### A6.1 Static diffusion

<b>Probe:</b>	"5 mm MIC BB-1H XYZ-GRD Z3386/0019"
<b>Gradient steps<sup>#</sup>:</b>	1 % to 100 %
<b>Maximum gradient value:</b>	3.0 T/m

#: Given by the file "difflist":

(0.01 0.076 0.142 0.208 0.274 0.34 0.406 0.472 0.538 0.604 0.67 0.736 0.802 0.868 0.934 1)

The pulse sequence used is shown in Fig A6.1 and a ramped gradient was used.

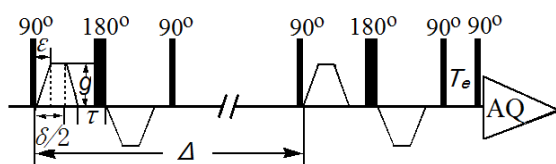


**Figure A6.1:** Ramped BPP-LED pulse sequence.

The signal decay is given by the following equation (cf. eq. (1)-(3)) in

C. S. Johnson, Proc. Nuclear Magn. Reson. Spec. **34**, 203 (1999).

Equation (3) was given by Prof. Daniel Topgaard.

$$M = M_0 e^{-bD} \quad (1)$$

$$b = (\gamma g \delta)^2 t_d \quad (2)$$

$$t_d = \Delta - \frac{\delta}{3} - \frac{\tau}{2} - \frac{\epsilon}{2} - \frac{\epsilon^2}{6\delta} + \frac{\epsilon^3}{15\delta^2} \quad (3)$$

Delay parameters in file "acqus":

**D= (0..63) (s)**

```
0 1 0.0004 0.0006 1e-04 0.09463344 0.0006 0.02032948 0 0.018249 0.018253 0.03
0.00025 0 0 0 1e-04 0 0 0 0.02 0.001 1e-06 0 0 0 0 0.005 0 0 0 0 0 0 0 0 0
0.0005 0.001 0 0 1e-04 0 0 0 0 0 0 0 0 0 0 0 0 0 0 0 0 0 0
```

**P= (0..63) (µs)**

```
12.4 15 30 0 0 0 0 0 0 0 0 0 0 0 200000 1000 220 280 600 2500 0 0 0 0 0 12.4
1000 0 0 0 0 0 0 0 0 0 0 0 0 0 0 0 0 0 0 0 0 0 0 0 0 0 0 0 0 0 0 0 0 0 0 0 0
```

**Table A6.1.1:** Values of parameters for static diffusion.

d2	d3	d4	d5	d6	d22	d42	d43	d46	p1	p2
0.0004	0.0006	1e-04	0.09463344	0.0006	1e-06	0.0005	0.001	1e-04	15	30

$$\Delta = 4d2 + 2d3 + 2d4 + p2 + d22 + 2d6 + 2p1 + d5 + d46 + 2d42 + d43 + 2d22 = 0.10102644 \text{ s}$$

$$\delta = 2(d2 + d3) = 0.002 \text{ s}$$

$$\tau = 2d4 + p2 = 2.3e-4 \text{ s}$$

$$\varepsilon=d_2=0.0004s$$

$$t_d=0.100032507s \text{ (eq.3)}$$

$$b=(\gamma g \delta)^2 \times t_d = (2.675222099 \times 10^8 \times 0.002)^2 \times 0.100032507 \times g^2 = 28636558977 \times g^2$$

**Table A6.1.2:** The gradient strength  $g$  and parameters  $b$  for static diffusion.

G=diff-ramp file"difflist"	$g=\text{diff-ramp} \times g(\text{max})$ $g=G \times 3 \times 1$	$b=(\gamma \delta)^2 \times t_d \times g^2$ $=28636558977 \times g^2$
0.01	0.03	25772903.08
0.076	0.228	1488642882
0.142	0.426	5196848177
0.208	0.624	11150388788
0.274	0.822	19349264716
0.34	1.02	29793475960
0.406	1.218	42483022520
0.472	1.416	57417904396
0.538	1.614	74598121589
0.604	1.812	94023674098
0.67	2.01	1.15695E+11
0.736	2.208	1.39611E+11
0.802	2.406	1.65772E+11
0.868	2.604	1.94179E+11
0.934	2.802	2.24831E+11
1	3	2.57729E+11

**Table A6.1.3:** Fitting results for the diffusion coefficients  $D$  for static measurements.

E7 (wt %)	$D(10^{-11} \text{ m}^2/\text{s})$ E7	$D(10^{-11} \text{ m}^2/\text{s})$ TMPTA
0	---	0.820
10.7	1.13	0.829
18.7	1.18	0.851
28.5	1.31	0.880
40.3	1.40	0.908
47.8	1.50	0.936
57.2	1.62	0.995

## A6.2 MAS diffusion

<b>Probe:</b>	"4 mm HRMAS 1H-13C/31P Z-GRD B3175/0415"
<b>Gradient steps<sup>#</sup>:</b>	10 % to 90 %
<b>Maximum gradient value:</b>	0.59 T/m×0.9 <sup>##</sup>

#: Given by the file "difflist":

```
(0.1 0.115775 0.134039 0.155185 0.179666 0.208008 0.240823 0.278813 0.322797 0.373719
0.432675 0.500931 0.579955 0.671445 0.777368 0.9)
```

##: The maximum gradient used in the pulse program corresponds to 90 % of the actually possible gradient value. This is specified by "GPZ6" in the file "ACQUS".

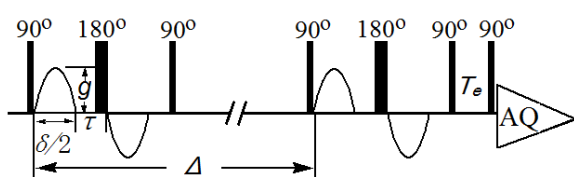


**Figure A6.2:** Sine-shaped BPP-LED pulse sequence for diffusion measurement.

$$b = \left( \frac{2\delta g \gamma}{\pi} \right)^2 \left( \Delta - \frac{\tau}{2} - \frac{\delta}{3} - P\pi \right) \quad (4)$$

The pulse sequence used is shown in Fig A6.2 and the parameter  $b$  is given by the following equation (4) (cf. E.E. Romanova et al., Journal of Magnetic Resonance 196 (2009) 110–114)

Delay parameters:

##SD= (0..63) (s)

```
3e-06 3 2e-05 3e-06 2e-05 0 1.5e-05 3e-06 0 0.06 0 0 0 0 0 0 0.001 0 0 0 0.1 0.01 1e-
06 0 0 1e-06 1e-06 1e-06 1e-06 1e-06 0 0 0 0 0 0 0 0 0 0 0 0 0 0 0 0 0 0 0 0
0 0 0 0 0 0 0 0
```

P values:

P= (0..63) (μs)

```
10 5.75 11.5 12 24 0 0 0 0 0 0 0 0 0 0 0 200000 1000 2500 0 1000 2500 0 0 0 0 0 0 10
1000 0 5000 0 0 0 0 0 0 0 0 0 0 0 0 0 0 0 0 0 0 0 0 0 0 0 0 0 0 0 0
```

**Table A6.2.1:** Values of parameters for MAS diffusion.

d16	d20	p2	p30
0.001	0.1	30	5000

$\Delta = d20 = 0.1 \text{ s}$

$P\pi = p2 = 1.15 \times 10^{-5} \text{ s}$

$\delta = p30 = 0.005 \text{ s}$

$\tau = d16 = 0.001 \text{ s}$

$t_d = \Delta - \tau/2 - 2\delta/3 - P\pi = 0.096155167 \text{ s}$

$b = (4\gamma g \delta / \pi)^2 \times t_d = (4\gamma \delta / \pi)^2 \times t_d \times g^2 = 278902589295.16 \times g^2$

**Table A6.2.2:** The gradient strength  $g$  and parameters  $b$  for MAS diffusion.

$G$ =diff-ramp file"difflist"	$g$ =diff-ramp $\times G$ (max) $g=G\times 0.59\times 0.9$	$b=(4\gamma\delta/\pi)^2\times t d\times g^2$ $=278902589295.16\times g^2$
0.1	0.0531	786396529.8
0.115775	0.061476525	1054074162
0.134039	0.071174709	1412875670
0.155185	0.082403235	1893830338
0.179666	0.095402646	2538477897
0.208008	0.110452248	3402527664
0.240823	0.127877013	4560763085
0.278813	0.148049703	6113186244
0.322797	0.171405207	8194086950
0.373719	0.198444789	10983277198
0.432675	0.229750425	14721945074
0.500931	0.265994361	19733194924
0.579955	0.307956105	26450274432
0.671445	0.356537295	35453774384
0.777368	0.412782408	47522021519
0.9	0.4779	63698118914

**Table A6.2.3:** Fitting results for the diffusion coefficients  $D$  for MAS measurements.

	E7	PDLCs	(P)TMPTA
$D(10^{-11}\text{m}^2/\text{s})$	3.10	2.09	0.68

## A7 Diffusion pulse programs

### A7.1 Ramped BPP-LED sequence used for static diffusion measurements

```
# 1 "/opt/topspin2/exp/stan/nmr/lists/pp/user/DT_ledbpgste"
;DT_ledbpgste
;AVII-500 (20101018)

;CLASS=DT
;SDIM=2
;$TYPE=diff
;$SUBTYPE=stimulated echo
;SCOMMENT=

;$OWNER=nmrslu
# 1 "/opt/topspin2/exp/stan/nmr/lists/pp/Avance.incl" 1
;Avance2.incl
; for 1
;avance-version (06/02/20)
;$CLASS=HighRes Incl
;SCOMMENT=

;$Id: Avance.incl,v 1.2 2006/09/13 12:12:04 chjo Exp $
# 11 "/opt/topspin2/exp/stan/nmr/lists/pp/user/DT_ledbpgste" 2

# 1 "/opt/topspin2/exp/stan/nmr/lists/pp/Grad.incl" 1
;Grad2.incl - include file for Gradient Spectroscopy
; for 1

;avance-version (07/01/17)

;$CLASS=HighRes Incl
;SCOMMENT=

define list<gradient> EA=<EA>

;$Id: Grad2.incl,v 1.12 2007/01/22 14:22:35 ber Exp $
# 12 "/opt/topspin2/exp/stan/nmr/lists/pp/user/DT_ledbpgste" 2

"d11 = 30m"
"d22 = 1u"
"d21 = 1m"
"p2 = 2*p1"
```

```

define list <gradient> ru=<rampUp.100>
define list <gradient> rd=<rampDown.100>
define list <gradient> dr=<diff_ramp>

# 1 "mc_line 23 file /opt/topspin2/exp/stan/nmr/lists/pp/user/DT_ledbpggste dc-measurement
inserted automatically"
    dccorr
# 23 "/opt/topspin2/exp/stan/nmr/lists/pp/user/DT_ledbpggste"
1 ze
2 d1

p1 ph1

d6 setnmr0|34|32|33 ctrlgrad 0
d2 grad{ ru(cnst1,100)*dr | ru(cnst2,100)*dr | ru(cnst3,100)*dr }
d3 grad{ dr(cnst1) | dr(cnst2) | dr(cnst3) }
d2 grad{ rd(cnst1,100)*dr | rd(cnst2,100)*dr | rd(cnst3,100)*dr }
d4
    p2 ph1
d4
d2 grad{ ru(-1*cnst1,100)*dr | ru(-1*cnst2,100)*dr | ru(-1*cnst3,100)*dr }
d3 grad{ dr(-1*cnst1) | dr(-1*cnst2) | dr(-1*cnst3) }
d2 grad{ rd(-1*cnst1,100)*dr | rd(-1*cnst2,100)*dr | rd(-1*cnst3,100)*dr }
d22 groff
d6 setnmr0^34^32^33 ctrlgrad 7

p1 ph2

if (I11) {
    ; if spoiler in use
    d46 setnmr0|34|32|33 ctrlgrad 0
    d42 grad{ ru(cnst4,100) | ru(cnst5,100) | ru(cnst6,100) }
    d43 grad{ (cnst4) | (cnst5) | (cnst6) }
    d42 grad{ rd(cnst4,100) | rd(cnst5,100) | rd(cnst6,100) }
    d22 groff
    d22 setnmr0^34^32^33 ctrlgrad 7
}

d5

p1 ph3

d6 setnmr0|34|32|33 ctrlgrad 0
d2 grad{ ru(cnst1,100)*dr | ru(cnst2,100)*dr | ru(cnst3,100)*dr }
d3 grad{ dr(cnst1) | dr(cnst2) | dr(cnst3) }

```

```

d2 grad{ rd(const1,100)*dr | rd(const2,100)*dr | rd(const3,100)*dr }
d4
    p2 ph1
d4
d2 grad{ ru(-1*const1,100)*dr | ru(-1*const2,100)*dr | ru(-1*const3,100)*dr }
d3 grad{ dr(-1*const1) | dr(-1*const2) | dr(-1*const3) }
d2 grad{ rd(-1*const1,100)*dr | rd(-1*const2,100)*dr | rd(-1*const3,100)*dr }
d22 groff
d6 setnmr0^34^32^33 ctrlgrad 7

```

p1 ph4

```

if (l11) {
    ; if spoiler in use
    d46 setnmr0|34|32|33 ctrlgrad 0
    d42 grad{ ru(const7,100) | ru(const8,100) | ru(const9,100) }
    d43 grad{ (const7) | (const8) | (const9) }
    d42 grad{ rd(const7,100) | rd(const8,100) | rd(const9,100) }
    d22 groff
    d22 setnmr0^34^32^33 ctrlgrad 7
}

```

d7

p1 ph5

```

go=2 ph31
d11 wr #0 if #0 igrad dr
lo to 1 times td1
exit

```

```

ph1= 0
ph2= 0 0 2 2
ph3= 0 0 0 0 2 2 2 2 1 1 1 1 3 3 3 3
ph4= 0 2 0 2 2 0 2 0 1 3 1 3 3 1 3 1
ph5= 0 0 0 0 2 2 2 2 1 1 1 1 3 3 3 3
ph31=0 2 2 0 2 0 0 2 3 1 1 3 1 3 3 1

```

```

;cnst3: diffusion gradient
;cnst4: spoiler gradient

```

## A7.2 Sine-shaped BPP-LED pulse sequence used for MAS diffusion measurements

```
# 1 "/opt/topspin2/exp/stan/nmr/lists/pp/user/DT_ledbpgp2s"
;ledbpgp2s
;avance-version (03/04/24)
;2D sequence for diffusion measurement using stimulated
; echo and LED
;using bipolar gradient pulses for diffusion
;using 2 spoil gradients
;D. Wu, A. Chen & C.S. Johnson Jr.,
; J. Magn. Reson. A 115, 260-264 (1995).

;$CLASS=DT
;$DIM=2D
;$TYPE=
;$SUBTYPE=
;$COMMENT=

;$OWNER=nmrstu
# 1 "/opt/topspin2/exp/stan/nmr/lists/pp/Avance.incl" 1
;Avance2.incl
; for 1
;avance-version (06/02/20)
;$CLASS=HighRes Incl
;$COMMENT=
;$Id: Avance.incl,v 1.2 2006/09/13 12:12:04 chjo Exp $
# 19 "/opt/topspin2/exp/stan/nmr/lists/pp/user/DT_ledbpgp2s" 2

# 1 "/opt/topspin2/exp/stan/nmr/lists/pp/Grad.incl" 1
;Grad2.incl - include file for Gradient Spectroscopy
; for 1
;avance-version (07/01/17)
;$CLASS=HighRes Incl
;$COMMENT=

define list<gradient> EA=<EA>

;$Id: Grad2.incl,v 1.12 2007/01/22 14:22:35 ber Exp $
# 20 "/opt/topspin2/exp/stan/nmr/lists/pp/user/DT_ledbpgp2s" 2

# 1 "/opt/topspin2/exp/stan/nmr/lists/pp/Delay.incl" 1
;Delay.incl - include file for commonly used delays
;version 00/02/07
;$CLASS=HighRes Incl
```



```
;$COMMENT=
```

```
;general delays
```

```
define delay DELTA  
define delay DELTA1  
define delay DELTA2  
define delay DELTA3  
define delay DELTA4  
define delay DELTA5  
define delay DELTA6  
define delay DELTA7  
define delay DELTA8
```

```
define delay TAU  
define delay TAU1  
define delay TAU2  
define delay TAU3  
define delay TAU4  
define delay TAU5
```

```
;delays for centering pulses
```

```
define delay CEN_HN1  
define delay CEN_HN2  
define delay CEN_HN3  
define delay CEN_HC1  
define delay CEN_HC2  
define delay CEN_HC3  
define delay CEN_HC4  
define delay CEN_HP1  
define delay CEN_HP2  
define delay CEN_CN1  
define delay CEN_CN2  
define delay CEN_CN3  
define delay CEN_CN4  
define delay CEN_CP1  
define delay CEN_CP2
```

```
;loop counters
```

```
define loopcounter COUNTER  
define loopcounter SCALEF  
define loopcounter FACTOR1
```

```

define loopcounter FACTOR2
define loopcounter FACTOR3

;$Id: Delay.incl,v 1.12 2005/11/10 12:16:58 ber Exp $
# 21 "/opt/topspin2/exp/stan/nmr/lists/pp/user/DT_ledbpgp2s" 2

define list<gradient> diff=<diff_ramp>

"p2=p1*2"
"DELTA1=d20-p1*2-p2-p30*2-d16*2-p19-d16"
"DELTA2=d21-p19-d16-4u"

# 1 "mc_line 34 file /opt/topspin2/exp/stan/nmr/lists/pp/user/DT_ledbpgp2s expanding definition
part of mc command before ze"
define delay MCWRK
define delay MCREST
"MCWRK = 0.500000*d1"
"MCREST = d1 - d1"
  dccorr
# 34 "/opt/topspin2/exp/stan/nmr/lists/pp/user/DT_ledbpgp2s"
1 ze
# 1 "mc_line 34 file /opt/topspin2/exp/stan/nmr/lists/pp/user/DT_ledbpgp2s expanding definition
of mc command after ze"
# 35 "/opt/topspin2/exp/stan/nmr/lists/pp/user/DT_ledbpgp2s"
# 1 "mc_line 35 file /opt/topspin2/exp/stan/nmr/lists/pp/user/DT_ledbpgp2s expanding start label
for mc command"
2 MCWRK
LBLF1, MCWRK
  MCREST
# 36 "/opt/topspin2/exp/stan/nmr/lists/pp/user/DT_ledbpgp2s"
50u setnmr0|34|32|33 ctrlgrad 0
p1 ph1
p30:gp6*diff
d16
p2 ph1
p30:gp6*-1*diff
d16
p1 ph2
p19:gp7
d16
DELTA1
p1 ph3
p30:gp6*diff
d16

```

```

p2 ph1
p30:gp6*-1*diff
d16
p1 ph4
p19:gp8
d16
DELTA2
4u setnmr0^34^32^33 ctrlgrad 7
p1 ph5
go=2 ph31
# 1 "mc_line 60 file /opt/topspin2/exp/stan/nmr/lists/pp/user/DT_ledbpgp2s expanding mc
command in line"
MCWRK wr #0 if #0 zd igrad diff
lo to LBLF1 times td1
MCWRK
# 61 "/opt/topspin2/exp/stan/nmr/lists/pp/user/DT_ledbpgp2s"
exit

```

```

ph1= 0
ph2= 0 0 2 2
ph3= 0 0 0 0 2 2 2 2 1 1 1 1 3 3 3 3
ph4= 0 2 0 2 2 0 2 0 1 3 1 3 3 1 3 1
ph5= 0 0 0 0 2 2 2 2 1 1 1 1 3 3 3 3
ph31=0 2 2 0 2 0 0 2 3 1 1 3 1 3 3 1

```

```

;p11 : f1 channel - power level for pulse (default)
;p1 : f1 channel - 90 degree high power pulse
;p2 : f1 channel - 180 degree high power pulse
;p19: gradient pulse 2 (spoil gradient)
;p30: gradient pulse (little DELTA * 0.5)
;d1 : relaxation delay; 1-5 * T1
;d16: delay for gradient recovery
;d20: diffusion time (big DELTA)
;d21: eddy current delay (Te) [5 ms]
;NS: 8 * n
;DS: 4 * m
;td1: number of experiments
;FnMODE: QF
; use xf2 and DOSY processing

;use gradient ratio: gp 6 : gp 7 : gp 8
; 100 : -17.13 : -13.17

;for z-only gradients:

```

```
;gpz6: 100%  
;gpz7: -17.13% (spoil)  
;gpz8: -13.17% (spoil)
```

```
;use gradient files:  
;gpnam6: SINE.100  
;gpnam7: SINE.100  
;gpnam8: SINE.100
```

```
;use AU-program dosy to calculate gradient ramp-file Difframp  
;$Id: ledbpp2s,v 1.5 2005/11/10 12:17:00 ber Exp $
```

## A8 Relaxation in the rotating frame

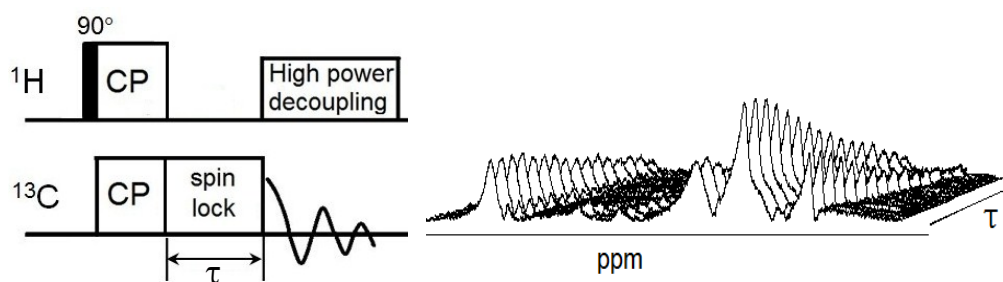


**Figure A8.1:** Pulse sequence for  $T_{1\rho,C}$  measurements by varying the spin lock time after cross polarization. The right part shows the spectral intensity as a function of  $\tau$ .

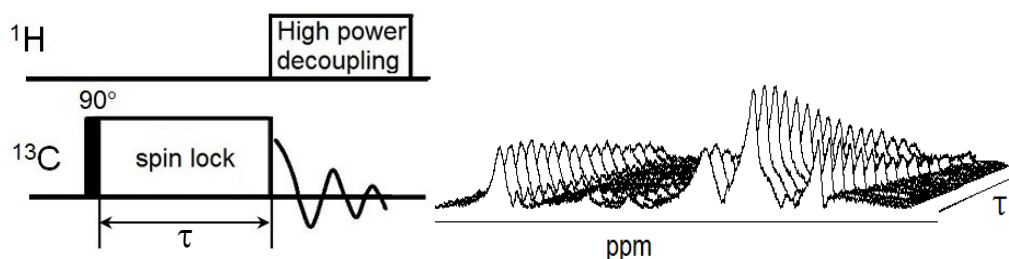


**Figure A8.2:** Pulse sequence for measuring  $T_{1\rho,C}$  of TMPTA by exciting the  $^{13}\text{C}$  spin directly. The right part shows the spectral intensity as a function of  $\tau$ .

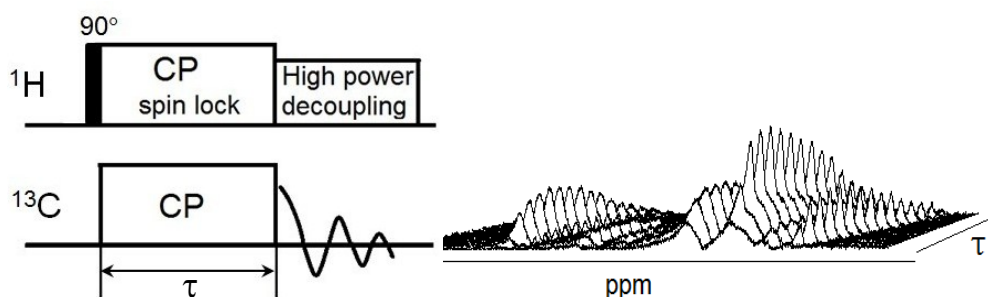


**Figure A8.3:** Pulse sequence for  $T_{1\rho,H}$  measurements by varying the contact time. The right part shows the spectral intensity as a function of  $\tau$ .

## List of Symbols

NMR	Nuclear magnetic resonance
$^1\text{H}$ NMR	Proton NMR
$^{13}\text{C}$ NMR	Carbon NMR
PPM	Parts per million
MAS	Magic angle spinning
CP	Cross polarization
PFG	Pulsed field gradient
STE	Stimulated echo
PGSE	Pulsed gradient spin echo
BPP-LED	Bipolar pair pulse longitudinal eddy-current delay
ODF	Order director fluctuations
PIPS	Polymerization-induced phase separation
SIPS	Solvent-induced phase separation
TIPS	Thermally-induced phase separation
E7	Mixture of four liquid crystals
5CB	4-cyano-4'-pentylbiphenyl
TMPTA	Trimethylolpropane triacrylate
TMS	Tetramethylsilane
LC	Liquid crystal
PDLC	Polymer-dispersed liquid crystal
HPDLC	Holographic polymer-dispersed liquid crystal
$B_0$	External magnetic field
$B_1$	Spin lock field or excitation field
$D$	Diffusion coefficient
$\delta$	Gradient duration
$\Delta$	Diffusion time
$t_d$	Effective diffusion time
$A_g$	Area of the gradient pulse or pulse pair
$\Delta\nu$	Spectra splitting
$\omega$	Larmor frequency
$f$	Friction coefficient
$\gamma$	Gyromagnetic ratio
$\sigma$	Chemical shielding tensor
$\beta$	Magic angle
$g$	Gradient strength
$h$	Planck constant
$\eta$	Viscosity coefficient
$k_B$	Boltzmann constant
$\lambda$	Wavelength (nm)
rf	Radio frequency
$R_1$	Spin-lattice or longitudinal relaxation rate
$R_2$	Spin-spin or transverse relaxation rate
$R_h$	Hydrodynamic radius
$\tau$	Delay between pulses
$T$	Temperature
$T_{NI}$	Nematic-to-isotropic phase-transition temperature

$T_1$	Spin-lattice or longitudinal relaxation time
$T_{1\rho}$	Spin-lattice relaxation time in the rotating frame
$T_{1\rho,C}$	Spin-lattice relaxation time in the rotating frame of carbon
$T_{1\rho,H}$	Spin-lattice relaxation time in the rotating frame of proton
$T_2$	Spin-spin or transverse relaxation time
$T_e$	Eddy current delay period
S	Nematic order parameter

## References

- [1] F. Reinitzer, *Monatsh. Chem.* **1888**, *9*, 421.
- [2] O. Lehmann, *Flüssige Kristalle*, Wilhelm Engelmann, Leipzig, **1904**.
- [3] T. J. Sluckin, D. A. Dunmur, H. Stegemeyer, *Crystals That Flow: Classic Papers in the History of Liquid Crystals*, Taylor & Francis, London, **2004**.
- [4] P. G. d. Gennes, J. Prost, *Physics of Liquid Crystals*, Oxford University Press, Oxford, **1995**.
- [5] S. Chandrasekhar, *Liquid Crystals*, Cambridge University Press, Cambridge **1992**.
- [6] E. B. Priestley, P. J. Wojtowicz, P. S. (Eds.), *Introduction to Liquid Crystals*, Plenum Press, New York, **1974**.
- [7] G. R. Luckhurst, G. W. G. (Eds.), *The Molecular Physics of Liquid Crystals*, Academic Press, London **1979**.
- [8] L. Vicari, *Optical applications of liquid crystals*, Taylor & Francis, London, **2003**.
- [9] T. Sonehara, in *Optical applications of liquid crystals* (Ed.: L. Vicari), Inst. of Phys, **2003**, pp. 245.
- [10] J. L. Ferguson, in *Proceedings of the International Symposium Digest of Technical Papers, Vol. 16*, San Jose, Calif, USA, **1985**, pp. 68.
- [11] J. W. Doane, N. A. Vaz, B.-G. Wu, a. S. Zumer, *Appl. Phys. Lett.* **1986**, *48*, 269.
- [12] J. L. Fergason, U. S. Patent 4 435047, U.S, **1984**.
- [13] J. D. Bernal, I. Fankuchen, *J. Gen. Physiol.* **1941**, *25*, 111.
- [14] G. E. Volovik, O. D. Lavrentovich, *Sov. Phys. JETP.* **1983**, *58*, 1159.
- [15] R. D. Williams, *J. Phys. A: Math. Gen.* **1986**, *19*, 3211.
- [16] P. Drzaic, *Liq. Cryst.* **2006**, *33*, 1281.
- [17] D. A. Higgins, J. E. Hall, A. Xie, *Acc. Chem. Res.* **2005**, *38*, 137.
- [18] R. A. M. Hikmet, H. Kemperman, *Nature* **1998**, *392*, 476.
- [19] Y. G. Marinov, G. B. Hadjichristov, A. G. Petrov, *Opt. Laser Eng.* **2010**, *48*, 1161.
- [20] P. L. Almeida, G. Lavareda, C. N. D. Carvalho, A. Amaral, M. H. Godinho, M. T. Cidade, J. L. Figueirinhas, *Liq. Cryst.* **2002**, *29*, 475.
- [21] F. Bloisi, L. Vicari, in *Optical applications of liquid crystals* (Ed.: L. Vicari), Inst. of Phys, **2003**, pp. 148.
- [22] J. L. West, *ACS Symp. Ser.* **1990**, *435*, 475.
- [23] R. Caputo, L. De Sio, A. Veltri, A. V. Sukhov, N. V. Tabiryan, C. P. Umeton, in *Advances in Composite Materials - Analysis of Natural and Man-Made Materials* (Ed.: P. Tesinova), InTech, **2011**, pp. 93.
- [24] T. J. Bunning, L. V. Natarajan, V. P. Tondiglia, R. L. Sutherland, *Annu. Rev. Mater. Sci.* **2000**, *30*, 83.
- [25] M. Mucha, *Prog. Polym. Sci.* **2003**, *28*, 837.
- [26] L. Bouteiller, P. LeBarny, *Liq. Cryst.* **1996**, *21*, 157.



- [27] P. S. Drazic, *Liquid Crystal Dispersions*, World Scientific, Singapore, **1995**.
- [28] G. S. Iannacchione, G. P. Crawford, S. Zumer, J. W. Doane, D. Finotello, *Phys. Rev. Lett.* **1993**, *71*, 2595.
- [29] S. Kralj, G. Lahajnar, A. Zidansek, N. Vrbancic-Kopac, M. Vilfan, R. Blinc, M. Kosec, *Phys. Rev. E* **1993**, *48*, 340.
- [30] G. S. Iannacchione, G. P. Crawford, S. Qian, J. W. Doane, D. Finotello, S. Zumer, *Phys. Rev. E* **1996**, *53*, 2402.
- [31] T. Jin, D. Finotello, *Phys. Rev. Lett.* **2001**, *86*, 818.
- [32] M. Vilfan, B. Zalar, A. K. Fontecchio, M. Vilfan, M. J. Escuti, G. P. Crawford, S. Zumer, *Phys. Rev. E* **2002**, *66*, 021710.
- [33] L. Beguin, J. W. Emsley, M. Lelli, A. Lesage, G. R. Luckhurst, B. A. Timimi, H. Zimmermann, *J. Phys. Chem. B* **2012**, *116*, 7940.
- [34] T. Väänänen, J. Tokisaari, J. Lounila, *J. Magn. Reson.* **1982**, *49*, 73.
- [35] T. Väänänen, J. Jokisaari, A. Kääriäinen, J. Lounila, *J. Mol. Struct.* **1983**, *102*, 175.
- [36] C. S. Yannoni, E. B. Whipple, *J. Chem. Phys.* **1967**, *47*, 2508.
- [37] B. M. Fung, *Prog. Nucl. Magn. Reson. Spectrosc.* **2002**, *41*, 171.
- [38] B. M. Fung, *J. Magn. Reson.* **1983**, *55*, 475.
- [39] A. Cogne, J.-B. Robert, L. Wiesenfeld, *Chem. Phys. Lett.* **1978**, *57*, 627.
- [40] P. Tallavaara, V. V. Telkki, J. Jokisaari, *J. Phys. Chem.* **2006**, *110*, 21603.
- [41] M. Vilfan, T. Apih, A. Gregorovic, B. Zalar, G. Lahajnar, S. Zumer, G. Hinze, R. Böhmer, G. Althoff, *Magn. Reson. Imaging* **2001**, *19*, 433.
- [42] E. Anoardo, F. Grinberg, M. Vilfan, R. Kimmich, *Chem. Phys.* **2004**, *297*, 99.
- [43] N. Bloembergen, E. M. Purcell, R. V. Pound, *Phys. Rev.* **1948**, *73*, 679.
- [44] I. Solomon, *Phys. Rev.* **1955**, *99*, 559.
- [45] F. Bloch, *Phys. Rev.* **1957**, *105*, 1206.
- [46] F. Bloch, *Phys. Rev.* **1956**, *102*, 104.
- [47] K. Tomita, *Prog. Theor. Phys.* **1958**, *19*, 541.
- [48] C. W. Cross, B. M. Fung, *J. Chem. Phys.* **1992**, *96*, 7086.
- [49] F. Grinberg, R. Kimmich, S. Stapf, *Magn. Reson. Imaging* **1998**, *16*, 635.
- [50] D. M. Sousa, G. D. Marques, P. J. Sebastiao, A. C. Ribeiro, *Rev. Sci. Instrum.* **2003**, *74*, 4521.
- [51] R. Kimmich, E. Anoardo, *Prog. Nucl. Magn. Reson. Spectrosc.* **2004**, *44*, 257.
- [52] D. F. Brougham, A. J. Horsewill, H. P. Trommsdorff, *Chem. Phys.* **1999**, *243*, 189.
- [53] A. Aluculesei, F. V. Chavez, C. Cruz, P. J. Sebastiao, N. G. Nagaveni, V. Prasad, R. Y. Dong, *J. Phys. Chem. B* **2012**, *116*, 9556.
- [54] R. Blinc, D. L. Hogenboom, D. E. O'Reilly, E. M. Peterson, *Phys. Rev. Lett.* **1969**, *23*, 969.
- [55] J. W. Doane, J. J. Visintainer, *Phys. Rev. Lett.* **1969**, *23*, 1421.
- [56] R. Y. Dong, C. F. Schwerdtfeger, *Solid State Commun.* **1970**, *8*, 707.
- [57] C. E. Tarr, M. A. Nickerson, C. W. Smith, *Appl. Phys. Lett.* **1970**, *17*, 318.
- [58] F. B. Michael, *J. Chem. Phys.* **1982**, *77*, 1576.
- [59] R. L. Sutherland, L. V. Natarajan, V. P. Tondiglia, a. T. J. Bunning, *Chem.*

- Mater.* **1993**, 5, 1533.
- [60] E. O. Stejskal, J. E. Tanner, *J. Chem. Phys.* **1965**, 42, 288.
- [61] R. Kimmich, *NMR: Tomography, Diffusometry, Relaxometry*, Springer Verlag, Berlin, **1997**.
- [62] M. J. Duer, *Solid-State NMR: Spectroscopy, Principles, and Applications*, **2005**.
- [63] M. H. Levitt, *Spin Dynamics: Basics of Nuclear Magnetic Resonance*, Wiley and Sons Ltd., **2002**.
- [64] P. T. Callaghan, *Principles of Nuclear Magnetic Resonance Microscopy*, Oxford Univ. Press, **1991**.
- [65] E. D. Becker, *High Resolution NMR Theory and Chemical Applications*, Academic press, **2000**.
- [66] R. Y. Dong, Editor-in-Chief: J. Lindon, in *Encyclopedia of Spectroscopy and Spectrometry (Second Edition)*, Academic Press, Oxford, **1999**, pp. 1855.
- [67] F. A. Bovey, P. E. Mirau, *NMR of Polymers*, Academic press, **1996**.
- [68] E. O. Stejskal, J. D. Memory, *High Resolution NMR in the Solid State, Fundamentals of CP/MAS*, Oxford University Press, **1994**.
- [69] J. Sanders, B. Hunter, *Modern NMR Spectroscopy, A Guide for Chemists*, Oxford Univ. Press, **1993**.
- [70] J. W. Hennel, J. Klinowski, *Fundamentals of Nuclear Magnetic Resonance*, Longman Scientific & Technical London, **1993**.
- [71] R. Ernst, *Principles of NMR in One and Two Dimensions*, Oxford Univ. Press, **1992**.
- [72] W. Kemp, *NMR in Chemistry: a Multinuclear Introduction*, in *McMillan education LTD*, **1986**.
- [73] A. Abragam, *The Principles of Nuclear Magnetism*, Clarendon Press, Oxford, **1961**.
- [74] A. Rahman, *Nuclear Magnetic Resonance: Basic Principles*, Springer Verlag, **1987**.
- [75] G. E. Pake, *J. Chem. Phys.* **1948**, 16, 327.
- [76] I. J. Lowe, *Phys. Rev. Lett.* **1959**, 2, 285.
- [77] E. R. Andrew, A. Bradbury, R. G. Eades, *Nature* **1958**, 182, 1659.
- [78] W. H. Jacek, J. Klinowski, *Magic Angle Spinning: A Historical Perspective*, in *Jacek Klinowski, New Techniques in Solid-State NMR*, Springer, **2005**.
- [79] S. R. Hartmann, E. L. Hahn, *Phys. Rev.* **1962**, 128, 2042.
- [80] A. Abragam, W. G. Proctor, *Phys. Rev.* **1958**, 109, 1441.
- [81] A. Pines, M. G. Gibby, J. S. Waugh, *J. Chem. Phys.* **1973**, 59, 569.
- [82] W. Kolodziejski, J. Klinowski, *Chem. Rev.* **2002**, 102, 613.
- [83] T. Tanaka, *Experimental Methods in Polymer Science*, Academic Press, **1997**.
- [84] <http://www.chem.wisc.edu/areas/reich/nmr/08-tech-01-relax.htm>, relaxation.
- [85] R. E. Taylor, *Concepts Magn. Reson.* **2004**, 22A, 37.
- [86] J. Perez Quinones, R. Szopko, C. Schmidt, C. Peniche Covas, *Carbohydr. Polym.* **2011**, 84, 858.
- [87] I. Wawer, J. Nartowska, A. A. Cichowlas, *Solid State Nucl. Magn. Reson.*

- 2001**, 20, 35.
- [88] F. M. Bayer, M. Tang, R. Michels, C. Schmidt, K. Huber, *Langmuir* **2011**, 27, 12851.
- [89] G. W. Gray, K. J. Harrison, J. A. Nash, *Electron. Lett.* **1973**, 9, 130.
- [90] A. Redler, *Herstellung und Untersuchung polymer-eingebetteter Flüssigkristallssysteme mit Hilfe der Holografie*, PhD thesis, University Paderborn **2011**.
- [91] O. P. Laszlo, in *Prog. Nucl. Magn. Reson. Spectrosc.*, Vol. 3 (Ed.: F. F. J.W. Emsley, L.H. Sutcliffe), Pergamon Press, Oxford, **1967**, pp. 231.
- [92] A. D. Buckingham, T. Schaefer, W. G. Schneider, *J. Chem. Phys.* **1960**, 32, 1227.
- [93] W. G. Schneider, *J. Phys. Chem.* **1962**, 66, 2653.
- [94] S. Kara-Slimane, U. Maschke, F. Benmouna, M. Bacquet, F. Roussel, J.-M. Buisine, X. Coqueret, M. Benmouna, *Eur. Polym. J.* **2002**, 38, 461.
- [95] A. Redler, A. Hoischen, H. Kitzerow, *Mol. Cryst. Liq. Cryst.* **2011**, 547, 97/[1787].
- [96] J. N. Maki, N. M. Loening, in *Modern Nuclear Magnetic Resonance in Undergraduate Education* (Eds.: D. Rovnyak, R. A. Stockland, S. P. Lee), American Chemical Society Books, Washington, DC, **2007**.
- [97] F. Kleinschmidt, *Anomalous Diffusion in Anisotropic Media*, PhD thesis, University Freiburg, **2005**.
- [98] R. Szopko, *Investigation of dimensional and structural properties of dye aggregates*, PhD thesis, University Paderborn, **2009**.
- [99] S. V. Dvinskikh, I. Furo, *Russ. Chem. Rev.* **2006**, 75, 497.
- [100] E. Stejskal, *J. Chem. Phys.* **1965**, 43, 3597.
- [101] C. S. Johnson, *Prog. Nucl. Magn. Reson. Spectrosc.* **1999**, 34, 203.
- [102] W. S. Price, P. W. Kuchel, *J. Magn. Reson.* **1991**, 94, 133.
- [103] S. Viel, F. Ziarelli, S. Caldarelli, *Proc. Natl. Acad. Sci.* **2003**, 100, 9696.
- [104] S. Viel, F. Ziarelli, S. Caldarelli, G. Pages, *J. Magn. Reson.* **2008**, 190, 113.
- [105] A. Pampel, M. Fernandez, D. Freude, J. Kärger, *Chem. Phys. Lett.* **2005**, 407, 53.
- [106] E. E. Romanova, F. Grinberg, A. Pampel, J. Kärger, D. Freude, *J. Magn. Reson.* **2009**, 196, 110.
- [107] J. Tanner, *J. Chem. Phys.* **1970**, 52, 2523.
- [108] M. Tang, A. Redler, D. Topgaard, C. Schmidt, H.-S. Kitzerow, *Colloid Polym. Sci.* **2012**, 290, 751.
- [109] H. Pu, D. Yin, B. Gao, H. Gao, H. Dai, J. Liu, *J. Appl. Phys.* **2009**, 106, 083111.
- [110] M. Vilfan, G. Lahajnar, I. Zupancic, S. Zumer, R. Blinc, G. P. Crawford, J. W. Doane, *J. Chem. Phys.* **1995**, 103, 8726.
- [111] J. Zhang, R. P. MacGregor, B. J. Balcom, *Chem. Phys. Lett.* **2008**, 461, 106.
- [112] C. Chiccoli, P. Pasini, G. Skacej, C. Zannoni, S. Zumer, *Mol. Cryst. Liq. Cryst.* **2001**, 367, 2987.
- [113] G. P. Crawford, D. K. Yang, S. Zumer, D. Finotello, J. W. Doane, *Phys. Rev.*

- Lett.* **1991**, *66*, 723.
- [114] N. Bloembergen, E. M. Purcell, R. V. Pound, *Phys. Rev.* **1947**, *73*, 679.
- [115] M. Mehring, *Principles of High Resolution NMR in Solids*, Springer-Verlag, Berlin/Heidelberg/New York, **1983**.
- [116] D. C. Look, I. J. Lowe, *J. Chem. Phys.* **1966**, *44*, 2995.
- [117] S. W. Kelly, C. A. Sholl, *J. Phys.: Condens. Matter.* **1992**, *4*, 3317.
- [118] <http://chem.ch.huji.ac.il/nmr/techniques/other/t1t2/t1t2.html>, relaxation.
- [119] T. Blasco, J. Pérez-Pariente, W. Kolodziejski, *Solid State Nucl. Magn. Reson.* **1997**, *8*, 185.
- [120] T. H. Walter, G. L. Turner, E. Oldfield, *J. Magn. Reson.* **1988**, *76*, 106.
- [121] L. Muller, A. Kumar, T. Baumann, R. R. Ernst, *Phys. Rev. Lett.* **1974**, *32*, 1402.
- [122] R. K. Hester, J. L. Ackerman, V. R. Cross, J. S. Waugh, *Phys. Rev. Lett.* **1975**, *34*, 993.
- [123] D. Suter, R. R. Ernst, *Phys. Rev. B* **1985**, *32*, 5608.
- [124] A. Naito, C. A. McDowell, *J. Chem. Phys.* **1986**, *84*, 4181.
- [125] M. H. Levitt, D. Suter, R. R. Ernst, *J. Chem. Phys.* **1986**, *84*, 4243.
- [126] E. W. Hagaman, P. C. Ho, L. L. Brown, F. M. Schell, M. C. Woody, *J. Am. Chem. Soc.* **1990**, *112*, 7445.
- [127] A. M. Gil, E. Albertir, *Solid State Nucl. Magn. Reson.* **1998**, *11*, 203.
- [128] C. Schmidt, K. Kuhn, H. Spiess, *Prog. Colloid Polym. Sci.* **1985**, *71*, 71.
- [129] M. Vilfan, N. Vrbancic-Kopac, B. Zalar, S. Zumer, G. P. Crawford, *Phys. Rev. E* **1999**, *59*, 4754.
- [130] R. Pratima, K. V. Ramanathan, *J. Magn. Reson. A* **1996**, *118*, 7.
- [131] F. Tian, T. A. Cross, *J. Magn. Reson.* **1997**, *125*, 220.
- [132] A. K. Chattah, G. A. Alvarez, P. R. Levstein, F. M. Cucchiatti, H. M. Pastawski, J. Raya, J. Hirschinger, *J. Chem. Phys.* **2003**, *119*, 7943.
- [133] P. R. Levstein, A. K. Chattah, H. M. Pastawski, J. Raya, J. Hirschinger, *J. Chem. Phys.* **2004**, *121*, 7313.
- [134] H. Siebert, *Untersuchung des Fließverhaltens von flüssigkristallinen Polymeren unter Scherung mit <sup>2</sup>H-NMR-Spektroskopie, Röntgenbeugung, Neutronenstreuung und Polarisationsmikroskopie*, PhD thesis, University Freiburg, **1998**.
- [135] S.-T. Wu, *Appl. Opt.* **1987**, *26*, 3434.
- [136] J. W. Emsley, G. R. Luckhurst, C. P. Stockley, *Mol. Phys.* **1981**, *44*, 565.
- [137] J. Pelaez, M. Wilson, *Phys. Chem. Chem. Phys.* **2007**, *9*, 2968.

## Publications

1. **Tang, M. X.**; Redler, A.; Topgaard, D.; Schmidt, C. and Kitzerow, H.-S. “Kinetics of the grating formation in holographic polymer-dispersed liquid crystals: NMR measurement of diffusion coefficients.” *Colloid Polym. Sci.* **2012**, 290, 751–755.
2. Bayer, F. M.; **Tang, M. X.**; Michels, R.; Schmidt, C. and Huber, K. “Molecular Recognition with 2,4-Diaminotriazine-Functionalized Colloids.” *Langmuir* **2011**, 27, 12851-12858.

## Participation in conferences

1. **Tang, M. X.**; Redler, A.; Schmidt, C. and Kitzerow, H.-S. “Reaction-Diffusion Model for a Polymer-Dispersed Liquid Crystals Grating Involving Diffusion Measurement.” Poster, 24<sup>th</sup> International Liquid Crystal Conference, Mainz (Germany), 19–24.08.2012.
2. **Tang, M. X.**; Redler, A.; Topgaard, D.; Schmidt, C. and Kitzerow, H.-S. “Kinetics of the Grating Formation in Holographic Polymer-Dispersed Liquid Crystals: NMR Measurement of Diffusion Coefficients.” Poster, 1<sup>st</sup> Europhotonics Spring School, Barcelona (Spain), 25–31.03.2012.
3. Redler, A.; Hoischen, A.; **Tang, M. X.** and Schmidt, C. and Kitzerow, H.-S.: “Reaction-Diffusion Model for Holographic Polymer-Dispersed Liquid Crystals Utilizing NMR Data of the Diffusion Coefficients”, Poster, 2<sup>nd</sup> German Liquid Crystal Conference, Hamburg (Germany), 30. 03–01. 04. 2011.
4. **Tang, M. X.** and Schmidt, C.: “Investigation of the Dynamics of Liquid Crystals in a Complex System by NMR”, Oral presentation at “AK-Treffen 2011” Burg Breuberg (Germany), 25–28. 02. 2011.
5. **Tang, M. X.** and Schmidt, C.: “Solid State NMR of Polymer-Dispersed Liquid Crystals”, Oral presentation at the 10<sup>th</sup> Seminar on "Festkörper-NMR-Methoden und Anwendungen in der Materialforschung", Oberjoch (Germany), 18–22. 07. 2010.